# STRUCTURE AND DYNAMICS PROPERTIES INVOLVED WITH THE TRANSPORT OF IONS ACROSS LIPID MEMBRANE BY ION CHANNELS USING MOLECULAR DYNAMICS SIMULATIONS

Miss Sunan Kitjaruwankul



จุฬาลงกรณ์มหาวิทยาลัย
Chulalongkorn University
บทคัดย่อและแฟ้มข้อมูลฉบับเต็มของวิทยานิพนธ์ตั้งแต่ปีการศึกษา 2554 ที่ให้บริการในคลังปัญญาจุฬาฯ (CUIR)
เป็นแฟ้มข้อมูลของนิสิตเจ้าของวิทยานิพนธ์ที่ส่งผ่านทางบัณฑิตวิทยาลัย
The abstract and full text of theses from the academic year 2011 in Chulalongkorn University Intellectual Repository (CUIR)
are the thesis authors' files submitted through the University Graduate School.

A Dissertation Submitted in Partial Fulfillment of the Requirements
for the Degree of Doctor of Philosophy Program in Nanoscience and Technology
(Interdisciplinary Program)
Graduate School
Chulalongkorn University
Academic Year 2015

Copyright of Chulalongkorn University

# โครงสร้างและสมบัติเชิงพลวัติที่เกี่ยวข้องกับการขนส่งไอออนผ่านลิพิดเมมเบรน โดยไอออนแชนนัลด้วยการจำลองพลวัติเชิงโมเลกุล

นางสาวสุนันท์ กิจจารุวรรณกุล

จุฬาลงกรณ์มหาวิทยาลัย
Chulalongkorn University

วิทยานิพนธ์นี้เป็นส่วนหนึ่งของการศึกษาตามหลักสูตรปริญญาวิทยาศาสตรดุษฎีบัณฑิต
สาขาวิชาวิทยาศาสตร์นาโนและเทคโนโลยี (สหสาขาวิชา)
บัณฑิตวิทยาลัย จุฬาลงกรณ์มหาวิทยาลัย
ปีการศึกษา 2558
ลิขสิทธิ์ของจุฬาลงกรณ์มหาวิทยาลัย

| | |
|---|---|
| Thesis Title | STRUCTURE AND DYNAMICS PROPERTIES INVOLVED WITH THE TRANSPORT OF IONS ACROSS LIPID MEMBRANE BY ION CHANNELS USING MOLECULAR DYNAMICS SIMULATIONS |
| By | Miss Sunan Kitjaruwankul |
| Field of Study | Nanoscience and Technology |
| Thesis Advisor | Associate Professor Pornthep Sompornpisut, Ph.D. |

Accepted by the Graduate School, Chulalongkorn University in Partial Fulfillment of the Requirements for the Doctoral Degree

.....Dean of the Graduate School
(Associate Professor Sunait Chutintaranond, Ph.D.)

THESIS COMMITTEE

.....Chairman
(Associate Professor Vudhichai Parasuk, Ph.D.)
.....Thesis Advisor
(Associate Professor Pornthep Sompornpisut, Ph.D.)
.....Examiner
(Professor Vithaya Ruangpornvisuti, Dr.rer.nat.)
.....Examiner
(Ratthapol Rangkupan, Ph.D.)
.....External Examiner
(Saree Phongphanphanee, Ph.D.)

สุนันท์ กิจจารุวรรณกุล : โครงสร้างและสมบัติเชิงพลวัติที่เกี่ยวข้องกับการขนส่งไอออนผ่านลิพิดเมมเบรนโดยไอออนแชนนัลด้วยการจำลองพลวัติเชิงโมเลกุล (STRUCTURE AND DYNAMICS PROPERTIES INVOLVED WITH THE TRANSPORT OF IONS ACROSS LIPID MEMBRANE BY ION CHANNELS USING MOLECULAR DYNAMICS SIMULATIONS) อ.ที่ปรึกษาวิทยานิพนธ์หลัก: รศ. ดร.พรเทพ สมพรพิสุทธิ์, 87 หน้า.

ไอออนแชนนัลเป็นโปรตีนฝังในเมมเบรนทำหน้าที่คัดเลือกและส่งไอออนข้ามผ่านเมมเบรนของเซลล์ การทำงานของไอออนแชนนัลถูกกระตุ้นได้ด้วยสิ่งเร้าที่แตกต่างกัน ทั้งนี้กลไกการทำงานในระดับโมเลกุลที่เกี่ยวข้องกับการคัดเลือกไอออนจำเพาะ (ion selectivity) และกลไกการเปิด-ปิดช่องทางผ่านของไอออน (gating) ได้มีการศึกษาเชิงลึกมาอย่างต่อเนื่องตั้งแต่โครงสร้างผลึกแรกของโพแทสเซียมไอออนแชนนัลได้รับการตีพิมพ์ในปี 1998 ในงานวิจัยนี้มีจุดประสงค์เพื่อศึกษาความสัมพันธ์ทางโครงสร้างและหน้าที่ของไอออนแชนนัลสองชนิดคือโพแทสเซียมแชนนัล (KvAP) และแมกนีเซียมแชนนัล (TmCorA) ด้วยวิธีการสร้างแบบจำลองและการจำลองพลวัติเชิงโมเลกุล ส่วนแรกของงานวิจัยนี้เป็นผลการศึกษาพลวัติเชิงโมเลกุลของโดเมนรับรู้ศักย์ไฟฟ้า (VSD) ของ KvAP แชนนัลในทั้งสองสภาวะการทำงาน ได้แก่ Up และ Down ผลการจำลองพลวัติในสภาวะ Down ที่ใช้ลิพิด 2 ชนิดคือฟอสโฟลิพิดและนอน-ฟอสโฟลิพิดไบเลย์ แสดงให้เห็นถึงโมเลกุลของน้ำที่เข้าถึงมากขึ้นในส่วนแกนกลางของ VSD ในฝั่งด้านในเซลล์ เมื่อเปรียบเทียบกับผลการจำลองพลวัติในสภาวะ Up การเปลี่ยนแปลงรูปทรงของรอยแยกของน้ำที่เกิดขึ้นในสภาวะ Down เมื่อเปรียบเทียบกับในสภาวะ Up นี้ เป็นไปเพื่อรองรับการเคลื่อนที่ของกรดอะมิโนอาร์จินีนที่เคลื่อนที่เข้าไปในฝั่งด้านในเซลล์ลิพิดไบเลย์ ส่วนที่สองของวิทยานิพนธ์นี้เป็นผลการศึกษาสมบัติการคัดเลือกไอออนจำเพาะของ TmCorA แชนนัล ผลการจำลองพลวัติและการคำนวณในระดับเคมีควอนตัมได้ดำเนินการเพื่อตรวจสอบเคมีโคออร์ดิเนชันและโครงสร้างของแมกนีเซียมไอออน ($Mg^{2+}$) และไอออนอื่นๆ ในส่วนคัดกรองเลือกจำเพาะ (selectivity filter) ที่ประกอบด้วยกรดอะมิโนอนุรักษ์ ไกลซีน-เมทไทโอนีน-แอสพาราจีน (GMN) ของ TmCorA แชนนัล ผลการจำลองพลวัติแสดงให้เห็นว่าลำดับกรดอะมิโน GMN ทำหน้าที่เป็นลิแกนด์ในชั้นที่สองของ $Mg^{2+}$ โดยในชั้นที่หนึ่งของ $Mg^{2+}$ มีน้ำ 6 โมเลกุลที่จัดเรียงเป็นออกตะฮีดรัล ส่วนการนำเอา $Mg^{2+}$ ออกจากบริเวณรับรู้ไดเวเลนท์แคทไอออน (DCS) เป็นผลให้เกิดการสร้างพันธะที่อ่อนลงระหว่าง $Mg^{2+}$ กับบริเวณคัดกรอง นอกจากนี้ผลการคำนวณด้วยวิธี QM/MM แสดงค่าพลังงานส่วนร่วมจากบริเวณ GMN เพื่อให้ไฮเดรตไอออนที่ถูกเลือกจับมีความเสถียรในการอยู่ที่บริเวณนี้เรียงลำดับเป็น $Co^{3+}$-hex > $Al^{3+}$ > $Ni^{2+}$-hex, $Co^{2+}$, $Ni^{2+}$, $Mg^{2+}$, $Ca^{2+}$ > $K^{+}$ > $Li^{+}$ > $Na^{+}$ ซึ่งสอดคล้องกับลำดับการเลือกจับไอออนของโปรตีน CorA ที่อ้างอิงจากผลการผลทดลองและสนับสนุนสมบัติการเลือกจับไอออนที่มีโครงสร้างเป็นออกตะฮีดรัล

สาขาวิชา วิทยาศาสตร์นาโนและเทคโนโลยี ลายมือชื่อนิสิต .....

ปีการศึกษา 2558 ลายมือชื่อ อ.ที่ปรึกษาหลัก .....

# # 5587852620 : MAJOR NANOSCIENCE AND TECHNOLOGY
KEYWORDS: POTASSIUM CHANNEL, MAGNESIUM CHANNEL, VOLTAGE-SENSOR DOMAIN, MD SIMULATIONS, QM/MM

SUNAN KITJARUWANKUL: STRUCTURE AND DYNAMICS PROPERTIES INVOLVED WITH THE TRANSPORT OF IONS ACROSS LIPID MEMBRANE BY ION CHANNELS USING MOLECULAR DYNAMICS SIMULATIONS. ADVISOR: ASSOC. PROF. PORNTHEP SOMPORNPISUT, Ph.D., 87 pp.

Ion channels are integral membrane proteins that select and transport ions across biological membranes. They are activated by a variety of stimuli. The molecular mechanism underlying ion selectivity and gating of ion channels has been a subject of intense research since the first crystal structure of potassium channel had been published in 1998. The aim of this thesis is to investigate the structure-function relationship of two ion channels, potassium (KvAP) channel and magnesium (TmCorA) channel, using molecular modeling and molecular dynamics simulations. The first part of the thesis is a molecular dynamics (MD) study of voltage sensor domain (VSD) of KvAP channel in two functional states, Up and Down. The MD simulations of Down-conformation conducted in two different lipid types, phospholipid and non-phospholipid bilayer, revealed higher accessible water molecules at the intracellular side of the VSD core than that of the Up-conformation. The results showed a change in the shape of water-crevice of the Down conformation with respect to that of the Up structure to accommodate the charged arginines moving towards the intracellular side of the bilayer. The second part of this thesis is the investigation of the ion selectivity of TmCorA channel. MD simulations and quantum chemical calculations were carried out to explore coordination chemistry and solvation structure of $Mg^{2+}$ and other cations in the selectivity filter containing the conserved Gly-Met-Asn (GMN) sequence of TmCorA. The results showed that the GMN residues act as the second shell ligands for $Mg^{2+}$. The first-shell structure of $Mg^{2+}$ has six water molecules in an octahedral arrangement. The removal of $Mg^{2+}$ at the Divalent Cation Sensor (DCS) site caused a weaker binding of $Mg^{2+}$ to the filter. Moreover, the QM/MM results revealed the stabilization energy ordered from $Co^{3+}$-hex > $Al^{3+}$ > $Ni^{2+}$-hex, $Co^{2+}$, $Ni^{2+}$, $Mg^{2+}$, $Ca^{2+}$ > $K^{+}$ > $Li^{+}$ > $Na^{+}$ which is consistent with the experimental selective trend of metal ions in CorA proteins supporting the selectivity property of binding with the octahedral metal complex.

Field of Study: Nanoscience and Technology Student's Signature .....

Academic Year: 2015 Advisor's Signature .....

# ACKNOWLEDGEMENTS

This thesis would not be complete if there is no helps from all of the following persons.

Firstly, I deeply appreciate my advisor, Assoc. Prof. Dr. Pornthep Sompornpisut, for his kindness, motivation, patience, and thoughtfulness. His guidance is very meaningful not only for doing research but also for being optimistic. Besides him, I am sincerely grateful to the rest of my thesis committee: Assoc. Prof. Dr. Vudhichai parasuk, Prof. Dr. Vithaya Ruangpornvisuti, Dr. Ratthapol Rangkupan, and Dr. Saree Phongphanphanee for their insightful comments and suggestions. In addition, my faithful thanks also go to all of my teachers who have educated me since I was young.

As being a friendship, I would like to thank my coworkers: Miss Sunit Fuklang , Miss Pattama Wapeesittipan, Mr. Kanon Sujaree, Mr. Panisak Boonamnaj, Mr. Chirayut Supunyabut, and Mr. Suppasith Assawa as well as other members in the computational chemistry unit cell (CCUC) at Department of Chemistry, Faculty of Science, Chulalongkorn University for their discussion, encouragement and cheerfulness. Moreover, I also would like to express my gratitude to the Nanoscience and Technology Program Graduate School, Chulalongkorn University for providing all facilities throughout the course.

Importantly, I would like to acknowledge all my financial supports including Faculty of Science at Sriracha, Kasetsart University Sriracha Campus, the DPST scholarship from the Institute for the Promotion of Teaching Science and Technology, Bangkok, Thailand, the Ratchadaphiseksomphot Endowment Fund, Chulalongkorn University and the 90th Anniversary of Chulalongkorn University.

Last but not least, I would like to thank my beloved family for being beside and supporting me all the time.

จุฬาลงกรณ์มหาวิทยาลัย
Chulalongkorn University

**CONTENTS**

Page



จุฬาลงกรณ์มหาวิทยาลัย
CHULALONGKORN UNIVERSITY

Page



จุฬาลงกรณ์มหาวิทยาลัย
Chulalongkorn University

Page

# LIST OF FIGURES

**Page**

**Page**



จุฬาลงกรณ์มหาวิทยาลัย
Chulalongkorn University

**Page**

**Page**

**Page**



จุฬาลงกรณ์มหาวิทยาลัย
Chulalongkorn University

# LIST OF TABLES

**Page**

## LIST OF ABBREVIATIONS

| | |
|---|---|
| $K_v$ | voltage-gated potassium channel |
| $K_{ir}$ | inwardly rectifying potassium channel |
| $Na_v$ | voltage-gated sodium channel |
| $Ca_v$ | voltage-gated calcium channel |
| $H_v$ | voltage-gated proton channel |
| KvAP | voltage-dependent potassium channel from *Aeropyrum pernix* |
| Ci–VSP | *Ciona intestinalis* voltage-sensitive phosphatase |
| VSD | voltage sensor domain |
| TmCorA | cobalt resistance protein from *Thermotoga maritima* |
| Mrs2 | mitochondrial magnesium channel |
| Alr1 | aluminium resistance protein |
| MjCorA | CorA protein from *Methanocaldococcus jannaschii* |
| DCS | divalent cation sensor |
| MD | molecular dynamics |
| SF | selectivity filter |
| GMN | glycine-methionine-asparagine |
| QM/MM | quantum mechanics/molecular mechanics |
| P-loop | pore domain loop |
| TM | transmembrane |
| S1-S6 | transmembrane helices 1 to 6 of VSD |
| 3D | three dimensional |
| R | arginine |
| D | aspartic acid |
| E | glutamic acid |
| POPC | 1-palmitoyl2-oleoyl-sn-glycero-3-phophochloline |
| DOTAP | 1,2-dioleoyl-3-trimethylammonium-propane |
| PCPG | phosphatidylcholine/phosphatidylglycerol |
| SDSL/EPR | site-directed spin labeling/electron paramagnetic resonance |
| PaDSAR | pseudoatom-driven solvent accessibility refinement |
| MTSSL | methanethiosulfonate spin label |

จุฬาลงกรณ์มหาวิทยาลัย
Chulalongkorn University

| | |
|---|---|
| $\Pi H_o^{-1}$ | probe mobility data |
| $\Pi O_2$ | oxygen accessibility data |
| ΠNiEDDA | nickel-ethylenediamine diacetate accessibility data |
| PBE | Poisson-Boltzmann equation |
| RMSD | root-mean-square-deviation |
| RMSF | root-mean-square-fluctuation |
| ATP | adenosine triphosphate |
| DNA | deoxyribonucleic acid |
| RNA | ribonucleic acid |
| TIP3P | transferable intermolecular potential three-position |
| RDF or g(r) | radial distribution function or pair correlation function |
| PCA | principle component analysis |
| MRT | mean residence time |
| ONIOM | Our own N-layered Integrated molecular Orbital and molecular Mechanics |
| B3LYP | Becke, 3-parameter, Lee-Yang-Parr |
| PM6 | Parameterized Model number 6 |
| UFF | Universal Force Field |
| $Co^{3+}$-hex or Cohex | cobalt hexaammine |
| $Ni^{2+}$-hex or Nihex | nikel hexaammine |
| $E_z$ | external electric field |
| $L_z$ | length of the membrane along the z-axis |
| C(t) | time correlation function |
| T(0) | binary function at time 0 |
| T(t) | binary function at time t |
| T | period of determining time |
| $\Delta E([ML_x]^{n+})$ | complexation energy |
| $\Delta E([ML_xW_y]^{n+})$ | total complexation energy |
| $\Delta E_{sSF}$ | stabilization energy from the selectivity filter |

จุฬาลงกรณ์มหาวิทยาลัย
Chulalongkorn University

# CHAPTER I: INTRODUCTION

In cells, there are common biological cations including $Na^+$, $K^+$, $Mg^{2+}$ and $Ca^{2+}$ that involve in many important metabolisms. They are essential signal transduction ions in neuron system; moreover, they are cofactors in many catalytic enzymes. Therefore, the ion homeostasis has to be regulated to maintain the normal condition of the living cells.

In aqueous solution or in cytoplasm, ions prefer to be polarized with water molecules forming the hydrated ions where oxygen atoms of water molecules face toward cation with different configurations, for instance, octahedron for $Na^+$, $Mg^{2+}$ and square antiprism for $K^+$ as shown in Figure 1.1 and the configurations of these 4 cations are shown in Table 1.1.

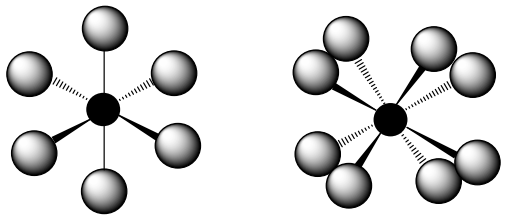

**Figure 1.1** The octahedron and Square antiprism models of hydrated ions.

**Table 1.1** Calculated ionic radius, M–O distance, configuration of hydrated cation in aqueous [1].

| aqua complex | $M^{n+}$'s ion radius (Å) | M–O distance | configuration |
|---|---|---|---|
| $Na(H_2O)_6^+$ | 1.09 | 2.43 | Octahedron |
| $K(H_2O)_8^+$ | 1.50 | 2.84 | Square antiprism |
| $Mg(H_2O)_6^{2+}$ | 0.76 | 2.10 | Octahedron |
| $Ca(H_2O)_8^{2+}$ | 1.12 | 2.46 | Square antiprism |

Unlike small uncharged molecules that can freely pass across the phospholipid membrane, these polar hydrated ions are impermeable through the membrane according to the incompatibility of polarization as demonstrated in Figure 1.2.

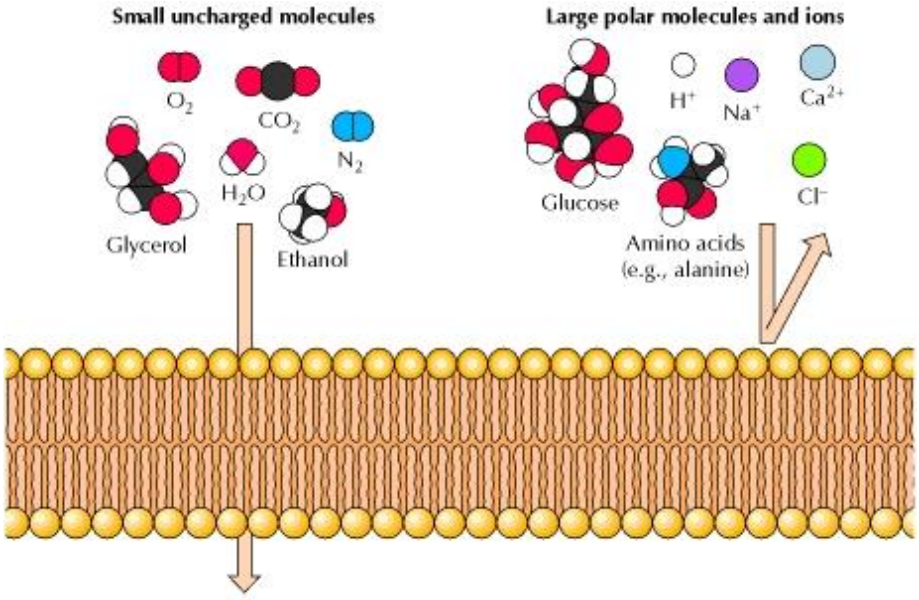


**Figure 1.2** The permeability of lipid bilayers [2].

However, every cell membrane does not contain only lipid compartments but also contains the embedded proteins, the integral membrane proteins, functioning as the nanoscale-transmembrane pores to allow the specific ions across the cell membrane. In addition, membrane proteins can be classified into 3 types including ion channels, carriers and pumps. The transport mechanisms of ion channels and carriers are passive diffusions depending on the electrochemical gradient but the transportation of pumps is active transport against a chemical gradient with utilizing the energy from ATP hydrolysis. Ion channels and carriers can be discriminated by the transportation rate with a very high rate of up to $10^8$ mol/s for ion channels while 10-$10^4$ mol/s for carriers and the conformational change occurring in carriers when binding with substrate ions [3]. Ion channels can open the gate to let selectively ions passing when they are activated and close the gate when they are inactivated depending on the driving force including membrane's potential (voltage-gated ion channels), ligand binding (ligand-gated ion channels) and mechanical stimuli (mechanosensitive ion channels) [4]. In addition, we can classify a type of ion channels regarding to the substrate ions as sodium channel, potassium channel, magnesium channel and calcium channel (Figure 1.3).

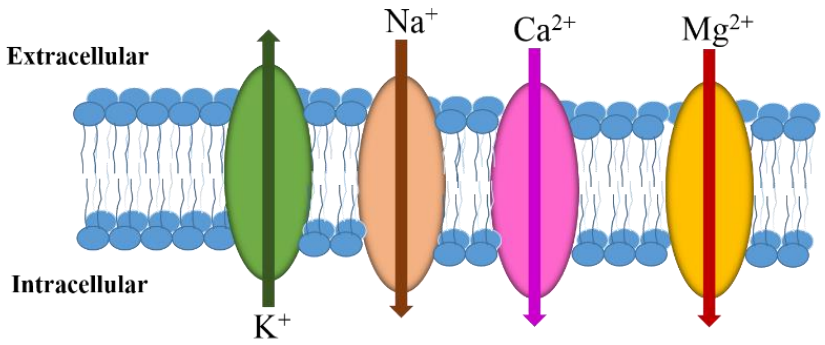


**Figure 1.3** Ion channel specified by individual ions.

Due to the function of ion channel mainly on the neuron transduction, the ion channel dysfunction can cause many channelopathies, for instance, hypertension, arrhythmia, anesthesia, epilepsy, seizure, cardiac arrhythmias [5]. Therefore the understanding of ion channel mechanisms is compulsory because they are the important drug targets that have been continuously developed and examined. The examples of some channelopathies involved in the ion channel disorders are shown in Table 1.2.

Nowadays, ion channels are not only the drug targets of human deceases but also the targets of insecticides that focus on the $Na_v$ channel [6]. Moreover, another ion channel like Mg channel that functions to regulate the $Mg^{2+}$ in cells is also the interesting membrane protein for studying in the molecular dynamics level to understand its mechanism too because the deficiency of $Mg^{2+}$can cause many diseases including diabetes, hypertension, coronary heart disease, and osteoporosis.[7] Here, the structural properties of voltage-gated potassium ion channel and magnesium ion channel are investigated by mean of molecular dynamic (MD) simulations. Therefore, this thesis contains 2 main topics as reported in the studied details of each ion channel in chapter II and chapter III, respectively. The interesting investigation points about KvAP and TmCorA channels are summarized in Table 1.3.

**Table 1.2** Selected channelopathies regarding to channel dysfunction.[8]

| ion channel family | channel | disease |
|---|---|---|
| $K_{ir}$ | $K_{ir}1.1$ | Bartter's syndrome |
| | $K_{ir}2.1$ | Andersen's Syndrome |
| $K_v$ | $K_v1.1$ | Episodic ataxia type 1 |
| $Na_v$ | $Na_v1.1$ | Epilepsy |
| | $Na_v1.5$ | Long QT syndrome |
| | $Na_v1.6$ | Cerebellar ataxia |
| | $Na_v2.1$ | Benign familial neonatal seizures |
| $Ca_v$ | $Ca_v1.2$ | Timothy syndrome |

**Table 1.3** The summarized details and the awaiting issue for investigation in this research.

| protein | available data | investigation point |
|---|---|---|
| KvAP-VSD | x-ray / activated (Up) state | The conformational change |
| TmCorA | x-ray/ closed state | Ion selectivity property |

จุฬาลงกรณ์มหาวิทยาลัย
Chulalongkorn University

# CHAPTER II: STRUCTURAL DYNAMICS OF VOLTAGE-SENSOR DOMAIN OF VOLTAGE-GATED POTASSIUM ION CHANNEL BY A COMPUTATIONAL STUDY

Voltage-gated sodium, potassium and calcium ($Na_v$, $K_v$ and $Ca_v$) channels are voltage-gated ion channels that can open or close the gate depending on the electrical potential of cell membranes [9]. The channels are composed of four subunits, each of which consists of six transmembrane segments. The voltage-dependent ion channels share a basic molecular architecture in which they contain two functional independence domains, i.e. voltage sensor domain (VSD) and the central pore domain (PD) [10, 11]. The VSD is the voltage detection unit regarding changes in the membrane potential, and subsequently induces the PD to transition from the closed or resting state to the open or activated state of the channel [12, 13].

Generally, different types and ion concentrations between the inner and outer cell result in a voltage different at the membrane of the cells. For instance, in a resting state of nerve cells, $Na^+$ concentration of extracellular side is higher than that of intracellular side whereas $K^+$ concentration of the outer cell is lower than that of the inner cell [14] as a result of having the membrane potential of about -70 mV. When cell is stimulated both $Na_v$ and $K_v$ channels will open causing membrane depolarization to reach the action potential of about 30 mV then $Na_v$ channel will be closed while allowing $K_v$ channel still open to repolarize the membrane potential. Typically, the repolarized potential overshoots the resting potential to about -90 mV as called the hyperpolarization step to prevent the receiving of another stimulus during this time. After that, the Na-K pump is active to restore the normal resting potential [15]. The action potential process is shown in Figure 2.1.

จุฬาลงกรณ์มหาวิทยาลัย
Chulalongkorn University

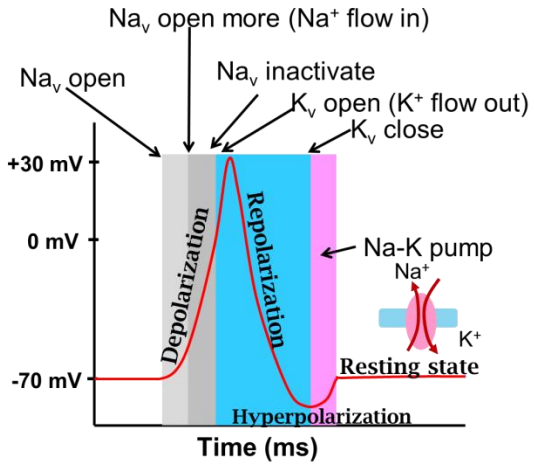


**Figure 2.1** The action potential graph of the nerve cells.

## 2.1 Literature review

In 2003, the 3D-crystal structures of the full-length and isolated-VSD of the $K_v$ from *Aecheabacteria aeropyrumpernix* (KvAP) were reported by Jiang and colleagues [16]. The full-length structure demonstrates a symmetric homotetramer consisting of six transmembrane helices (S1-S6) where the S1-S4 helices form the voltage sensor domain (VSD) part and the S5-S6 helices form the pore domain part (Figure 2.2). The KvAP-VSD exhibits an independent function as reported from Jiang *et al.* that a monomer of KvAP-VSD still responses to bind with protein toxins, voltage-sensing inhibitors [16]. Moreover, the independent function of the VSD in ion channels is supported by the other VSD-containing proteins like *Ciona intestinalis* voltage-sensitive phosphatase (Ci-VSP) and voltage-gated proton ($H_v$) channel that have no ion-conducting pores but can sense the voltage changes of membrane potential (Figure 2.3) [17-20]. However, the available crystal structures of the $K_v$ channels and $Na_v$ channel are all in the activated-state conformations because it is impossible to crystalize them in the presence of a negative potential. Therefore the resting-state conformation is necessary to study deep insight into the molecular mechanism of the channel function.

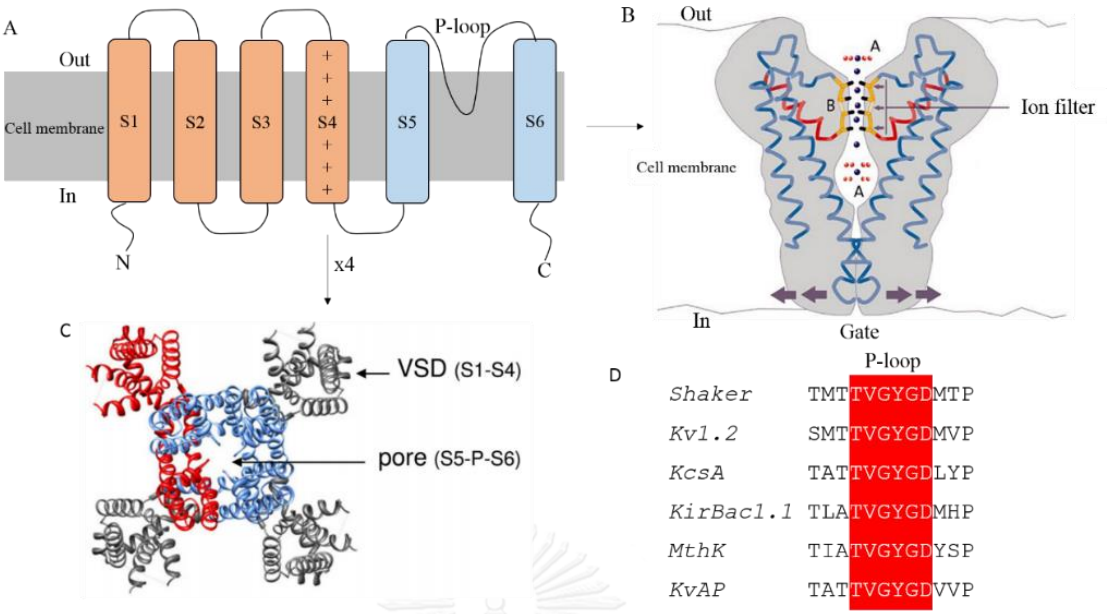


**Figure 2.2** (A) Cartoon of the 6-TM in one subunit of $K_v$ channel (B) Side view of the pore domain (C) Top view (extracellular side) of $K_v$ channel (D) Sequence alignment of the P-loop in the potassium channel family [16].

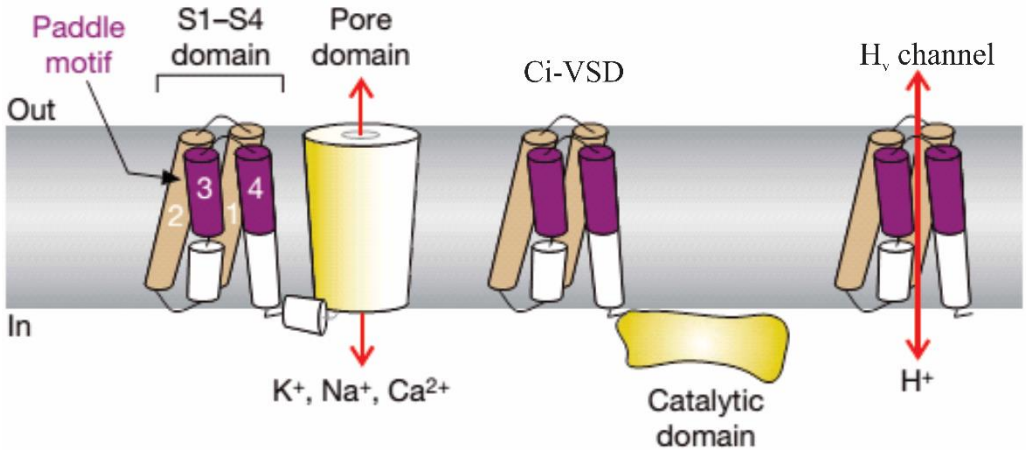


**Figure 2.3** Cartoon representation of voltage-gated ion channels, Ci-VSP and $H_v$ channel [13].

## 2.2 Gating charges

Since 1952, Hodskin and Huxley [21] proposed the remarkable discovery that the ion conduction of excited cells resulted from the movement of some charged components in membrane which is called the gating charge. Afterwards, the

experimental and theoretical studies have been interested in determining the total gating charge from the gating current. It has been reported that a total gating charge is about 13 e (~ 3 e/ VSD-unit) [22-26]. A dominant part of the gating charge movement is on the S4 helix which contains 5 highly conserved arginine residues at every third position including R117(R1), R120(R2), R123(R3), R126(R4) and R133(R5) as illustrated in Figure 2.4(A). The x-ray structure of Up-state conformation reveals the first 4 residues locating near the lipid-solvent interface while the R5 is formed salt-bridge interaction with aspartate 62 (D62) that located on the S2 helix as illustrated in Figure 2.4(B).

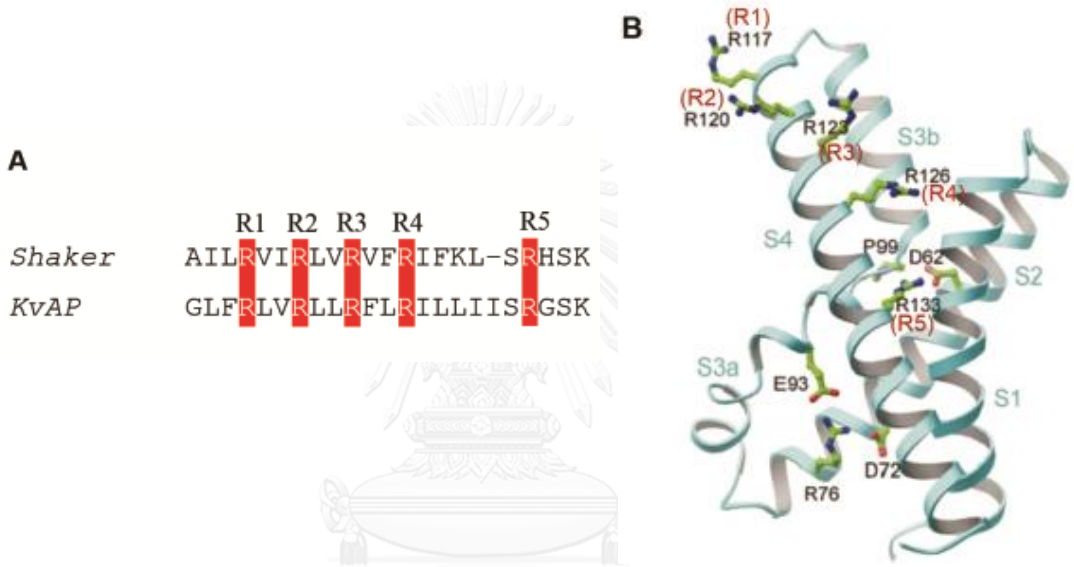


**Figure 2.4** (A) sequence alignment of S4 segment in Shaker and KvAP (B) X-ray structure of KvAP-VSD showing the selected residues on the S4 helix.

## 2.3 Voltage-sensing Models

It has been proposed that the gating charge occurring in the S4 segment of VSD can drive the pore domain opening. However, the mechanism of this movement remains unclear. There are three proposed models based on the experimental results including the helical screw model, the paddle model and the transporter model.

For the helical screw model the S4 helix rotates and translates at the same time along its own helical axis [27, 28]. The paddle model [16, 29] is related to the motion of the paddle part (S3b-S4) which forms the helix-turn-helix structure. This motion is

like paddling a boat. Whereas the transporter model [30, 31] the S4 helix tilts and rotates a little (~2-3 Å) as demonstrated in Figure 2.5.

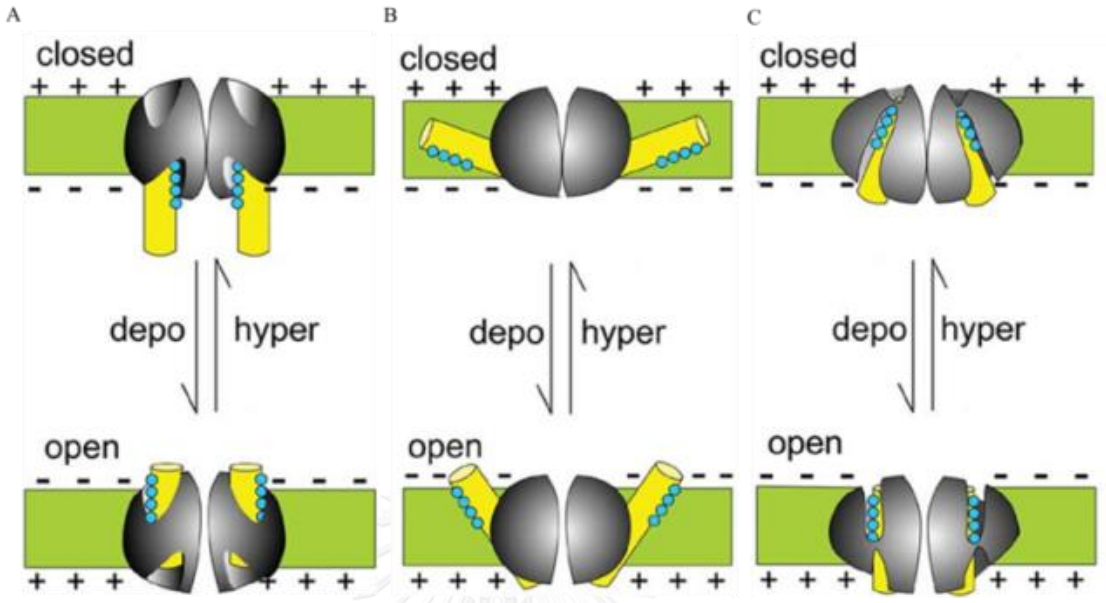


**Figure 2.5** Three models of the movement of the S4 helix in the VSD (A) Helical screw model (B) Paddle model (C) Transporter model [32].

## 2.4 Down-state conformation and VSD coupling pore domain mechanism

A lack of the Down-state crystal structure of KvAP channel results in the ambiguous explanation of molecular detail about the conformation change upon membrane depolarization. To understand at the molecular detail, the Down-state conformation of KvAP and the dynamics property along the 2 states are required by means of the accessibility data from the experiments incorporated with the molecular dynamics simulations.

Based on the crystal structure of KvAP [16], it is hypothesized that the S4 sensor is stabilized in the Up-state conformation. This idea has been supported by the electron microscopic analysis [33, 34] that the gating charge residues move at the protein-lipid interface. From electrophysiological studies, they suggest that KvAP exhibits the non-conductive state when it is in the non-phospholipid bilayer (1,2-dioleoyl-3-trimethylammonium-propane or DOTAP) and it can transform to the active-state when reconstituted into the phospholipid bilayer [35, 36].

In 2010, Zheng *et al*. [37] investigated the conformation change of the KvAP in DOTAP comparing with in a phospholipid bilayer (1-palmitoyl-2-oleoyl-sn-glycero-3-phophochloline or POPC) by using electrophysiological and mutagenesis experiments. They found that KvAP can change the conformation from Up-state in POPC to Down-state in DOTAP at 0 mV comparable to voltage changing from -80 mV (Up-state) to 0 mV (Down-state) in POPC (Figure 2.6).

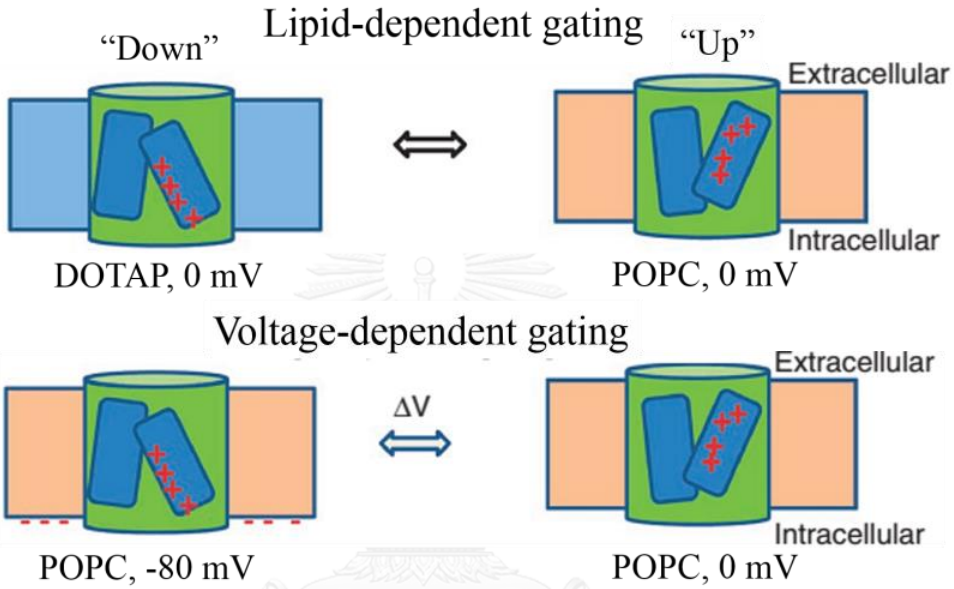


**Figure 2.6** Cartoon caomparison between lipid-dependent gating and voltage-dependent gating of KvAP-VSD [37].

In addition, Krepkiy *et al.* [38] employed NMR, fluorescence and circular dichroism to explore the structural interaction between lipids, water and the VSD. They concluded that the arginine residues in the S4 of KvAP-VSD interact with both hydrophobic acyl chains and phosphodiesters in POPC while, in DOTAP, the interactions between the VSD and acyl chains are detected without disrupting the overall secondary structure of VSD. Moreover, the VSD in both lipids is well hydrated indicating an existence of the water crevices in the Up and Down-state conformations. The presence of the water crevices in the VSD is thought to increase dielectric environment in the membrane. The POPC and DOTAP structure are shown in Figure 2.7.

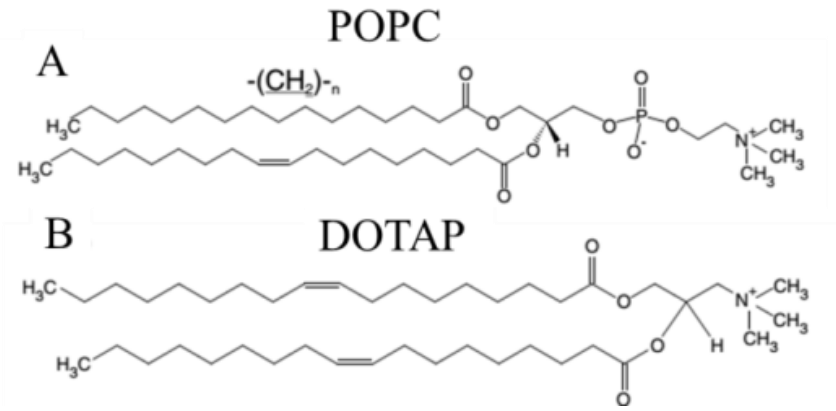


**Figure 2.7** The chemical strucutres of POPC and DOTAP.

## 2.5 The water-filled crevice in the VSD

Based on the results from cysteine accessibility and voltage-patch clamp techniques of the Shaker $K^+$ channel [39-41], it has been found that the movement of S4 segment in response to the membrane potential showed the accessibility to methanethiosulfonate suggesting the presence of aqueous crevices in both intracellular and extracellular sides. Additionally, the results from MD simulations on the KvAP-VSD in POPC [42, 43] revealed that the Up-state conformation of the KvAP-VSD is stabilized in the hydrated lipid bilayer by hydrogen bond interactions of Arg residues located on the S4 helix with water molecules.

In 2011, Andersson *et al*. [44] performed MD simulations of the S4 helix of KvAP in POPC and in DOTAP. The MD results of the S4 helix in POPC showed a hydrophobic gap at the center of the lipid. In DOTAP, they, however, observed the water wires penetrating the hydrophobic gap structure of the S4 helix. The water wires occurred in the DOTAP system and the comparing water density profile between the POPC and DOTAP system are shown in Figure 2.8.

In 2012, Sunit [45] performed MD simulations of Up-state in POPC at 0 mv and Down-state in POPC at -70 mV of KvAP-VSD for 50 ns. The results showed that there were water distributions in the VSD structure revealing the hourglass-like shape in the VSD as shown in Figure 2.9.

In 2014, Li *et al*. [31] investigated structure and dynamics of KvAP-VSD in Down-state by using Site Directed Spin Labeling – Electron Paramagnetic Resonance

(SDSL/EPR) data. The protein was reconstituted in a mixed lipid bilayer of phosphatidylcholine/phosphatidylglycerol (POPC/POPG or PCPG) and in DOTAP. They employed a computational approach "PseudoAtom-Driven Solvent Accessibility Refinement (PaDSAR) method [46] to construct the Up- and Down-conformations of KvAP-VSD. Their result illustrated the distinct difference between both conformations in which the Down-state structure represented a larger intracellular water crevice than the extracellular side while there was a little water accessibility in the Up-state. They proposed the tilt-shift model as displayed in Figure 2.10.

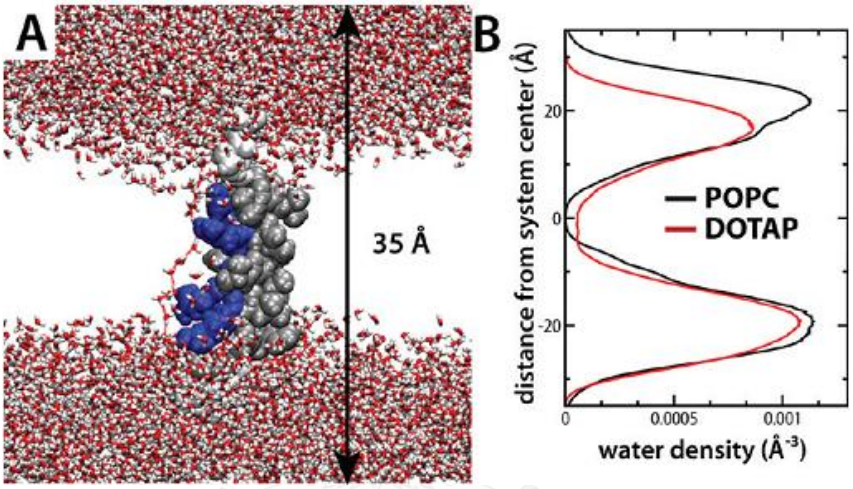


**Figure 2.8** (A) A snapshot from the DOTAP simulation. (B) The number densities of water in the first and second solvation shells around the Arg residues in POPC (black line) and DOTAP (red line) [44].

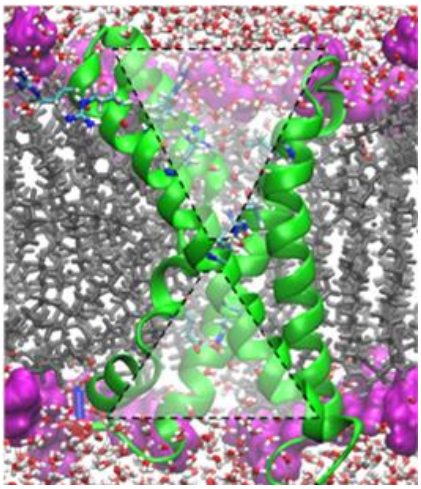

**Figure 2.9** The hourglass-like shape of water crevices in the VSD [45].

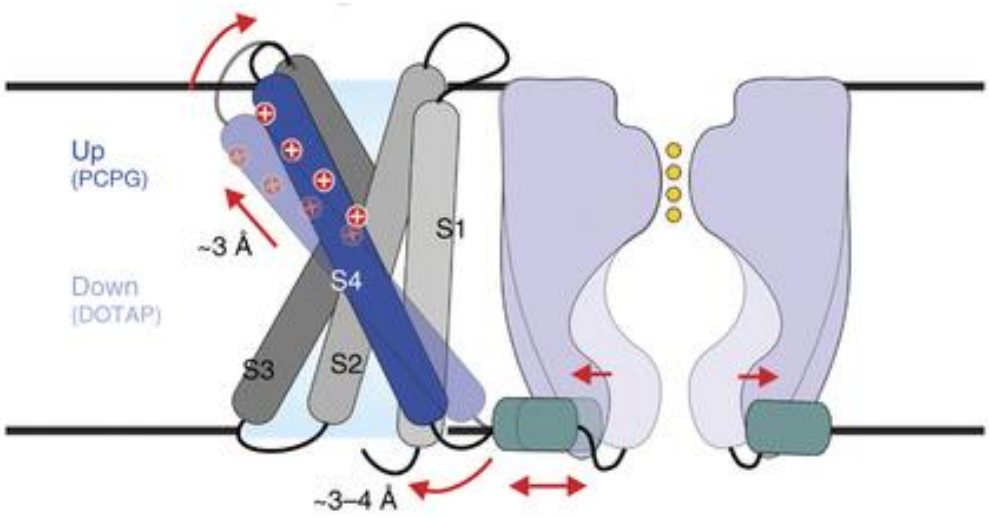


**Figure 2.10** The tilt-shift model on KvAP-VSD [31].

## 2.6 SDSL/EPR technique and PaDSAR method

Basically, the site-directed spin labeling (SDSL) method is a biophysical and biochemical technique. The nitroxide free radical (spin) compound is tagged to a desired site of the protein based on the basis of a specific chemical reaction between spin labels and cysteine residues. The spin label reagent is the sulfhydryl-specific nitroxide and the most commonly used one is methanethiosulfonate spin label (MTSSL or spin label I) [47] (Figure 2.11).

The SDSL/EPR technique provides three types of structural parameters. 1) the motional dynamics or called the mobility value as calculated from the inverse linewidth of the central resonance ($\Delta H_o^{-1}$) of the spectral line. 2) side-chain accessibility between spin labels and paramagnetic relaxation reagents including oxygen accessibility ($\Pi O_2$) and NiEDDA accessibility ($\Pi$NiEDDA). The $\Pi O_2$ is used for determining the lipid-exposed residues because $O_2$ gas is hydrophobic and can permeate into the membrane while the $\Pi$NiEDDA is used for determining the aqueous-exposed residue because NiEDDA is water-soluble and cannot permeate into the membrane. 3) spin-spin coupling distance including intra-spin and interspin-distances which are used for determining the global structure of protein and the conformational change [48].

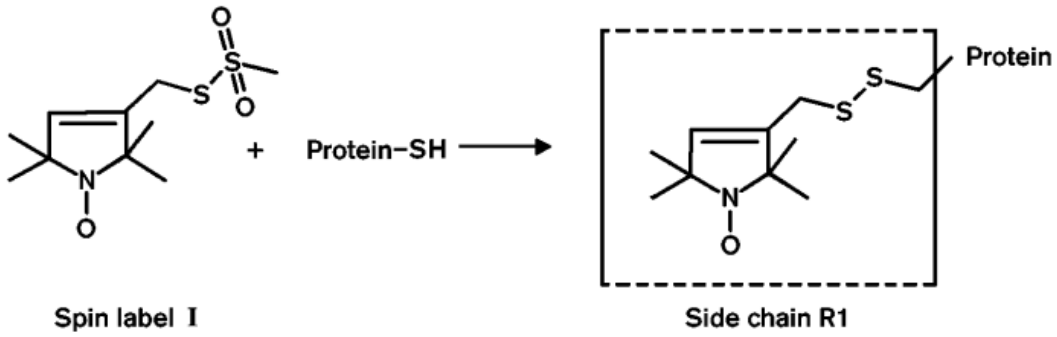


**Figure 2.11** The site-directed spin labeling (SDSL) reaction [47].

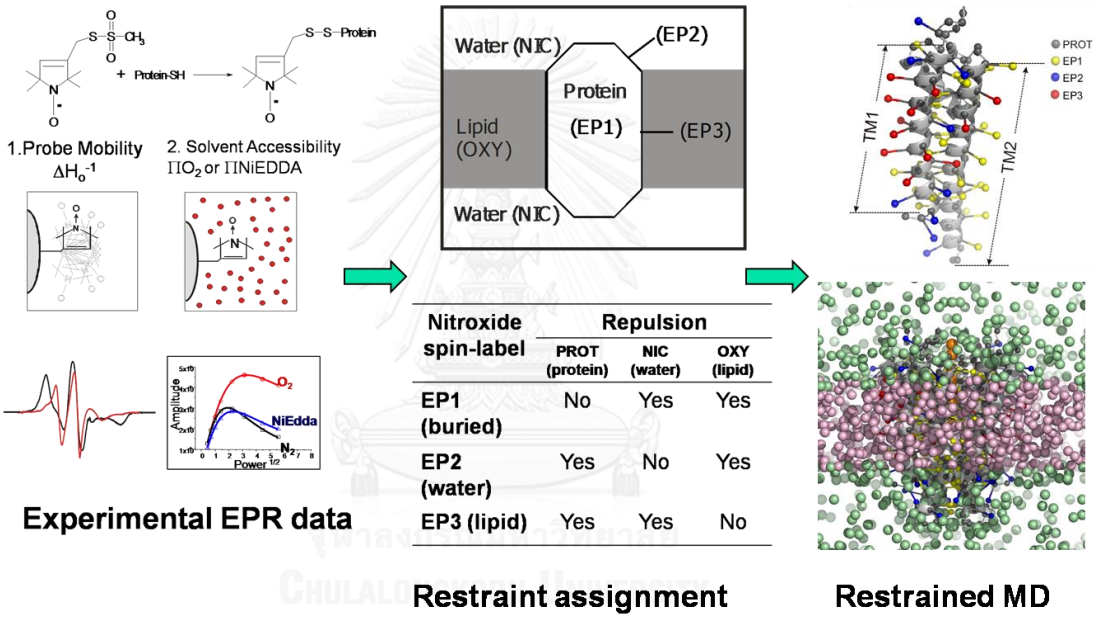


**Figure 2.12** The structural calculation process by means of PaDSAR apporach.

Structure calculations using PaDSAR method considered various types of interactions obtained from pseudoatoms introduced into the system. There are three types of pseudospin; EP1 for buried pseudospin residue, EP2 for water-exposed residue and EP3 for lipid-exposed residue. These pseudospins are mainly derived from the interpretation of SDSL/EPR accessibility parameters. During the PaDSAR calculation, these pseudospin interacts to three types of pseudoatom environment; OXY for $O_2$ molecule in the lipid bilayer, NIC for NiEDDA molecule outside the membrane and PROT for protein backbone (Figure 2.12). The restraint energy from the interaction

between pseudospin and pseudoatom environment is computed in a form of Lennard-Jones pair potential functions.

## 2.7 Objectives

1. To construct structural models of KvAP-VSD in resting (Down) configurations based on the SDSL/EPR data (from the cooperation with the Perozo's group, University of Chicago).

2. To investigate structure and dynamic properties Up and Down-state conformations of KvAP-VSD by means of MD simulations

## 2.8 Materials and method

### 2.8.1 Hardware

Personal computer (PC), Notebook, and High-performance computer cluster "Pheonix" located at Computational Chemistry Unit Cell (CCUC) laboratory, Department of Chemistry, Faculty of Science, Chulalongkorn University

### 2.8.2 Softwares

**CHARMM c35b6:** CHARMM or Chemistry at HARvard Molecular Mechanics is a MD program developed by Martin Karplus and his group at Harvard [49]. This program is widely used for studying in biological MD simulation system, moreover, it contains the force field parameters compatibly used for calculating the potential energy with other alternative MD simulations programs.

**NAMD 2.8b:** NAMD or Nanoscale Molecular Dynamics program is a MD simulation package for large biomolecular systems. It is a non-commercial use by individuals, academic institutions and corporations for in-house business purposes. It has been developed by the Theoretical and Computational Biophysics Group in the university of Illinois at urbana-Champaign [50].

**VMD 1.9:** VMD or Visual Molecular Dynamics is a program for modeling, visualizing, and analysis of biological systems. It is suitable to read Protein Data Bank (PDB) coordinate files, view and render a structure with general

representation styles, moreover, it can be used to display and analyze the trajectory files obtained from NAMD program. It is a freeware developed by the same group as NAMD program [51].

**Wordom:** Wordom is a versatile, user-friendly and efficient program for analyzing MD trajectories to gain the secondary structure, calculation of solvent accessible surfaces, elastic network model, motion cross correlations, protein structure network, shortest intra-molecular and inter-molecular communication paths, etc [52].

**APBS 1.2.1:** APBS or Adaptive Poisson-Boltzmann Solver is a free software package used for computing solvation energy according to the Poisson-Boltzmann equation (PBE). It can be performed in the electrostatic continuum system of the implicit solvent with using APBSmem program as a Java-based graphical interface integrated with PDB2PQR program which is a Python software package for converting PDB format to PQR format in which the PQR file is a PDB file that is added hydrogen coordinates and assigned atomic charges and radii of atoms [53-55].

### 2.8.3 Method for constructing structure models

The Up- and Down-state models were refined using PaDSAR method incorporating with the SDSL/EPR results obtained from Perozo's group. The Up-state model was taken directly from the previous work [31] which was used the x-ray structure of KvAP-VSD (1ORS.pdb) as the starting structure and refined with the EPR data of the 132 single-cysteine mutants (residues 20 – 151 of KvAP-VSD structure) in PCPG liposome at 0 mV.

The refined Up-state model was used as the starting structure to model the Down-state structure. Types of pseudospin were assigned to each residue as listed in Table 2.1. The virtual pseudoatom environment consisting of several hundreds of $O_2$ and NiEDDA denoted as OXY and NIC, respectively, were placed in the system then the restrained MD simulations were performed with CHARMM program. Finally, top ten candidate models which gave a good agreement with the experiment data were selected and the average coordinates of the selected candidates was used as the refined Down-state model.

**Table 2.1** Assignment of pseudospin types for the spin labeled residues in KvAP-VSD domain

| type | residue position |
|---|---|
| EP1 (n=48) | 25 31 32 35 36 39 41 42 44 45 46 55 58 59 61 62 66 69 72 73 75 77 87 88 90 93 94 95 96 97 98 99 100 101 103 105 113 122 126 133 136 137 140 141 142 143 144 145 |
| EP2 (n=19) | 28 76 79 80 81 82 85 86 89 104 107 108 111 112 114 116 119 146 147 |
| EP3 (n=41) | 22 23 27 30 33 37 40 43 47 48 49 50 52 54 57 60 63 64 67 68 70 71 74 91 92 102 109 110 115 117 118 121 124 125 127 128 129 130 131 132 134 |

The PaDSAR method was incorporated in the CHARMM program version c35b6. In the PaDSAR method, each residue of the protein was subjected to attach with two virtual particles, backbone and the pre-assigned spin-probe pseudospins (EP1, EP2, and EP). During the course of molecular dynamics (MD) calculations, restraint driving forces to spin-probe particles were governed by interactions with environment pseudoatoms, backbone, $O_2$ (OXY) and NiEDDDA (NIC).The VSD was modeled with all heavy atoms and all polar hydrogens with the extended-atom PARAM19 force field. The structure calculation was performed with several cycles of PaDSAR runs. Structures that gave an excellent agreement with experimental data were selected as a potential Down-state model. The reliability of models was further examined by molecular dynamics simulations and gating charge calculations. The flowchart of PaDSAR runs and the criteria of selecting PaDSAR model are shown in Figure 2.13.

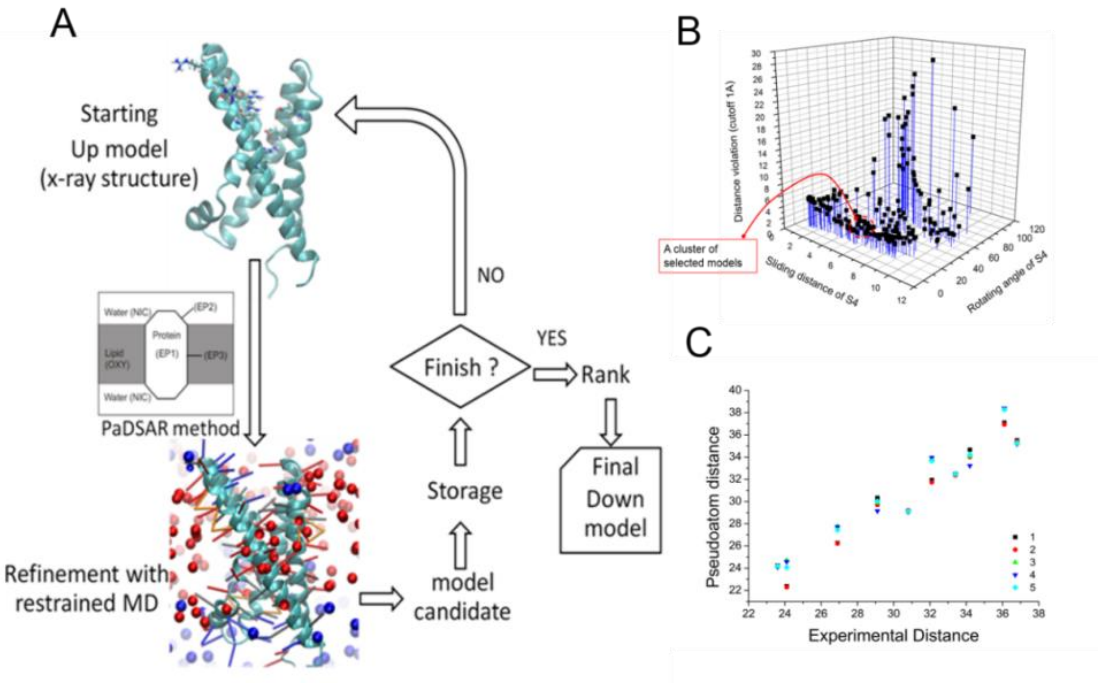


**Figure 2.13** A) Steps of structure modeling of Down conformation using PaDSAR [45] B) Evaluation of candidates based on distance penalty and C) Comparison between experiment and five obtained models.

### 2.8.4 Molecular dynamics details

MD simulations of KvAP-VSD in the lipid bilayer were performed according to the membrane protein tutorial [56]. The three simulation systems were individually conducted including (1) Up-state in a POPC bilayer at 0 mV denoted as Up-POPC (2) Down-state in a POPC bilayer at -70 mV denoted as Down-POPC (3) Down-state in a DOTAP bilayer at 0 mV denoted as Down-DOTAP in which all were hydrated with TIP3P water models. The system was solvated and neutralized with $Na^+$ and $Cl^-$ ions at 0.15 M using VMD's Autoionize plugin. The periodic box of each system had a dimension of ~80 Å x 80 Å x 80 Å. The studied simulation systems of all-atoms are demonstrated in Figure 2.14. All MD simulations were run using NAMD2.8b2 software with the timestep of 2 fs. CHARMM-22 and CHARMM-27 Force field parameters were employed for proteins and POPC, respectively. While structure coordinates and force field parameters of DOTAP were kindly provided from Andersson *et al*. [44]. To reduce the imaginary effect, periodic boundary conditions

were employed with the long-range electrostatic interactions calculated using the particle mesh Ewald summation method. A distance cutoff was set at 12 Å for short-range nonbonded interactions and to keep a fixed bond between a hydrogen atom and a heavy atom, the SHAKE and SETTLE algorithms were used. The minimization steps were run with restrained MD simulations in order to relax a non-appropriate geometry of the system starting from restraining protein and lipid headgroup atoms then restraining protein atoms while the others (waters, lipids and counterions) were free, finally, all restraints were removed following by an equilibration run. Afterwards, the production MD simulations were performed for 100 ns with using Langevin dynamics at a constant temperature of 298 K and a damping coefficient of 1 ps-1. Nośe-Hoove Langevin Piston was used for controlling the pressure at 1 atm, with a piston period of 200 fs and a damping time of 50 fs. Moreover, 4-independent MD simulations of Down-POPC system (50 ns) were conducted in order to validate the repeatability of MD simulations results. The details of MD simulations are summarized in Table 2.2.

**Table 2.2** Summary of the MD Systems for the Up- and Down-State Conformations of the KvAP-VSD.

| system | electrical field (mV) | total water molecules | total phospholipids | total atoms |
|---|---|---|---|---|
| Up-state | No | 7,025 | 130 | 40,722 |
| Down-POPC | -70* | 7,044 | 129 | 40,645 |
| Down-DOTAP | No | 6,808 | 129 | 39,189 |

*The approximately membrane potential (-70 mV) was achieved by applying an external electric field perpendicular to the membrane according to an equation (2.1)

$$E_z\left(\frac{\text{kcal}}{\text{mol Å e}}\right) = -23.06\ \frac{\text{V (volts)}}{L_z(\text{Å})} \qquad \textbf{(2.1)}$$

where $L_z$ is the length of the membrane along the z-axis.

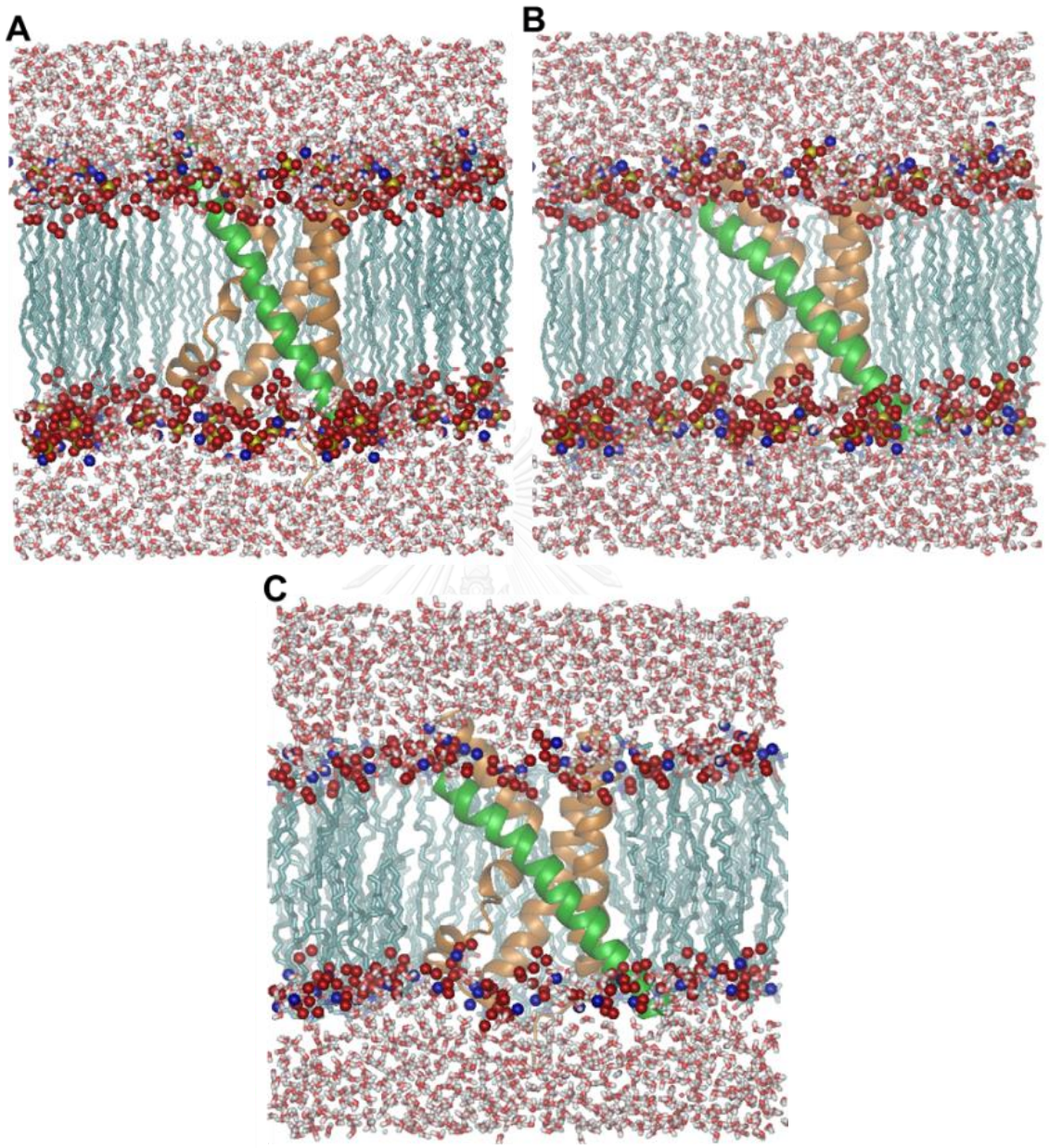


**Figure 2.14** (A) Up-POPC (B) Down-POPC (C) Down-DOTAP. Where the S4-helix (residue 117 to 151) is shown in the green color-part, S1-S3 helices are shown in orange, TIP3P-water models are shown with licorice models, yellow-balls are P-atoms, red-balls are O-atoms, blue-balls are N-atoms and cyan chains are acyl-chains of lipid bilayers.

### 2.8.5 MD trajectory analysis

MD trajectories were analyzed to observe the structural and dynamical properties along the simulations. The root-mean-square-deviation (RMSD), numbers of water molecules and positions of S4-arginines were computed using VMD scripts. Salt-bridge interactions and secondary structures were analyzed using WORDOM, python scripts and gnuplot programs. Salt-bridge interactions between arginine and acidic residues (aspartate or glutamate) were determined based on the basis of hydrogen bonding geometry of the distance between the guanidinium donor group of arginine and the acceptor carboxylate group of acidic residues. Water density maps were obtained from the VolMap plugin tool of VMD program.

### 2.8.6 Gating charge calculation

The movement of Arg residues along the S4 of KvAP-VSD according to the conformational change (under the influence of membrane electric field) results in the electrostatic energy difference called “gating charge”. To calculate the gating charge transfer, MD snapshots of Up-state and Down-state in POPC were used as the starting state and final state, respectively. The linearized Poisson-Boltzmann (PB) equation [57] using a continuum multidielectric treatment for implicit solvation models was used to compute the gating charge. All ions and solvent molecules were excluded then H-atoms, atomic charges and atomic radii of all atoms were assigned with PDB2PQR software. The partial charges and protein radii were taken from the PARSE parameter sets. The implicit solvent box containing water-membrane-water slab with a dielectric constant for membrane and protein was set at 2 ($\varepsilon_m = 2$) and a dielectric constant for water was set at 80 ($\varepsilon_w = 80$) [58]. The thickness of membrane was set at 20 Å. The ionic strength of bathing solution was 0.1 M with probe radius of 1.4 Å. The multigrid algorithm (containing coarse, medium and fine grids) was employed to generate dielectric, charge and ion accessibility maps of the protein. The membrane potential of the inner bath was varied from 77 to -77 mV and was kept at 0 mV for the outer bath as illustrated in

. The temperature was set at 298.15 K. All input parameters were set by using APBSmem and the calculations were done by using APBS program.

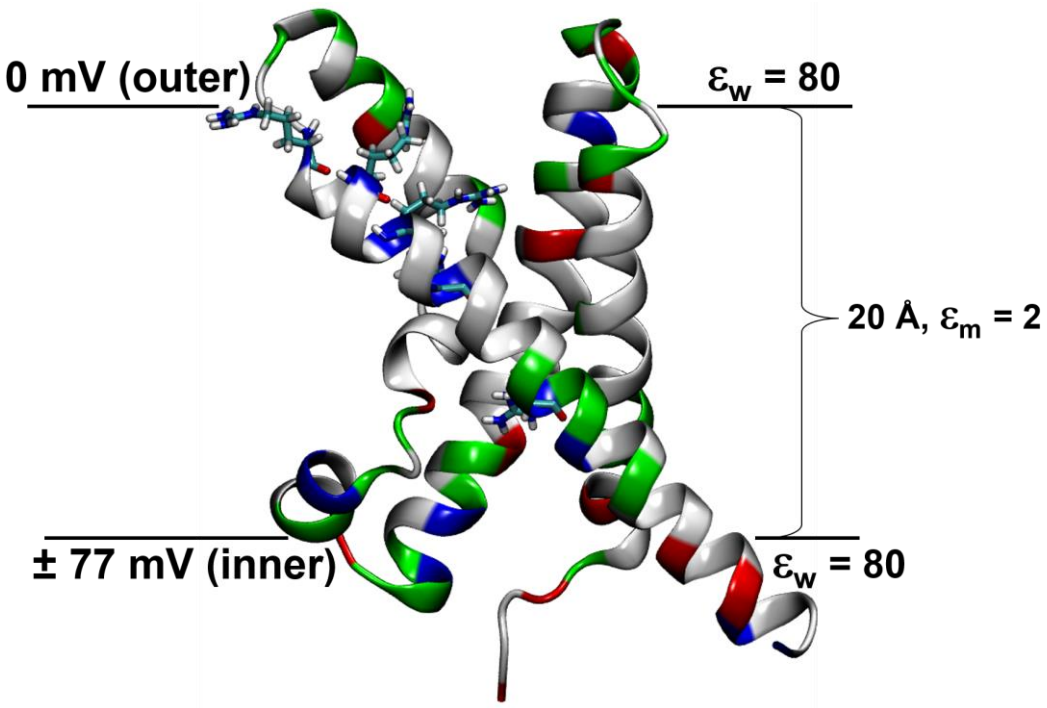


**Figure 2.15** Gating charge calculation of KvAP-VSD using PB solvent continuum method.

## 2.9 Results and discussion

### 2.9.1 Down-state model

Top-ten candidate models of Down-state conformation were selected with respect to the ranking best-fit with the experimental EPR data. An ensemble superimposition between Up-state and candidate Down-state models is shown in Figure 2.16. The S4-helices in the candidate models were the most affected parts moving in the same manner. The S4 motion underwent the downward tilt and slight rotation along its helical axis as a result of the new rearrangements of gating charge arginines (R117, R120 and R123) in the way of deeply distributing into the hydrophobic membrane. The effects of S4 displacement drove the switched salt-bridge interactions from R123-E107 in Up-state to R123-E45 and R120-E107 in Down-state, as shown in Figure 2.17.

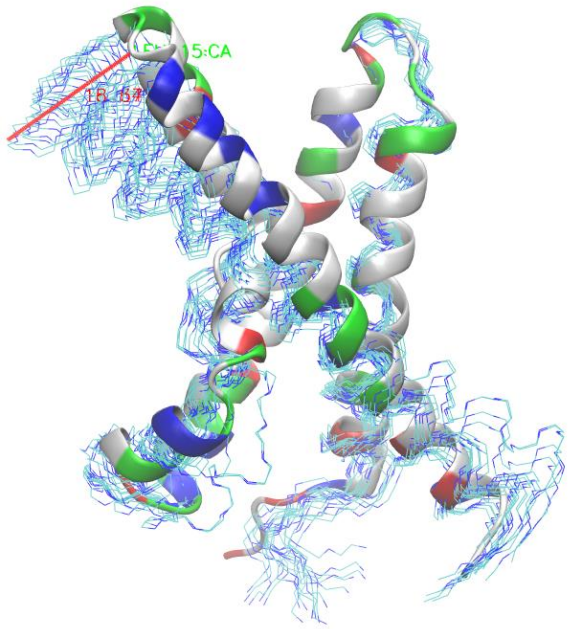

**Figure 2.16** An ensemble of candidate Down-state models (wireframe) superimposed onto Up-state model (cartoon).

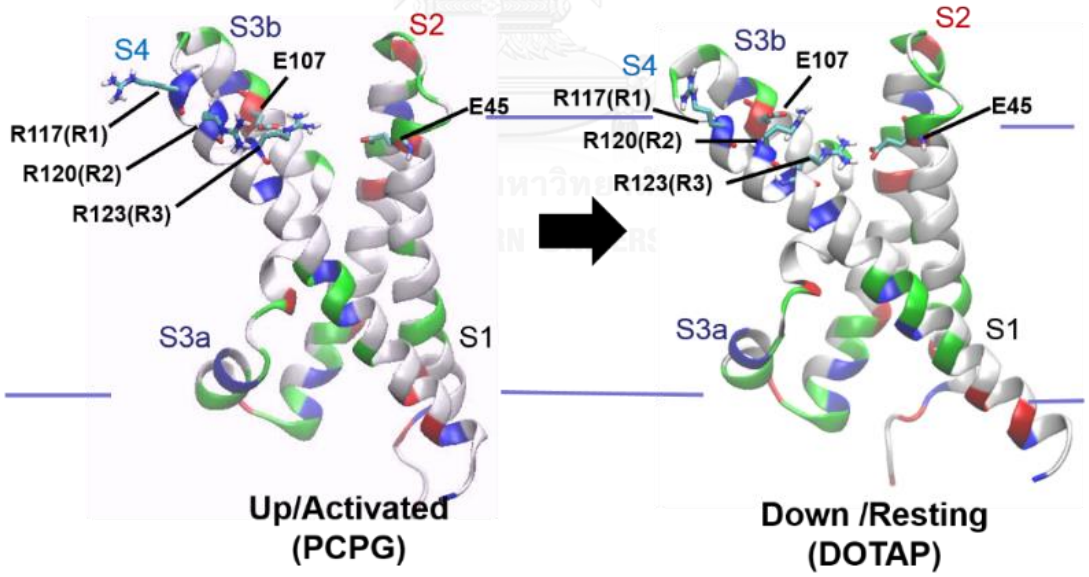


**Figure 2.17** KvAP-VSD models of Up-state and Down-state conformations illustrating salt-bridge interaction changes. Red color is for acidic residue, blue for basic residue, green for polar residue and white for non-polar residue.

### 2.9.2 Dynamics properties of KvAP-VSD from MD simulations

The backbone RMSD plot of the studied systems is shown in Figure 2.18(A). The backbone fluctuation was in a range of 1.5−3.0 Å compared with the starting structure indicating that all simulation systems had the structural and dynamical stabilities over 100-ns simulation time. In addition, MD simulations results were validated to observe the repeatability by performing 4-independent of Down-POPC system for 50-ns simulation time and the obtaining RMSD profiles are shown in Figure 2.18(B). The average RMSDs over the last 30-ns were calculated as reported in Table 2.3.

RMSD results are compatible among all studied systems indicating the stability and reliability of simulating systems. Moreover, RMSD values of each segment (as shown in Figure 2.19(A)) reveal the RMSD range of 1.0 – 4.0 Å incorporated with the secondary structure analysis (Figure 2.19(B)) depicting the helical structure stability of all segments with no significant break in the helix conformation in all systems.

จุฬาลงกรณ์มหาวิทยาลัย
Chulalongkorn University

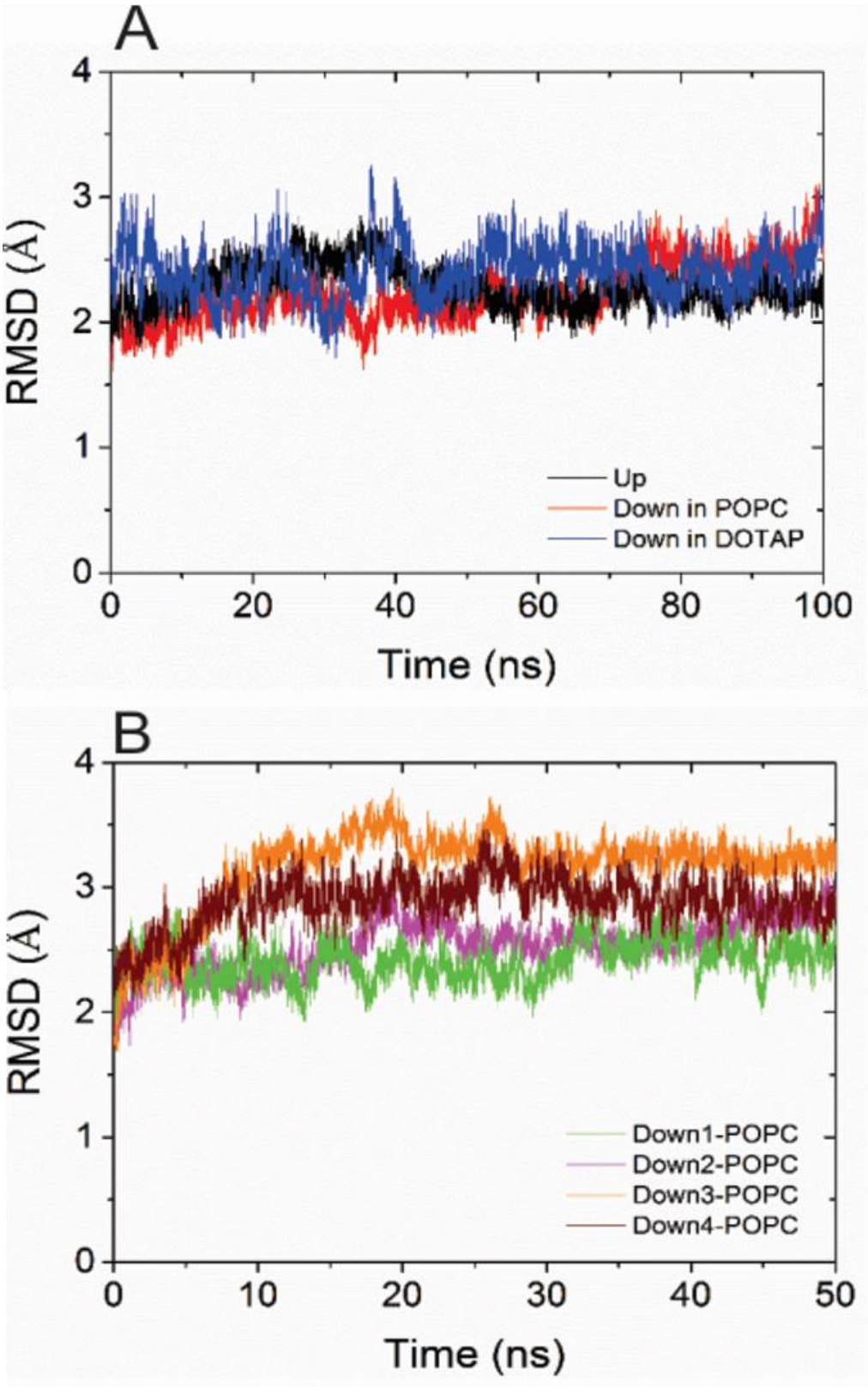


**Figure 2.18** (A) Backbone RMSDs over 100-ns simulation time (B) Backbone RMSDs of 4-independent Down-POPC runs for 50-ns.

**Table 2.3** Average RMSD values over the last 30-ns MD trajectories.

| system | average RMSD ± SD |
|---|---|
| Up-POPC (100-ns) | 2.23 ± 0.08 |
| Down-POPC (100-ns) | 2.50 ± 0.14 |
| Down-DOTAP (100-ns) | 2.42 ± 0.16 |
| Down-POPC (50-ns x 4) | 2.64 ± 0.11, 2.44 ± 0.15, 3.26 ± 0.10, 2.94 ± 0.15 |

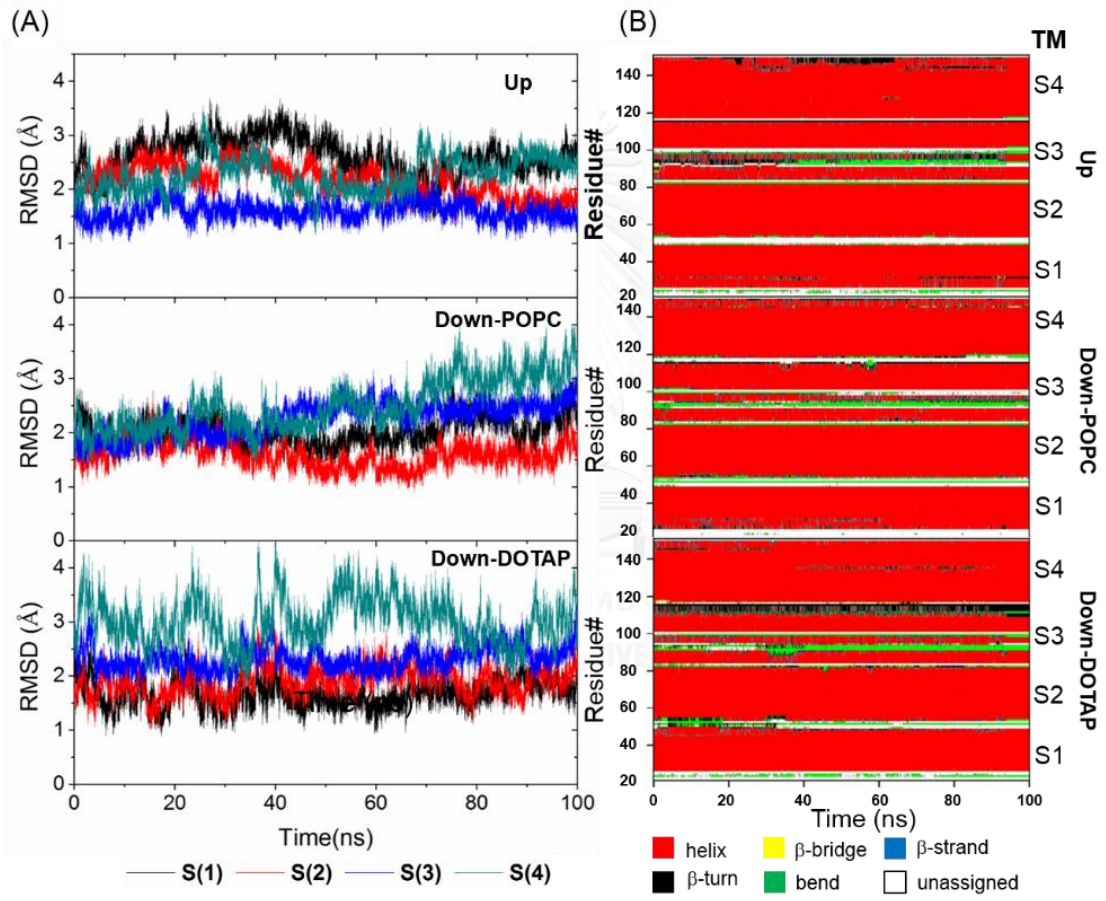


**Figure 2.19** (A) RMSD of each segment (S1-S4) (B) secondary structure analysis as a function of simulation time.

### 2.9.3 Shapes of water crevices in the VSD-core

Water molecules were found to diffuse from both sides into the VSD core forming a narrow water-filled like pore which provides the different shapes as shown in Figure 2.20.

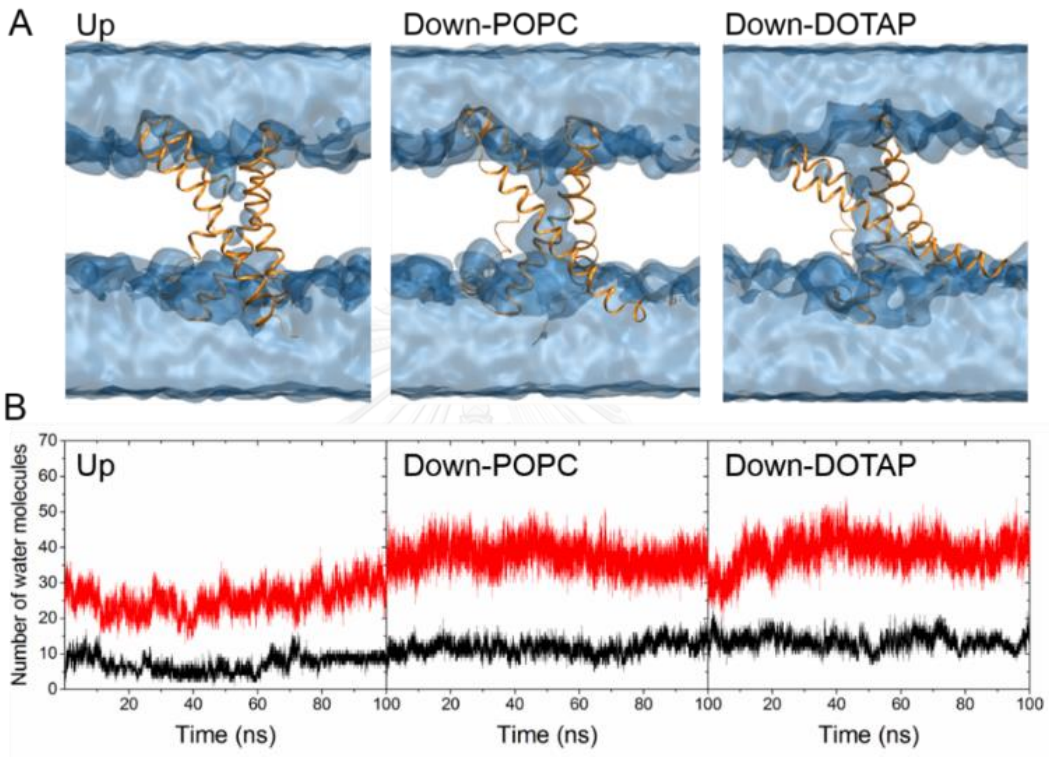


**Figure 2.20** The accessible water crevices in the Up- and Down-state conformations of KvAP-VSD. (A) MD snapshots of the different shapes of water-crevices in the VSD core (the VSD is shown by a ribbon and the accessible-water is shown as a transparent surface). (B) Number of water molecules in the extracellular (black line) and intracellular (red line) as a function of time.

Besides, the number of accessible water molecules was counted with the defining distances along z-axis of 15 and -15 Å for extracellular and intracellular sides, respectively. In particular, in the intracellular the number of accessible water molecules in the Down-POPC and Down-DOTAP simulations is found to be greater than that in the Up-state conformation (Table 2.4). These results are consistent with the observed

experimental EPR data, which showed differences in the accessibilities of nickel-ethylenediamine diacetate (NiEDDA) to the S4 residues for the VSD reconstituted in two different lipid compositions [31]. The NiEDDA accessibility into the intracellular end of S4, in a DOTAP bilayer, was greater than in a mixed phosphatidylcholine/phosphatidylglycerol (PCPG) bilayer. This indicates that the dielectric constant increases in the lower crevice in the Down-state conformation to reduce the hydrophobic barrier when the gating charged arginines moving as a result of conformational change.

**Table 2.4** Average number of water molecules in extracellular and intracellular crevices of KvAP-VSD in studied systems over the last 20-ns MD trajectories.

| | Up-state | Down-POPC | Down-DOTAP |
|---|---|---|---|
| no. water in extracellular | 8.9. ± 0.9 | 13.1 ± 1.7 | 13.0 ± 1.6 |
| no. water in intracellular | 28.9 ± 3.2 | 35.8 ± 2.9 | 38.8 ± 3.3 |

Furthermore, the water density maps (Figure 2.21) of the studied systems showed the different shapes of the water-crevices within the VSD. Both Down-POPC and Down-DOTAP revealed the wider density at the lower crevice, indicating more water penetration in the intracellular side of the VSD. It is worth nothing that some snapshots of Up-POPC simulations displayed the zero water density at some regions. This is because there were salt-bridge interactions between the S4 arginines and the negative countercharges forming a constriction that prevents the penetration of water molecules across the bilayer. Whereas, in both Down-state conformations, the water density apparently deeps into the hydrophobic environment. Thus, it is clearly noticed that the hydrophobic thickness of the membrane bilayer in both Down-state systems was shorter than in the Up-POPC system. This implies that the fluidity of membrane has been readjusted during the conformational change resulting in a shorter bilayer-thickness to facilitate the movement of S4 arginines across the membrane electric field. Taken together, the water-crevice changing in between Up- and Down-

conformations supports the concept that refocusing of the electric field maintains the stability of the gating charged arginines.

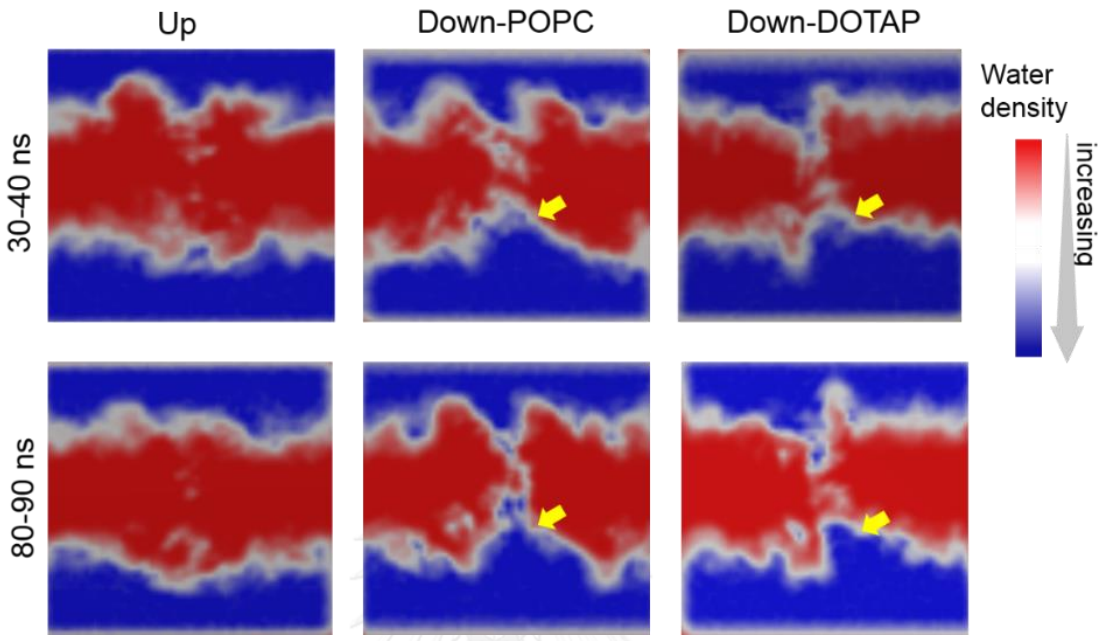


**Figure 2.21** The MD-derived water density in the Up- and Down-state conformations of the KvAP-VSD. The yellow arrows indicate a wider region of water density at the intracellular water crevice.

### 2.9.4 Distance displacement of S4 arginine residues

With respect to the magnitude of the S4 arginine movements as a result of water-crevice shape changes, the distance displacement of S4 arginine residues were determined as demonstrated in Figure 2.22. One can notice that S4 arginine residues in the Down-POPC and Down-DOTAP were distributed deeper inside the membrane compared to those in the Up-state conformation. In particular, the R123, R126 and R133 residues were deeper inside the hydrophobic region than R117 and R120 which were exposed near the water-lipid interface in the Up-POPC system.

Moreover, Table 2.5 shows that these 5 arginines in the Down-state confirmation move towards the membrane bilayer with the magnitude of 4–5Å (relative to the position of arginines in the Up-state conformation) which is corresponding to the translocation movement.

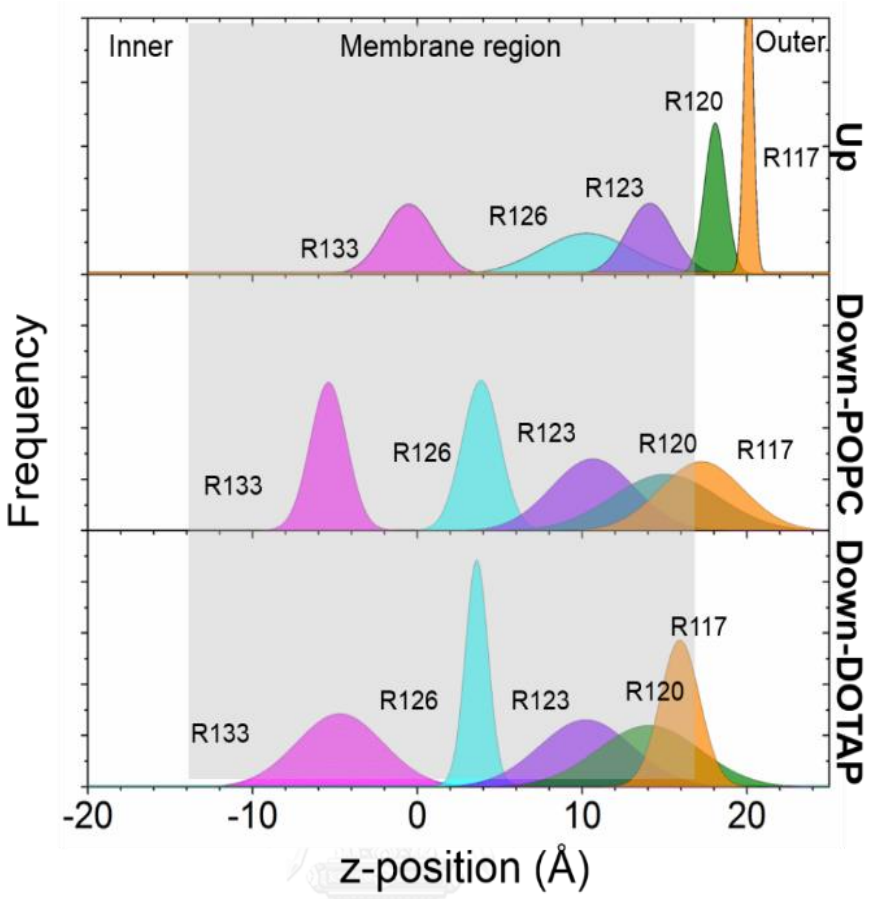


**Figure 2.22** Gating charge arginine positions in the studied systems (extracted from a mass density profile of the last 20 ns MD trajectories).

จุฬาลงกรณ์มหาวิทยาลัย
Chulalongkorn University

**Table 2.5** Average distance displacement of S4-arginine residues along z-axis comparing Up vs Down-POPC and Up-POPC vs Down-DOTAP.

| | distance displacement (Å) | | | | |
|---|---|---|---|---|---|
| | R117(R1) | R120(R2) | R123(R3) | R126(R4) | R133(R5) |
| Up vs Down-POPC | 2.7 | 3.1 | 3.5 | 6.1 | 4.8 |
| Up vs Down-DOTAP | 4.0 | 4.1 | 3.9 | 6.7 | 4.2 |

### 2.9.5 Change in salt bridge interactions

Salt-bridge interactions between the positively charged arginine residues on the S4 helix and the negative countercharge residues located on the S1, S2, S3a and S3b helices were analyzed. From the MD trajectories, hydrogen bond distances involving the S4 arginine residues R117, R120, R123, R126 and R133 were considered. The distance profiles (Figure 2.23), in Up-POPC, reveal three salt-bridge pairs involving R123, R126 and R133 and the guanidinium group of R133 formed a stable salt bridge with D62 whereas the R123 side chain was placed close to E107. The salt-bridge between the R123-E107 pair is considerably weak as the color changes back-and-forth between blue and green (sometimes red), in addition, the R126 side chain forms a salt bridge with E107 while the R117 and R120 were water-lipid exposed and so do not engage in salt bridge interactions. In contrast, both Down-POPC and Down-DOTAP systems demonstrated changes in the gating charged environments. A large distance separation (> 3.5Å) between R133 and D62 of the S2-helix suggested that this salt-bridge interaction pair was not formed, instead, the salt-bridge pair was changed to R133-E93. For R126, the salt-bridge formation with E107 of the S3-helix observed in the Up-POPC was no longer detected in the Down-state systems. Another important change in the disruption and formation of salt-bridge interactions involving the S4-arginine residues was with R123. The weak salt-bridge interaction of R123-E107 pair detected in the Up simulation was found to switch as a R123-E45 pair in Down-POPC, however, this salt-bridge pair became stable in Down-DOTAP. Additionally, a new salt-bridge pair of R120-E107 was observed in both Down-POPC and Down-DOTAP. It should be noted that the R120 in Up-POPC was not involved in salt-bridge interactions with residues in VSD, rather, it mainly interacted with phosphate head-group of the lipid-membrane and water molecules. These salt-bridge interactions and high accessible water-crevices occurring in Down-state conformations provided a suitable environment in stabilizing the gating charges deep into the membrane. Overall, these findings are in accord with the previous MD simulation studies [43, 44].

จุฬาลงกรณ์มหาวิทยาลัย
CHULALONGKORN UNIVERSITY

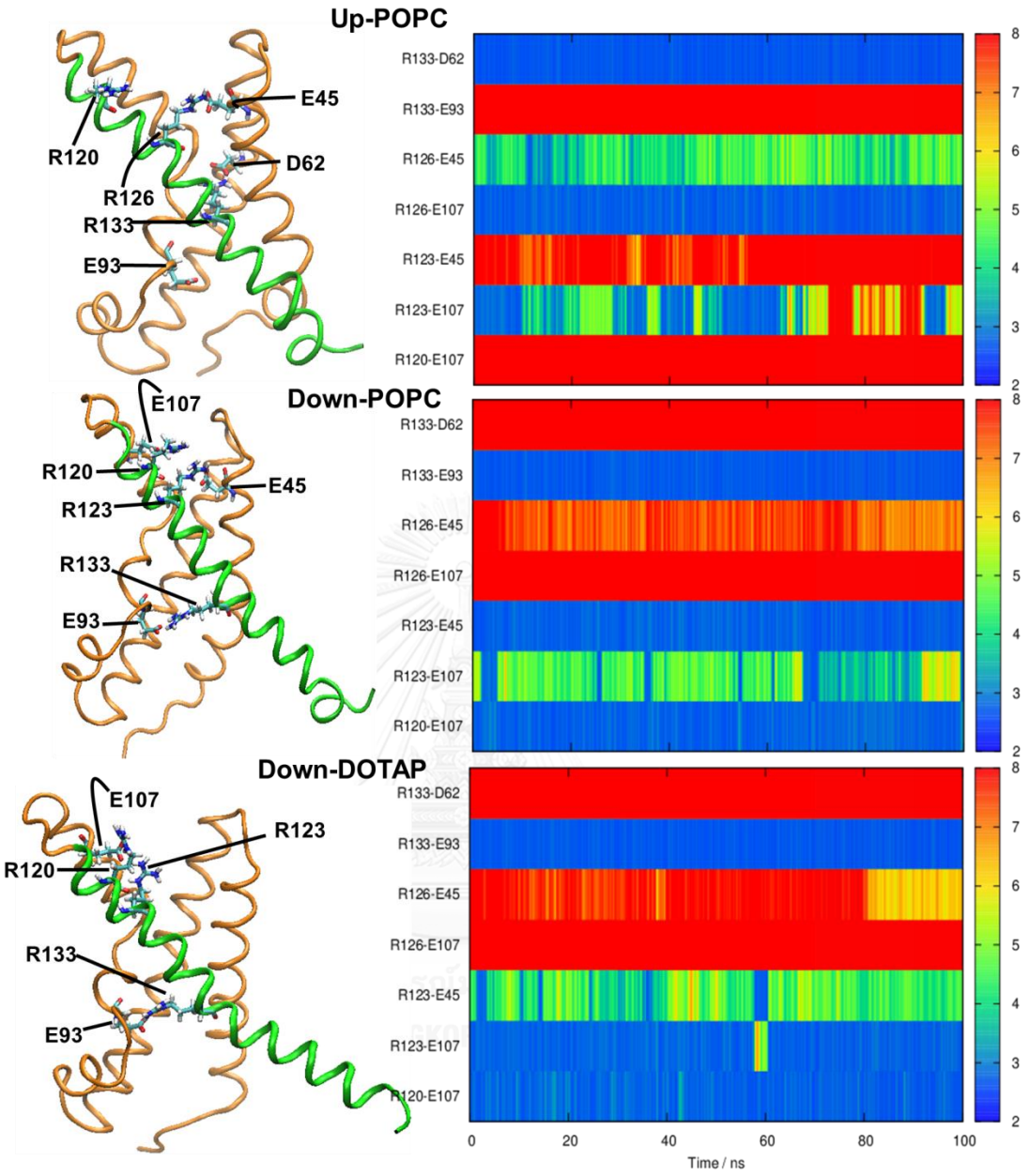


**Figure 2.23** Salt-bridge interactions involved with S4-arginine residues in the Up, Down-POPC and Down-DOTAP (left) and the distance profile (right), where D-A = the distance between the hydrogen donor and acceptor atoms.

### 2.9.6 Gating charge calculations

Comparing between Up-POPC and Down-POPC, the S4-arginines were located in different positions which result from the electrical potential change. The amount of work driving the movement of sensing charged arginines as called the gating charge can be calculated by using APBS program. In this study, ten snapshots of the Up and Down-POPC simulations were employed to compute the difference in energy versus the voltage changes (from -77 to +77 mV) as shown in Figure 2.24 which reveals the energy difference of about -5.6 $k_BT$ at -77 mV and this increases as the membrane potential increases. The slope of this voltage dependence curve is the gating charge which was found to be 2.79 ± 0.09e. This calculated gating charge is consistent with the experimental estimates of 12–13e measured for the Shaker $K^+$ tetrameric channel, which is equivalent to ~3 e per monomer [59].

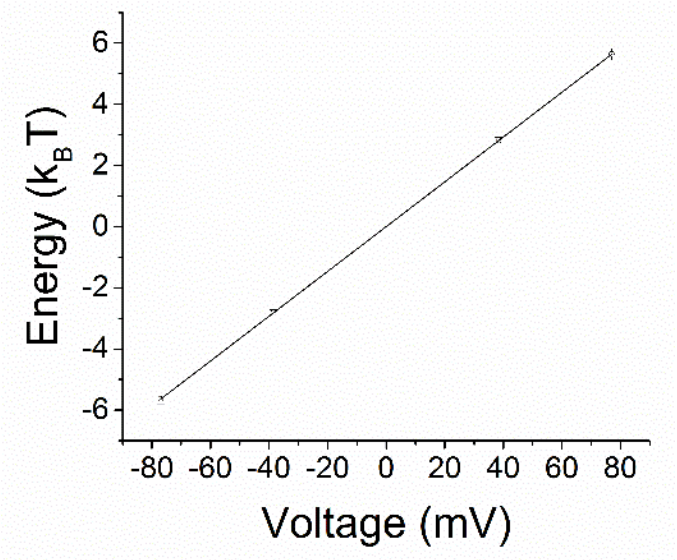


**Figure 2.24** Voltage dependence graph calculated from the electrical potential energy difference between Up-state and Down-state conformations in the membrane potential range from -77 to +77 mV.

## 2.10 Conclusion: KvAP-VSD study

The structural and dynamical properties of the isolated KvAP-VSD channel were evaluated in the Up- and Down-state conformations by means of MD simulations. The results showed the stability of the tertiary and secondary structures of the four transmembrane segments. The different shapes of the water crevice in the voltage sensor core were observed during the simulations where the Down-state conformations (Down-POPC and Down-DOTAP) provided a large water penetration through the intracellular side of the VSD to increase a dielectric constant of bilayer incorporated with the readjusted membrane thickness resulting in an accommodation of a Downward movement of the S4-arginines towards the resting state. Besides, the stability of the sensor in the Down-state conformation was supported by a change of salt-bridge networks involving the S4 arginine residues. The results of the gating charge transfer calculation from the MD simulations were in good agreement with electrophysiology experiments for the $K_v$, supporting the validity of this MD analysis.

จุฬาลงกรณ์มหาวิทยาลัย
Chulalongkorn University

# CHAPTER III: STRUCTURE, DYNAMICS AND ION SELECTIVITY OF MAGNESIUM ION CHANNEL BY A COMPUTATIONAL STUDY

Magnesium ion ($Mg^{2+}$) is the most abundant divalent cation in organisms. It serves as an essential metal ion in many physiological and biological processes. This divalent metal ion has a unique property. For example, it is the smallest ion among other biological cations with an ionic radius of 0.76 Å (Table 1). The first hydration shell strongly forms an octahedral geometry with the $Mg^{2+}$-oxygen (water) distance of ~ 0.210 nm obtained from X-ray diffraction results and MD simulations [60, 61]. The hydrated $Mg^{2+}$ exhibits a slow water exchange rate (~$10^5$ waters/s) with the highest effective hydrated volume (~ 400 folds) [62]. It can be noted that the fully hydrated $Mg^{2+}$ ion is the largest among other biological ions. Therefore, it can be implied that the transport mechanism of $Mg^{2+}$ across the membrane is different from other ion channel systems.

Owing to the importance of $Mg^{2+}$, the $Mg^{2+}$ homeostasis has long been a subjective of intense research. The understanding of magnesium transport system in prokaryotes is significant because it can be used as the fundamental information for further studying in magnesium transport system in eukaryotes such as the homologue of Mrs2 (mitochondrial magnesium channel) and Alr1 (aluminium resistance protein, the major $Mg^{2+}$ uptake system in yeast plasma membranes) [63]. In bacteria, there are three systems that can regulate the $Mg^{2+}$ translocation i.e. MgtA/B, MgtE and CorA [64]. Among them, CorA has proposed to be the primary $Mg^{2+}$ uptake system. CorA or cobalt resistance protein was first identified by Maguire and co-workers [65]. CorA does not mediate only $Mg^{2+}$, but also $Co^{2+}$ and $Ni^{2+}$ [66].

## 3.1 Literature review

In 2006, there were three crystal structures of *Thermotoga maritima* CorA (TmCorA) published by individual group [67-69]. They were crystalized in the presence of $Mg^{2+}$. It has been suggested that these crystal structures correspond to the closed-state conformation. In 2012, Pfoh *et. al*. [70] reported TmCorA structures in both presence and absence of $Mg^{2+}$ ions ($Cs^{+}$-presence instead). All reported structures are similar and are in the resolution range of 2.9–3.9 A˚.

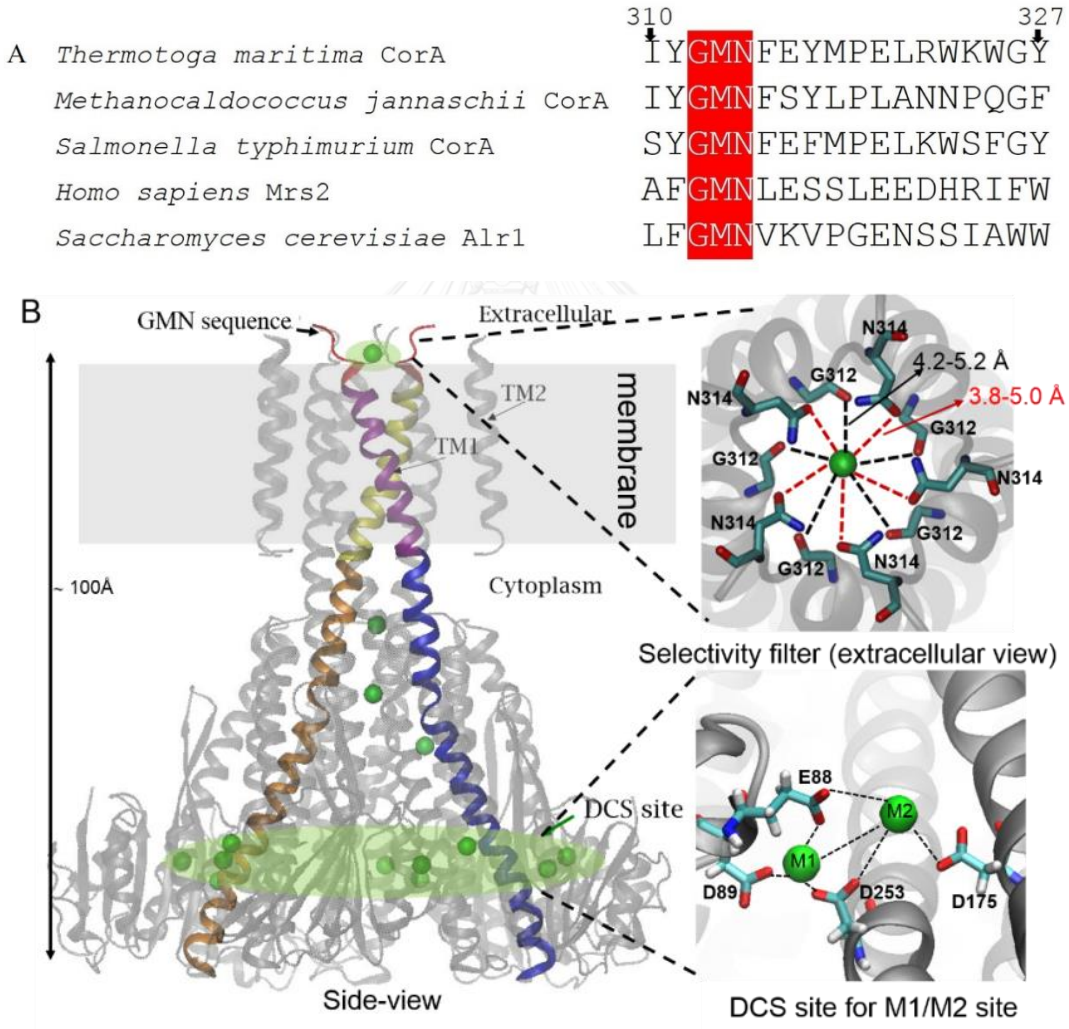


**Figure 3.1** (A) Sequence alignment of the TmCorA family where the numbering is based on the TmCorA sequence. (B) Crystal structure of TmCorA channel (4EED.pdb) highlighting the GMN motif at the extracellular loop and one of the five M1/M2 binding sites at the DCS site.

TmCorA is a cone-shaped pentameric protein consisting of four domains i.e., cytosolic domains, stalk helices, inner and outer transmembranes (TM1 and TM2) and periplasmic loops. It forms a long ion conductive pore with ~40 Å in length. The pore is defined by the assembly of inner transmembrane helices connecting to stalk helices [63]. The TM2-domains face with the hydrophobic lipid bilayers and connects to the TM1-domains by the periplasmic loops. The periplasmic loops contain highly conserved MPEL and YGMNF motifs which have been proposed that they might act as the selectivity filter (SF). Besides, the cytoplasmic domain exhibits a functional significance. The crystal structure reveals that there are two intracellular $Mg^{2+}$-binding sites (M1 and M2) in between subunit in the cytoplasmic domain. The M1 site is coordinated nearby the side chain of two acidic residues, D89 and D253 while the M2 site is ~7 Å far from the M1 site. The M2 site is coordinated with the side chain of E88, D175 and D179. This binding site is called as the divalent cation sensor (DCS).

Chakrabarti *et al.* (2010) [71] performed MD simulations on the TmCorA systems in the lipid bilayer to investigate the effect of $Mg^{2+}$-bound to metal binding sites of TmCorA on the Mg transport mechanism. Their results showed that $Mg^{2+}$ removal affected the conformational fluctuation and the pore diameter of the hydrophobic residues was wider with the widest at the methionine constrictions (M291 and M302). This region is called the MM stretch which can facilitate the transport of $Mg^{2+}$ and the hydration. They proposed the gating mechanism as the iris-like dilation at the MM stretch of TmCorA pore (Figure 3.2).

จุฬาลงกรณ์มหาวิทยาลัย
CHULALONGKORN UNIVERSITY

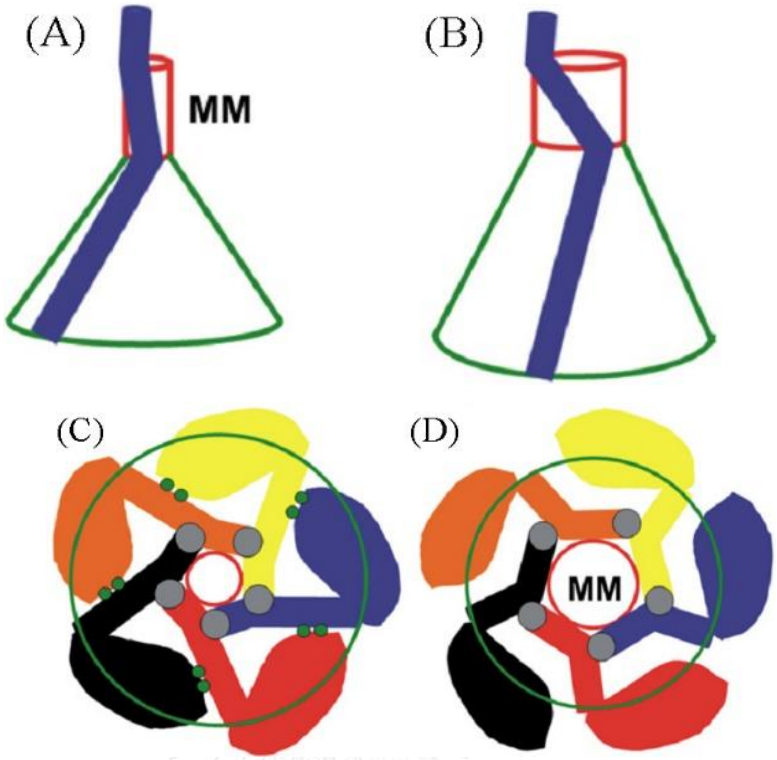


**Figure 3.2** Cartoon representation of the iris-like mechanism of pore Dilation [71]. (A) Side view of the closed state. (B) Side view of the open state. (C) Top view of the closed state. (D) Top view of the open state. For clarity, only one stalk helix is shown in the side view.

In 2012, Wapeesittipan [72] studied MD simulations of TmCorA of closed-state and open-state conformations. The closed-state structure was from the x-ray crystal structure (2IUB.pdb) with a periplasmic loop modeled by Dalmas's (2010) [73]. The open-state structure was modeled from closed-state structure using PaDSAR approach from EPR dataset. After performing MD simulations for 100 ns, the 12-$Mg^{2+}$ -bound closed-state model showed the greatest structural stabilities, whereas the simulation of open-state showed the most deviate conformational changes which loosed structural symmetry of pentamer. The researchers also proposed the open gating mechanism that underwent the scissor-like motion (Figure 3.3) with the narrower cytoplasmic domain incorporating the wider of the hydrophobic constriction pore to permeate the hydrated $Mg^{2+}$ ions.

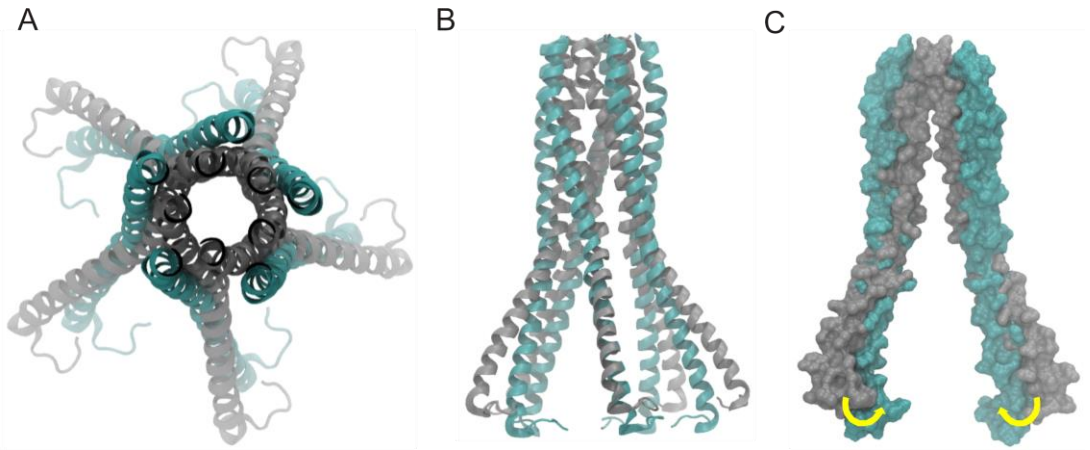


**Figure 3.3** Conformational change between closed (grey) to open (cyan) (A) Top view. (B) Side view. (C) Side view as a scissor-like motion of the molecular surface representation [72].

Dalmas *et al.* (2014) [74] examined the permeation and selectivity of TmCorA by using electrophysiological recording and mutagenesis studies. They proposed that in the absence of extracellular $Mg^{2+}$, TmCorA exhibits a nonselective property by allowing the permeations of cations along their electrochemical gradients. But when the extracellular $Mg^{2+}$ concentration increases, the GMN motif can selectively bind with $Mg^{2+}$ and block other ions. Moreover, when the extracellular $Mg^{2+}$ concentration is higher, $Mg^{2+}$ can flow continuously via electrostatic repulsion as called a block and repulsion mechanism (Figure 3.4).

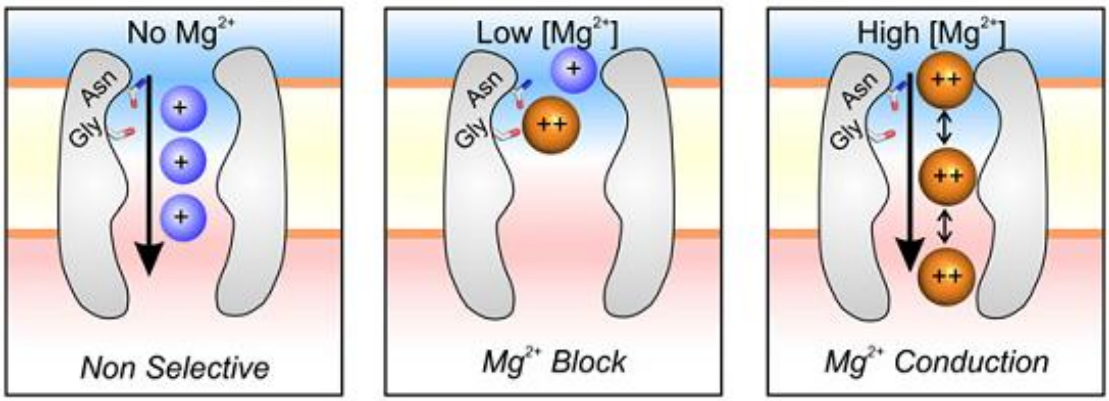


**Figure 3.4** A block and repulsion mechanism of TmCorA [74].

In 2014, Dalmas *et al.* [75] investigated a more detail insight into molecular basis of $Mg^{2+}$-gating in TmCorA based on their previous work using EPR spectroscopy,

electrophysiology and MD simulations. The conformation of liposome-reconstituted CorA in two conditions of with and without $Mg^{2+}$ was determined by means of the refinement of EPR data with the PaDSAR approach to achieve the three-dimensional (3D) models of both closed and open structures. Incorporating with the electrophysiological results, they proposed the $Mg^{2+}$-driven negative feedback mechanism as illustrated in Figure 3.5 that $Mg^{2+}$ ion acts as a ligand to drive a non-conductive conformation of CorA but when $Mg^{2+}$ is low, the protein can be triggered to the conductive conformation by a widespread rearrangements resulting in pore-expanding to permeate $Mg^{2+}$ flowing Down its electrochemical gradient.

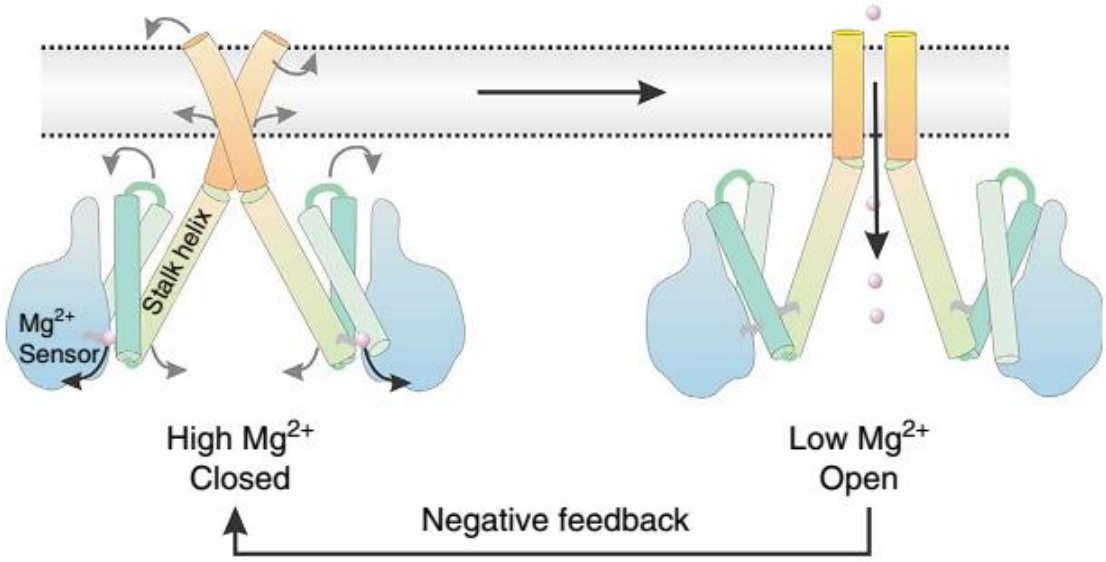


**Figure 3.5** Negative feedback mechanism of $Mg^{2+}$-dependent gating in CorA [75].

According to published crystal structures of TmCorA in the closed-state conformation, they reveal a similar symmetrically structural architecture comprising of the GMN motif, TM1, TM2, stalk helix and cytosolic domain forming a funnel-shaped pentamer. Each part has been proposed that functions differently as the selective filter (SF) of the GMN motif, the hydrophobic conduction pore of TM1 and the regulatory site at DCS in cytoplasmic domain. Nevertheless, the distinct chemistry of $Mg^{2+}$ preferring the rigid coordination with octahedral oxygen-containing ligand in the inner shell causes the confusing question that how does the hydrated $Mg^{2+}$ can be discriminated from other ions and transported through the highly conserved hydrophobic pore for a long distance (~40 Å) ?. At GMN motif, the binding distances

between $Mg^{2+}$ and the N314 side chain together with the carbonyl group of G312 (~4 Å of each distance) and asymmetrically coordinated of one N314 side chain are observed suggesting partially hydrated $Mg^{2+}$ ion bound at the GMN selective filter [70, 76, 77] but how each interaction can occur only for $Mg^{2+}$ recognition is still quested.

### 3.2 The selectivity filter of CorA protein

Moomaw *et al.*, 2010 [62] studied on the functional mutagenesis of the other part from periplasmic loop of StCorA (CorA from *Salmonella enterica* serovar Typhirium) which consists of $^{281}$EFMPELKWS$^{298}$ residues (including the MPEL motif) that corresponds to $^{316}$EFMPELKWS$^{324}$ in TmCorA. They concluded that the 2 acidic residues in this part were not involved with the electrostatic interaction of $Mg^{2+}$ and proposed that $Mg^{2+}$ prefers to initially bind in the fully-hydrated form agreeing with the selective function of CorA for strongly binding with a fully-hydrated $Mg^{2+}$ analogue, Co(III)hex [78].

This supports the selectivity function of the GMN motif that also presents in all CorA family but there is no the MPEL motif in MjCorA-crystal structure (CorA from *Methanocaldococcus jannaschii*) which is still the Mg-selective channel and reveal the locating of $Mg^{2+}$ in the GMN ring with the same distance range (~4 – 5 Å) to TmCorA-structure which supports the idea that the GMN residue should form the second shell ligands with the partially hydrated $Mg^{2+}$ .

In 2013, Palombo *et al.* [79] conducted the structure−function analysis focusing on the pentamer integrity and $Mg^{2+}$-uptake of TmCorA when G312, M313 and N314 in the extracellular loop were mutated individually. They found that this motif was involved with both structural and functional properties by which G312 is related to the $Mg^{2+}$-uptake and is essential for pentamer integrity while N314 is important to both properties.

In aqueous solution, $Mg^{2+}$ favors to coordinate with 6 water molecules in the first solvation shell and with ~12 water molecules in the second solvation shell as obtained from the theoretical study [60] forming a fully hydrated $Mg^{2+}$ as displayed in Figure 3.6 with the average distance of Mg-O$^{1st}$ shell of 2.10 Å and Mg-O$^{2nd}$ shell of 4.13 Å.

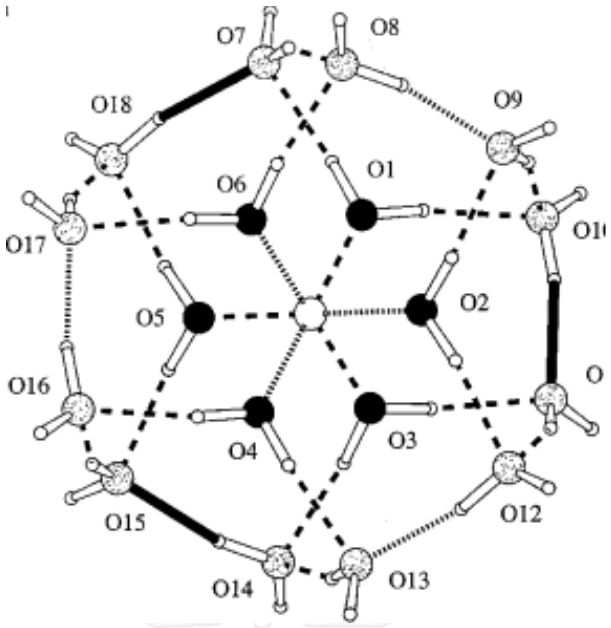


**Figure 3.6** Optimized structure of $Mg(H_2O)_6 \cdot (H_2O)_{12}$ complex [60].

Unfortunately, due to the current medium resolution of TmCorA crystal structures (2.9 – 3.9 Å), the coordinates of water molecules are absent. Therefore, it is interesting to verify the water arrangement of $Mg^{2+}$ in the motif of TmCorA (TmCorA-SF). This could address the questions about (1) how the conserved GMN residues interact with $Mg^{2+}$ and (2) how different between the coordination structure of $Mg^{2+}$ in the TmCorA-SF and in aqueous solution.

## 3.3 Objective

To investigate structure, dynamics and ion selectivity of TmCorA $Mg^{2+}$ channel by means of MD simulations and QM/MM study

## 3.4 Materials and method

### 3.4.1 Hardware

Personal computer (PC), Notebook and High-performance computer cluster “Pheonix” located at Computational Chemistry Unit Cell (CCUC) laboratory, Department of Chemistry, Faculty of Science, Chulalongkorn University

### 3.4.2 Softwares

NAMD, VMD (as described in Chapter II)

**Gaussian09 and Gaussview05:** Gaussian program is the computational program using for electronic structure calculation. It was first developed by John Pople and his group at Carnegie-Mellon University, however, the license has been changed to Gaussian Inc., since 1987. While Gaussview program.is used for visualizing and manipulating the structure file [80, 81].

### 3.4.3 Structure models

The TmCorA crystal structure (PDB ID code 4EED) was used. The missing periplasmic loop (residue number from 316 to 325) was modeled by using the loop prediction program LOOPY [82]. All missing hydrogens atoms were added using the PSFGEN plugin in VMD. Side-chain ionization states at pH 7 were assigned based on $pK_a$ calculations using PROPKA [83]. In addition, we constructed a truncated TmCorA-SF model containing a $Mg^{2+}$ ion and periplasmic loop residues (residues 310 to 327) to reduce the size of the simulated systems and improve the sampling calculations by focusing on the coordination shell structures of $Mg^{2+}$ in the TmCorA-SF.

To investigate the effect of $Mg^{2+}$ ions in the DCS sites on the structure of the TmCorA-SF, three different model simulation systems were conducted including the full-length TmCorA (denoted as FLCorA), the full-length TmCorA without $Mg^{2+}$ in the DCS sites (denoted as FLCorA-no$Mg^{DCS}$), and the full-length TmCorA without $Mg^{2+}$ at all (denoted as FLCorA-no$Mg^{all}$). For the truncated TmCorA-SF model, two simulated systems were carried out including the constrained backbone atoms loop model (denoted as CtrnLoop-Mg) and the non-constrained backbone atoms loop model (denoted as FlexLoop-Mg) to compare degrees of model uncertainty regarding the loop structure prediction. Furthermore, the simulation of $Mg^{2+}$ in aqueous solution (denoted as Free-Mg) was also performed for comparison.

### 3.4.4 Simulation setup

All simulated systems were constructed using the VMD v1.9 program. For the full-length model, the preparation of each system was conducted according to the membrane protein tutorial [84]. MD simulations were performed in POPC membrane where the transmembrane domain of TmCorA was embedded in a central alignment of a hydrated POPC. TIP3P water models [85] were used as water molecules and $Na^+$ and $Cl^-$ ions at a concentration of 0.1 M were used to neutralize the system with using VMD's autoionize plugin. The full-length systems were in the periodic simulation box containing a total of ~300,000 atoms. For CtrnLoop-Mg and FlexLoop-Mg, the simulations were performed in aqueous solution because the periplasmic loop of TmCorA is the exposing part at an extracellular side of the membrane. Each system was solvated by TIP3P water molecules and neutralized by counter ions using the VMD plugin scripts. To mimic the immobility of the missing transmembrane and intracellular parts of the protein, two terminal backbone atoms of both truncated TmCorA-SF simulations were constrained with respect to their initial positions. The CtrnLoop-Mg simulation was carried out by constraining all backbone atoms while no constrained atoms were applied in the FlexLoop-Mg simulation. To validate the consistency of the simulations and improve sampling, both simulations were performed with three replications using independent starting configuration.

All MD simulations were performed using NAMD2.8b2 software. CHARMM22 and CHARMM27 force field parameters were employed for protein and lipid, respectively including for the metal ions (including $Mg^{2+}$, $Ca^{2+}$, $Na^+$ and $K^+$) [49]. The periodic boundary conditions and long-range electrostatic interactions using the particle mesh Ewald summation with a distance cut-off of 12 Å and pair list distance of 13.5 Å were employed [86]. The SHAKE and SETTLE algorithms were used to keep the rigid bond between the hydrogen and heavy atoms [87, 88]. Pressure was kept constant at 1 atm using a Nośe-Hooven Langevin Piston [89, 90]. Temperature was slowly increased from 100 K to 300 K and kept constant at 300 K using Langevin dynamics with the damping coefficient of 1 $ps^{-1}$. The details of all MD systems are shown in Table 3.1 and the studied simulation systems of all-atoms are demonstrated in Figure 3.7. In addition, MD simulations of other cations including $Ca^{2+}$, $K^+$ and $Na^+$

in aqueous denoted as Free-M systems and in flexible loop denoted as FlexLoop-M systems were also conducted individually for comparison.

**Table 3.1** Detailed summary of the studied MD simulations

| system | #$Mg^{2+}$ | #water | #POPC | box dimension(Å$^3$) | total atoms | time (ns) × repetition |
|---|---|---|---|---|---|---|
| FLCorA | 14 | 66763 | 493 | 131 × 124 × 170 | 293648 | 100×1 |
| FLCorA-no $Mg^{all}$ | 0 | 62059 | 493 | 128 × 128 × 169 | 286402 | 100×1 |
| FLCorA-no $Mg^{DCS}$ | 4 | 66743 | 493 | 139 × 140 × 144 | 293598 | 100×1 |
| FlexLoop-Mg | 1 | 9298 | 0 | 78 × 73 × 52 | 29517 | 20×3 |
| CtrnLoop-Mg | 1 | 9298 | 0 | 78 × 73 × 52 | 29517 | 20×3 |
| Free-Mg | 1 | 826 | 0 | 30 × 30 × 30 | 2481 | 10×1 |

### 3.4.5 Molecular dynamics simulations

To relax the initial configuration and remove steric clashes, energy minimizations and restrained MD simulations were performed. Firstly, lipid tails were fixed but other atoms were minimized and equilibrated. Subsequently, protein atoms and $Mg^{2+}$ ions were restrained while the rest (waters, lipids and counter ions) were relaxed. Finally, all atoms in the system were carried out with free molecular dynamics to further equilibrate. The time step of each MD simulation was 2 fs and recording step was 2 ps/trajectory. MD simulations for full-length systems were conducted for 100 ns while the simulation time for the truncated systems was 20 ns and for Free-Mg system was 10 ns.

### 3.4.6 MD trajectory analysis

Structural and dynamical information of the simulated systems was extracted from MD trajectories through the execution of modified VMD scripts. This includes the atomic-based root-mean-square-deviation (RMSD), the residue-based root-mean-square-fluctuation (RMSF), radial distribution function (RDF), probability distribution of coordination number, hydrogen-bonding, inter-atomic distances and its distribution, principal component analysis (PCA) and the mean residence time (MRT).

The HOLE program [91] was employed to compute the pore radius of the protein models.

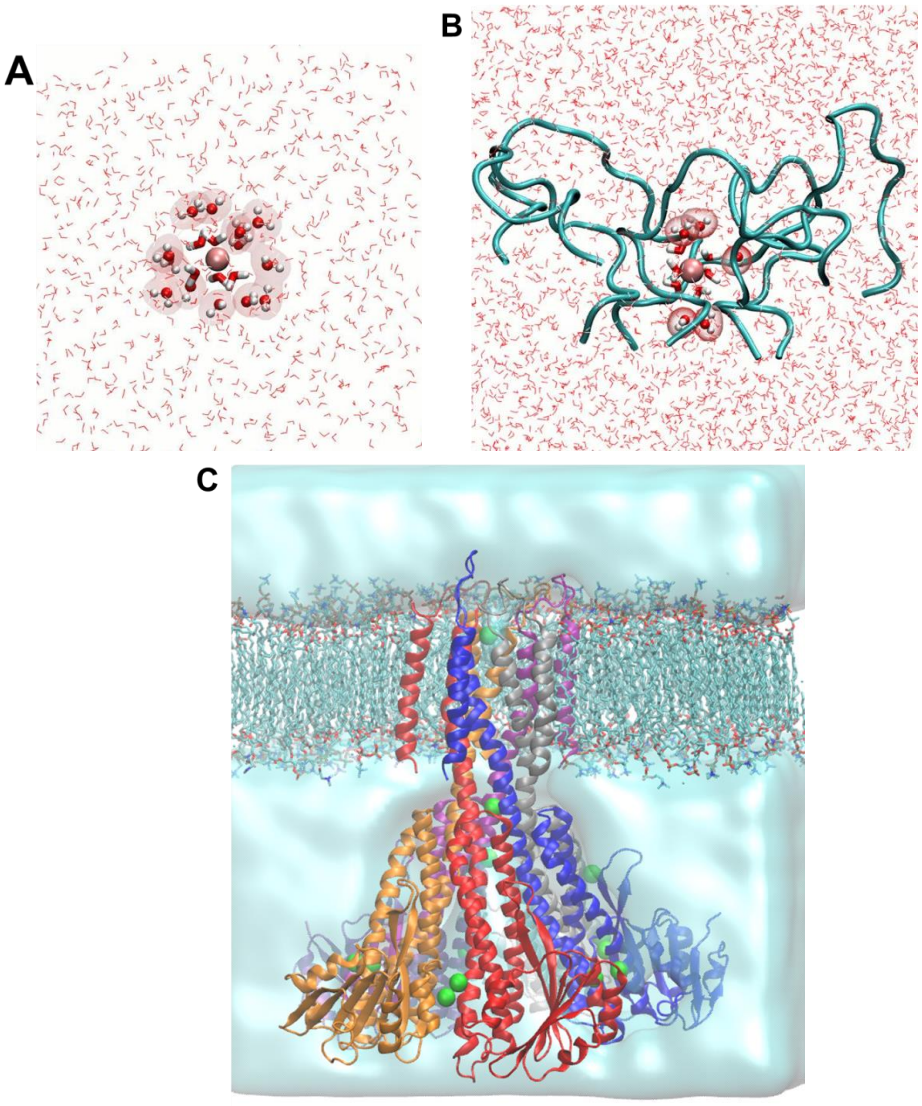


**Figure 3.7** (A) Free-Mg (B) FlexLoop-Mg / CtrnLoop-Mg in the water box simulation (C) FLCorA showing the $Mg^{2+}$ ions locating in the systems.

### 3.4.7 Domain motion by principle component analysis (PCA)

To identify essential dynamics of motions of the FLCorA systems, a principal component analysis for Cα atoms was analyzed by aligning the structure

coordinates of average trajectories (about 1500-2000 structural snapshots at 20 ps intervals were chosen from the last 40-ns MD trajectories) on its initial structure then filtering out all occurring trivial translations and rotations. The first two principal components (PC1 and PC2) of motion, which correspond to the first two Eigen vectors of the covariance matrix, were determined using the WORDOM structural analysis package, interpolated structures along the first two principal components were created using VMD.

### 3.4.8 Mean residence time (MRT) of water in coordination shell

A mean residence time (MRT) is an exchanging rate between water molecules in the second solvation shell of $Mg^{2+}$ and those in the bulk solution. Here, MRT value was calculated by using the time correlation function (C(t)), according to an equation (3.1) [92].

$$C(t) = \frac{\langle T(0)T(t)\rangle}{\langle T\rangle} \quad \textbf{(3.1)}$$

where T(t) is a binary function at time t. T(t) will be equal to 1 if the considered water molecule remains in the site at time t, and 0 otherwise. T(0) is equal to 1 at time zero, T is a period of determining time. Therefore, C(t) is the conditional probability of a tagged-water pair at time t thus C(t) will be reached ~0 (at a long-time) according to an exponential decay. The time period was divided into every 30 ps along a total of simulation time (20-ns for Loop-Mg systems and 100-ns for FLCorA systems). The MRT of water ($\tau$) in the hydration shell can be calculated by fitting the exponential function according to equation (3.2) [93]. The residence time correlation function graph of a representative curve of each system is displayed in Figure 3.8.

$$C(t) = e^{-t/\tau} \quad \textbf{(3.2)}$$

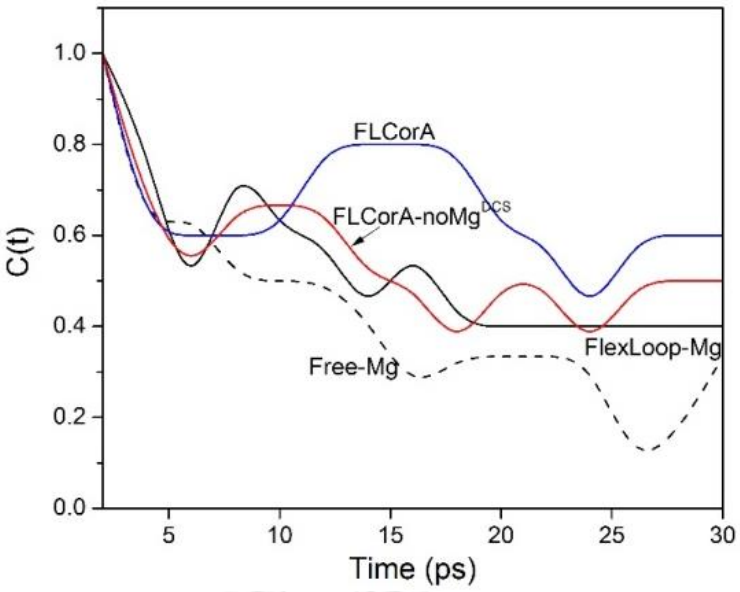


**Figure 3.8** The residence time correlation function curve comparing among the studied systems.

### 3.4.9 QM/MM study

To investigate the interactions between $Mg^{2+}$ and water molecules in the TmCorA-SF, a snapshot in the minimization step of FLCorA was selected. It is essential to reduce the size of the model system since the structure of the full-length TmCorA is too large for QM/MM calculations. The studied model includes the atomic coordinates of the TmCorA-SF (G312-M313-N314), $Mg^{2+}$, and a total of ten water molecules with the distance of 5.5 Å from $Mg^{2+}$ (Figure 3.9). Gaussview05 program was used to add the N-terminal with $–COCH_3$ and C-terminal with $–NHCH_3$ to the model to prevent the terminal-charge effect. Structure optimization was performed using the hybrid computational method of Our own N-layered Integrated molecular Orbital and molecular Mechanics (ONIOM) developed by Mokomura [94] incorporated in the Gaussian09 program package [80] (possessed a total of 281 atoms) with three-layered ONIOM calculation of B3LYP/6-31G(d):PM6:UFF level [95-97] as for a high, medium and low layer, respectively. The inner part of the structure consisting of $Mg^{2+}$ and ten water molecules was treated as the QM part. The side chain atoms of N314 and backbone atoms along G312 to N314 were chosen as the medium layer and the rest were treated as the low layer. For describing the studied model systems, we used a notation $[ML_xW_ySF]^{n+}$ where M is the studied metal ion with an n-charge including

$Li^+$, $Na^+$, $K^+$, $Ca^{2+}$, $Mg^{2+}$, $Co^{2+}$, $Ni^{2+}$, $Al^{3+}$, and $Co^{3+}$; L is water molecule for $Li^+$, $Na^+$, $K^+$, $Ca^{2+}$, $Mg^{2+}$, $Co^{2+}$, $Ni^{2+}$, $Al^{3+}$ and is ammonia molecule for $Co^{3+}$ and $Ni^{2+}$ as $Co^{3+}$-hexaammine ($Co^{3+}$-hex or Cohex) and $Ni^{2+}$-hexaammine ($Ni^{2+}$-hex or Nihex) thus there are 10 studied models; W is water molecule; x and y are, respectively, the coordination numbers of the inner-shell ligand ($H_2O$ or $NH_3$) and the outer-shell water; SF is referred to the capped GMN residues of five protomers. Here, Cohex and Nihex were investigated because, based on the literature [78], Cohex is the potent CorA inhibitor but Nihex is not. The details of the model systems and the ONIOM setup parameters are summarized in Table 3.2.

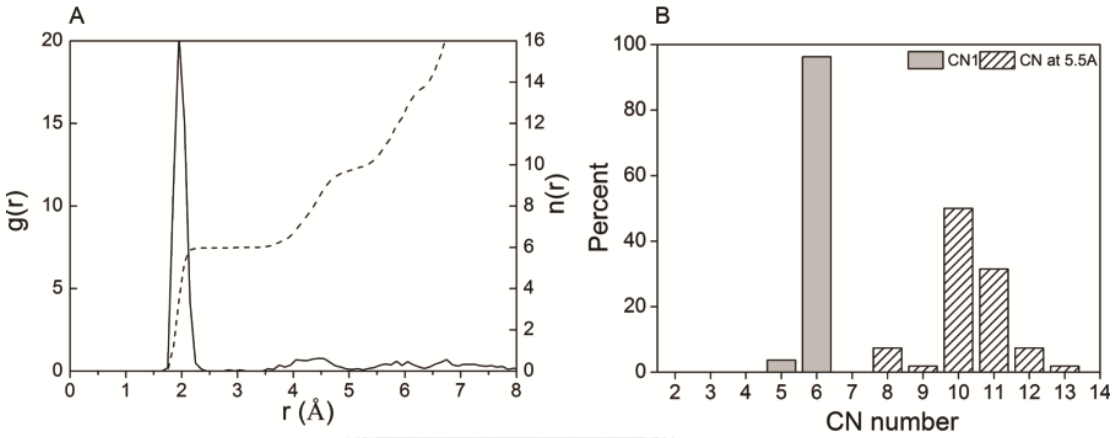


**Figure 3.9** (A) RDF of Mg-O($H_2O$) from MD trajectories of FLCorA minimization step (B) Coordination number distribution of the first hydration shell (CN1) and CN of water molecules at the Mg-O distance of 5.5 Å.

**Table 3.2** ONIOM details for geometry optimizations. Where M is $Li^+$, $Na^+$, $K^+$, $Ca^{2+}$, $Mg^{2+}$, $Co^{2+}$, $Ni^{2+}$, $Al^{3+}$ , $Co^{3+}$ and n+ is the ion's charge.

| system | QM basis set[a] | medium basis set[a] | low model forcefield[a] | total atoms |
|---|---|---|---|---|
| $[M(H_2O)_x\,(H_2O)_y\,SF]^{n+}$ | B3LYP/6-31G(d) (31) | PM6 (115) | UFF (135) | 281 |
| $[Co(NH_3)_6(H_2O)_4SF]^{3+}$ | B3LYP/6-31G(d) (37) | PM6 (115) | UFF (135) | 287 |
| $[Ni(NH_3)_6(H_2O)_4SF]^{2+}$ | B3LYP/6-31G(d) (37) | PM6 (115) | UFF (135) | 287 |

[a]Numbers in parentheses are the values of atoms in each ONIOM layer.

The examples of ONIOM complex models of the hydrated- $Mg^{2+}$-SF is shown in Figure 3.10. The complexation energy denoted as $\Delta E([ML_x]^{n+})$, the total complexation energy denoted as $\Delta E([ML_xW_y]^{n+})$ and the stabilization energy from the selectivity filter denoted as $\Delta E_{sSF}$ were calculated according to equations (3.3), (3.4), and (3.5), respectively.

$$\Delta E([ML_x]^{n+}) = E([ML_x]^{n+}) - (E(M^{n+}) + xE(L)) \quad \textbf{(3.3)}$$

$$\Delta E([ML_xW_y]^{n+}) = E([ML_xW_y]^{n+}) - (E(M^{n+}) + xE(L) + yE(W)) \quad \textbf{(3.4)}$$

$$\Delta E_{sSF} = E([ML_xW_ySF]^{n+}) - (E([ML_xW_y]^{n+}) + E(SF)) \quad \textbf{(3.5)}$$

where $E([ML_x]^{n+})$ and $E([ML_xW_y]^{n+})$ are the single point energies of the $[ML_x]^{n+}$ and $[ML_xW_y]^{n+}$ complexes, respectively. E(M) is the single point energy of the metal ion, E(L) is the single point energy of the inner-shell ligand molecule ($H_2O$ or $NH_3$) and E(W) is the single point energy of the outer-shell water molecule. These energies were calculated at B3LYP/6-311+G(2d,2p) level from the optimized structures. $E([ML_xW_ySF]^{n+})$ is the single point energy of $[ML_xW_ySF]^{n+}$ calculated with 2-layered ONIOM using B3LYP/6-311+G(2d,2p):B3LYP/6-31G(d) level where the SF molecule was treated as the low layer and E(SF) is the single point energy of the SF molecule calculated with B3LYP/6-31G(d) level.

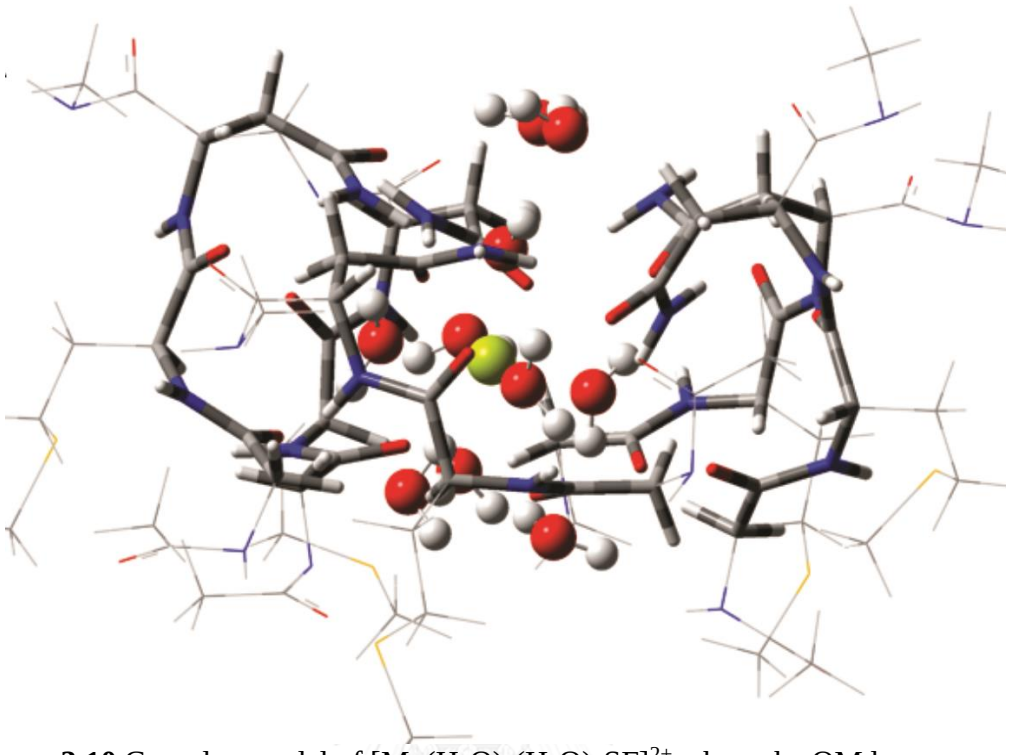

**Figure 3.10** Complex model of $[Mg(H_2O)_6(H_2O)_4SF]^{2+}$ where the QM layer comprises of $Mg^{2+}$ and $+10H_2O$ ($M+6NH_3+4H_2O$ for cation hexaamine) as shown in ball-and-stick model, the medium layer is shown in licorice model and the low layer is shown in wireframe model.

จุฬาลงกรณ์มหาวิทยาลัย
Chulalongkorn University

## 3.5 Results and discussion

### 3.5.1 First and second hydration shells of $Mg^{2+}$

An obtaining RDF profile (g(r)) of Mg-O(water) comparing among Free-Mg, CrnLoop-Mg, and FlexLoop-Mg is shown in Figure 3.11(A). The RDF of Free-Mg profile provides two-separated peaks of the first and second hydration shells. The first hydration shell appears as a sharp peak at 2.0 Å while the second shell appears as a broad peak at 3.5 – 4.8 Å with the maximum distance of 4.2 Å. Because of being strong ion-solvent interactions, the first hydration shell is well separated from the second one. No exchange of water molecule between the first and second shells was observed during the simulation time. The experimentally-determined residence times of the inner-shell water were found to be on the order of microsecond time scale at 25

°C [98]. Whereas the RDF between the second and bulk was considerably separated, but is not reached a zero value (at minimum), suggesting that there are the probability of an exchange process between the second shell and bulk waters. The integration of the first peak is equal to six revealing an octahedral arrangement of the first hydrated-shell of $Mg^{2+}$. Figure 3.11(B) illustrates the probability distributions of coordination numbers within the first and second hydration shells calculated from the RDF graph. The rigidity of the first hydrated-shell structure of $Mg^{2+}$ can be illustrated by a 100 percentage frequency of occurrence. Furthermore, the integration number, n(r) of the second shell waters is up to ~17. The hydration number of the second shell was distributed with a various numbers because of the water exchange process between the second shell waters and bulk waters during the simulation. This indicates that the interactions between $Mg^{2+}$ and the second-shell waters are relatively weak.

The results clearly show that the first-shell coordination is absolutely equal to 6, while the second-shell coordination is distributed from 8 to 17 with the most frequency of 13 (followed by 12, 14 and 11 with slightly lower probability). Both Loop-simulations provide the similar two-separated peaks with the RDF of Free-Mg. However, an important difference is the lower intensity peak at the second-shell coordination in the RDF of both Loop-Mg systems. The most second shell water-coordination number (CN2) is 5 and 3 for FlexLoop-Mg and CtrnLoop-Mg, respectively. Noticeably, the second-shell waters of $Mg^{2+}$ in the TmCorA-SF are considerably less than in the bulk. Besides, the MRT value (Table 3.3) of the second shell waters in both Loop-Mg simulations (29.4 ps) is greater than that of in Free-Mg (10.2 ps). This longer residence time indicates that the second-shell waters of $Mg^{2+}$ in the Loop system become stable and hardly exchangeable. Overall, the results from this simulation are in good agreement with x-ray diffraction and QM/MM MD studies [99-101]. The computational studies suggested that, in aqueous solution, the fully hydration structure of $Mg^{2+}$ ($Mg[H_2O]_6 \cdot [H_2O]_{12}^{2+}$) is arranged approximately as a dodecahedral cluster [102].

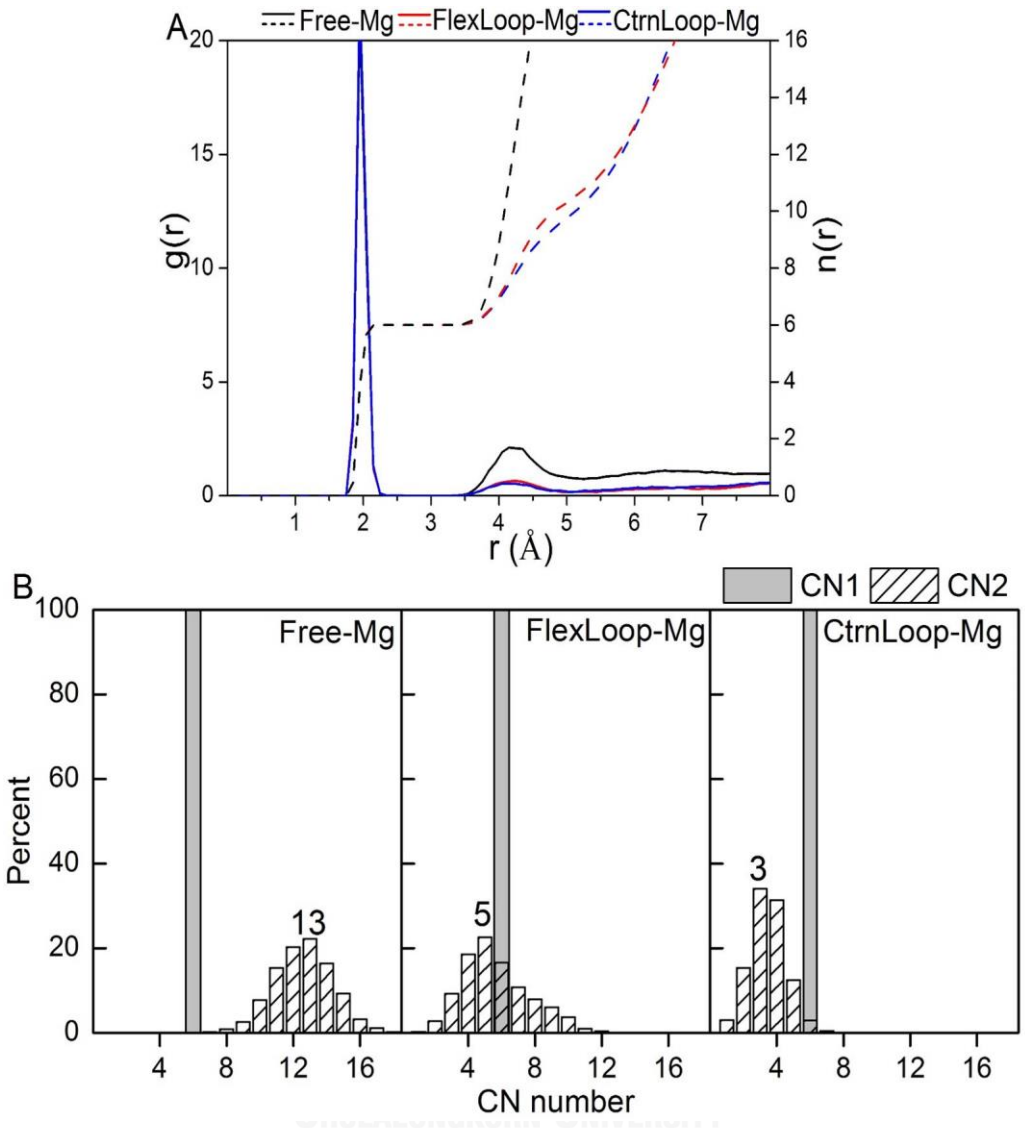


**Figure 3.11** (A) g(r) of the Mg-O(water) distance of Free-$Mg^{2+}$ (black), FlexLoop-Mg (red) and CtrnLoop-Mg(blue) and (B) the corresponding probability distribution of CN1 and CN2.

The loss of some second-shell waters of the hydrated $Mg^{2+}$ may be resulted from the repulsions between the GMN residues and the fully-hydrated $Mg^{2+}$ due to the quite narrow metal-binding pocket as well as hydrogen bonding between the first and second-shell waters is relatively weak, thus, the acceptor atoms of G312 and N314 (oxygen or nitrogen) can be the outer shells as substituted from water molecules via hydrogen bond formations. To verify the second-shell replacement, the RDF of Mg-

O(G312) and Mg-$O^{\delta}$(N314) was analyzed as shown in Figure 3.12(A) for CtrnLoop-Mg and FlexLoop-Mg. It clearly shows a single peak with maximum about 4.2-4.3Å from the $Mg^{2+}$-center which is essentially the same as the second-shell distance present in Free-Mg. Therefore the G312 and N314 could serve as the second-shell ligands when the $Mg^{2+}$ is bound to the TmCorA-SF. The coordination number can be obtained from the integration value (n(r)) of the RDF as equal to 4 - 5 for G312 and N314 (for both Loop-Mg simulations) which is corresponding to the pentameric structure of the GMN sequences. From trajectory visualization, the orientation of O(G312) and $O^{\delta}$(N314) atoms poses toward $Mg^{2+}$ in which they can form hydrogen bonding with the first-shell waters (Figure 3.12(B)). The hydrogen-bonding between the first-shell and second-shell ligands of $Mg^{2+}$ were explored according to the criteria of the distance between H-donor (N or O) and H-acceptor (usually O) less than 3.0 Å and the angle of hydrogen-donor-acceptor not greater than 65°.

**Table 3.3** Hydration number with the most occurrence and residence time of water molecules in the first and second shells of ions at 300K[a].

| system | hydration number | MRT (ps) |
|---|---|---|
| Free-Mg | 6 (13) | ne[b] (10.2) |
| FlexLoop-Mg | 6 (5) | ne (29.4) |
| CtrnLoop-Mg | 6 (3) | ne (29.4) |
| FLCorA | 6 (8) | ne (47.1) |
| FLCorA-no$Mg^{DCS}$ | 6 (10) | ne (35.2) |

[a]Numbers in parentheses are for the second hydration shell in the hydration number column and for the first and second shells in the residence time column. [b]ne=No exchange of water during the simulation time.

The hydrogen-bonding occupancy between the first-shell waters and second-shell ligands (water molecules, G312, and N314) extracted from MD trajectories is shown in Figure 3.13. It is obviously shown that the hydrogen-bonding between the first-shell waters and O(G312) and $O^{\delta}$(N314) atoms can compensate the

hydrogen-bonding loss between water molecules in the first and second shells. It should also be noted that the hydrogen-bonding for the pairs of the first-shell waters and G312 or N314 observed from CtrnLoop-Mg provides a higher occupancy than from FlexLoop-Mg as a result of backbone rigidity performing on CtrnLoop-Mg simulations.

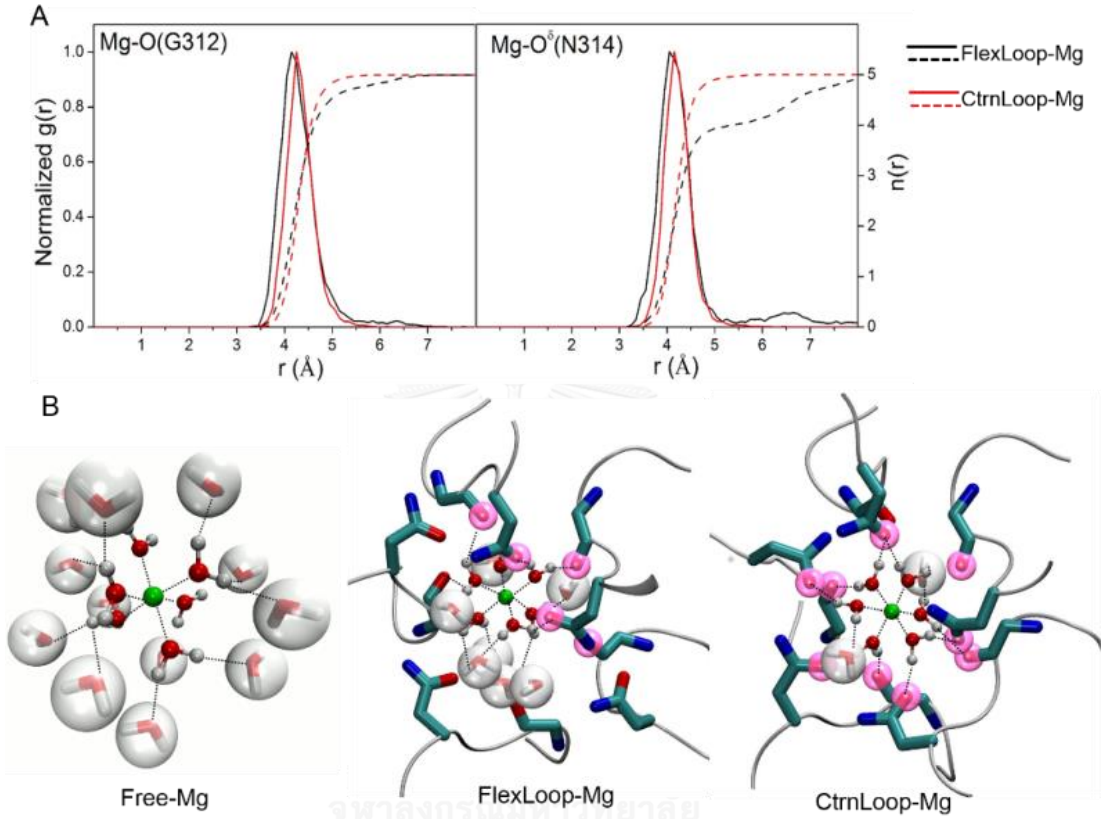


**Figure 3.12** (A) g(r) of the Mg-O of G312 and of N314 and (B) Inner and outer shells of the coordination structure taken from MD snapshots shown together with hydrogen bonds (dashed line). $Mg^{2+}$ is colored as the green sphere. The first-shell waters are drawn as a ball and stick representation, and the second-shell waters are shown as a stick in a white sphere. G312 and N314 side chains are drawn as a stick presentation. Residues located within the second shell are indicated by a pink sphere.

In the case of ions in aqueous solution (Free-M systems), the RDF profiles (Figure 3.14) display the substantial differences of the first and second peaks of g(r) of the M-O(water) supporting they have the different hydration shell structures. In addition, for FlexLoop-M systems, the MD results revealed that there was only $Mg^{2+}$ locating in the selectivity filter as it possessed the minimal displacement along the Z-

axis of the channel (Figure 3.15), on the contrary, other three cations moved out immediately. This suggests that G312 and N314 residues can specifically recognize the orientation of the hydrated $Mg^{2+}$ rather than other biological cations.

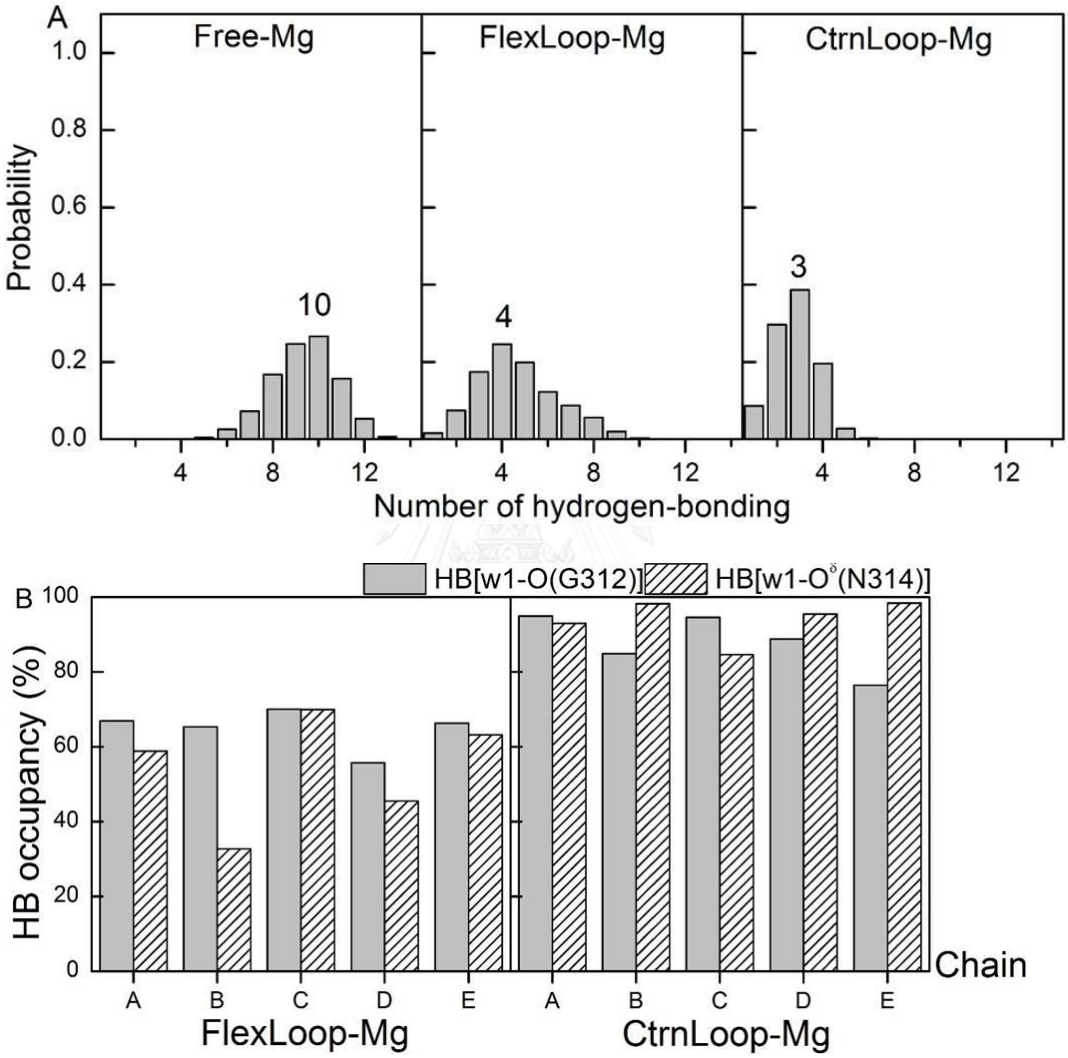


**Figure 3.13** (A) Probability distribution of the number for hydrogen bonding between the first-shell water (w1) and the second-shell waters (w2) and (B) Occupancy of hydrogen bond for the pairs of w1-G312 and w1-N314.

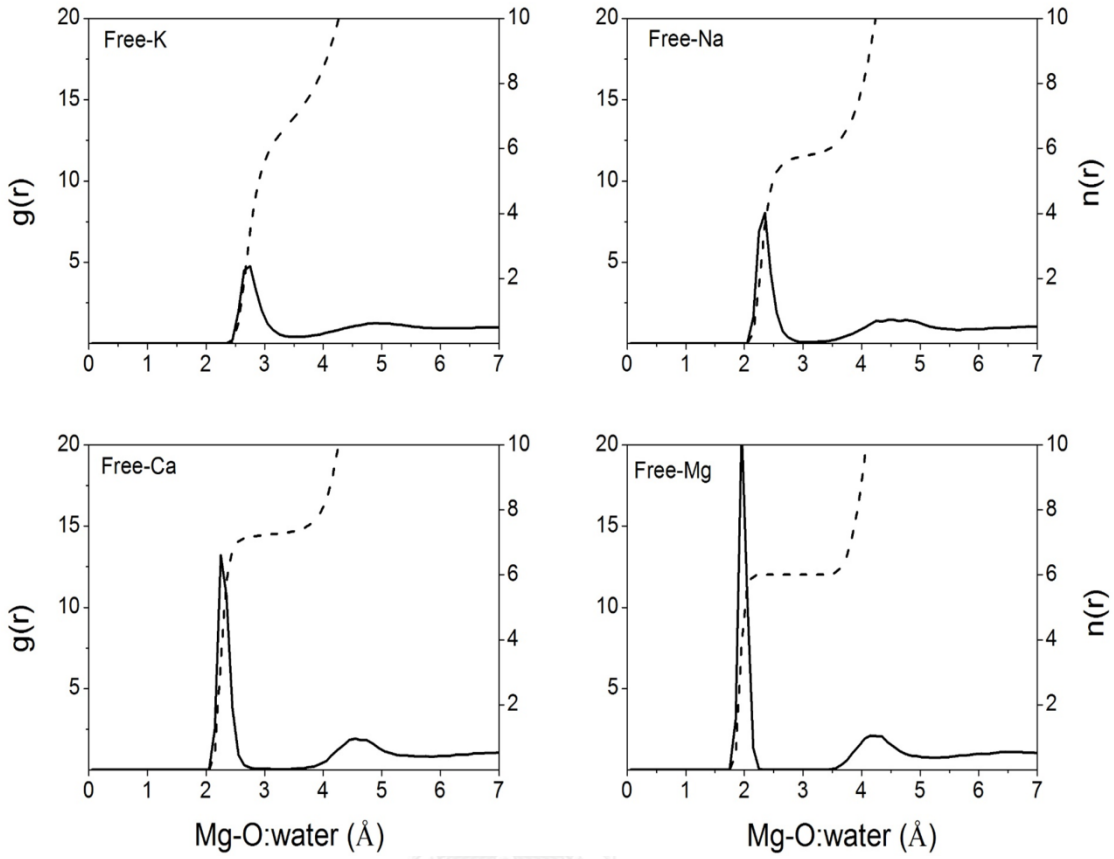


**Figure 3.14** g(r) of the Mg-O(water) distance of Free-M systems (where M = $K^+$, $Na^+$, $Ca^{2+}$ and $Mg^{2+}$ denoted as Free-K, Free-Na, Free-Ca and Free-Mg, respectively).

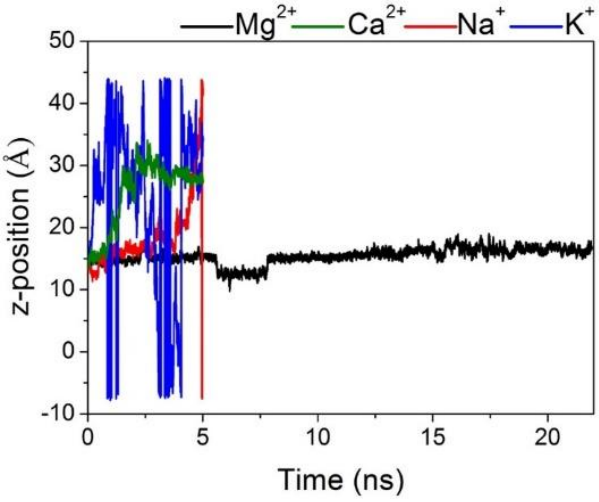


**Figure 3.15** the Z-position of each metal ion in the FlexLoop-M system along the simulation time (where M = $K^+$ , $Na^+$, $Ca^{2+}$ and $Mg^{2+}$).

### 3.5.2 Simulations of the full-length protein

The backbone RMSDs of FLCorA, FLCorA-noMg$^{all}$ and FLCorA-noMg$^{DCS}$ were analyzed as shown in Figure 3.16. The low RMSD value during the first ~6 ns was resulted from the restrained simulations in the minimization step, after that, RMSD rapidly increase in the MD production run due to all restraints were removed. During the course of MD simulations, all three systems showed a gradual increase in RMSD, except for FLCorA-noMg$^{all}$, which exhibits a rapid change in the first 40ns. However, they reach a steady state after 50ns and remain stable until the end of the simulation (100ns) for all simulated systems. A small RMSD fluctuation between 3 and 4 Å suggests the overall stability of the protein structure and a well-behaved system of the simulations.

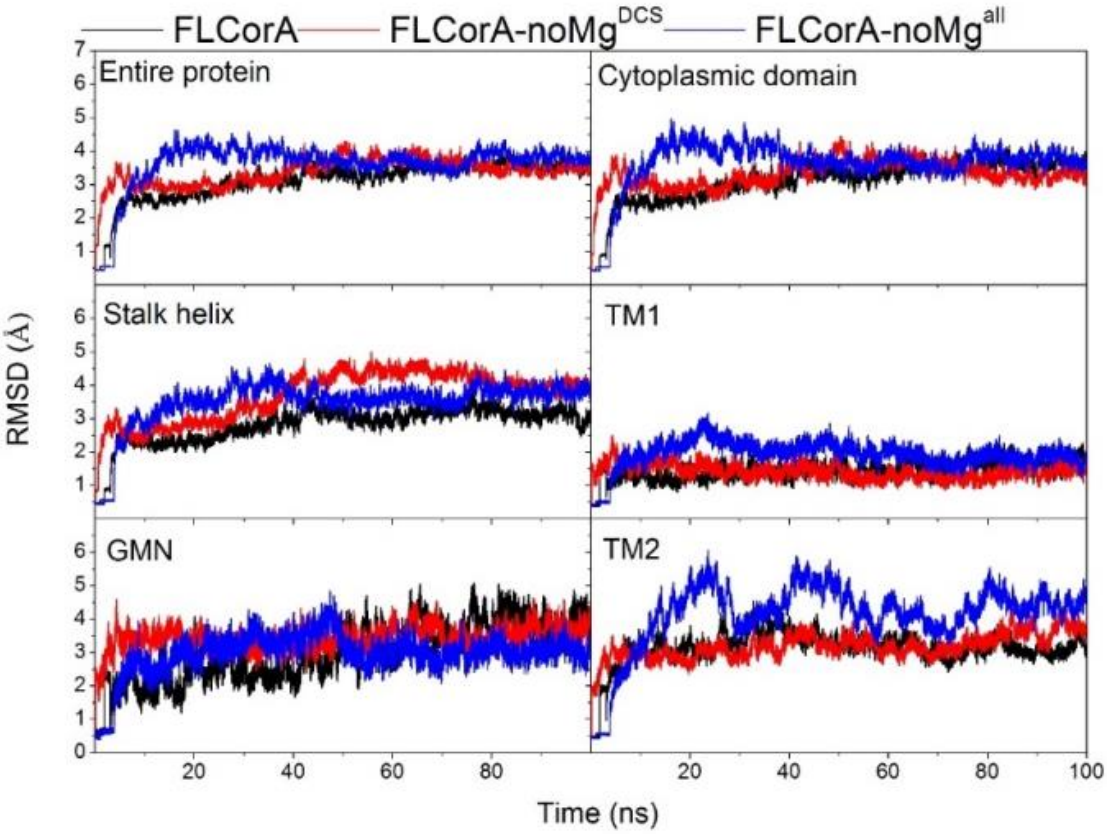


**Figure 3.16** Backbone RMSD profiles with respect to the starting structure over the 100ns MD trajectories of FLCorA, FLCorA-noMg$^{DCS}$ and FLCorA-noMg$^{all}$.

The structural and dynamical fluctuation of five domains of the protein including cytoplasmic domains (residues 30-239), stalk (residues 240-290), inner transmembrane helices (or TM1 residues 291-310), the GMN sequence (residue 312-314) and outer transmembrane helices (or TM2 residues 327-349) was also determined. From RMSDs of each domain (Figure 3.16), during the first 40 ns, the FLCorA-noMg$^{all}$ simulation's shows a rapid increase in RMSD of cytoplasmic domain greater than FLCorA and FLCorA-noMg$^{DCS}$ simulations. However, after 40 ns of simulations, this cytoplasmic-RMSD of FLCorA-noMg$^{all}$ gradually drops to a comparable value with the other two simulated systems and reached a similar degree of structural deviations at the last 100 ns simulation time. For the TM domain, it appears that TM1 has the smallest deviation for all simulated systems. A distinct effect of the removal DCS-$Mg^{2+}$ can be observed from the higher RMSD values of the stalk in FLCorA-noMg$^{all}$ and FLCorA-noMg$^{DCS}$ simulations compared to that of FLCorA. During the first 40 ns of simulations, the RMSD of the stalk helix domain of FLCorA-noMg$^{all}$ rises to 4 Å, showing the highest degree of fluctuation compared to the other two systems. Nevertheless, the stalk-RMSD of FLCorA-noMg$^{all}$ drops for the next 40ns and rises back to about 4 Å again during the last 20 ns. In contrast, the stalk-RMSD of FLCorA-noMg$^{DCS}$ rises gradually to the average value of ~4 Å during the last 20 ns. It should be noted that both FLCorA-noMg$^{all}$ and FLCorA-noMg$^{DCS}$ simulations revealed the structural fluctuation of stalk helix more than that of FLCorA over the 100 ns of simulation. This implies that the absence of $Mg^{2+}$ in DCS of TmCorA triggers the motion of the stalk domain. Considering the RMSD of TM2, the FLCorA-noMg$^{all}$ simulation exhibits large fluctuations more than other systems. This is probably due to the fact that TM2 is a part connecting to a periplasmic loop, which appears to be highly flexible. However, all simulations did not show an apparent relationship between the TM2-fluctuation and the influence on coordination structures of $Mg^{2+}$ in the TmCorA-SF.

### 3.5.3 Coordination structure of $Mg^{2+}$ in the selectivity filter in full-length TmCorA

The RDFs of Mg-O(water) from FLCorA and FLCorA-no$Mg^{DCS}$ simulations (Figure 3.17(A)) reveal a similar pattern with the RDFs of Mg-O(water) in Free-Mg, CtrnLoop-Mg and FlexLoop-Mg systems. The n(r) of the first peak is equal to six as being an octahedral-inner shell of $Mg^{2+}$. The highest frequency of the second-shell water is 8 for FLCorA and 10 for FLCorA-no$Mg^{DCS}$ (Fgiure 3.17(B)). In the FLCorA-no$Mg^{DCS}$ simulation, the greater number of the second-shell water molecules is associated with side chain rearrangements of the GMN residues as visualized from MD trajectories (Figure 3.19(B)). The MRT of the second-shell water is 47.1ps for FLCorA, which is longer than that of 35.2ps for FLCorA-no$Mg^{DCS}$ (Table 3.3). This indicates that the second-shell waters in the TmCorA-SF of FLCorA-no$Mg^{DCS}$ are more mobile than the waters of FLCorA. The RDFs plots of Mg-O(G312) and Mg-$O^{\delta}$(N314) of FLCorA and FLCorA-noMgDCS are shown in Figure 3.19. The RDFs of both Mg-O(G312) and Mg-$O^{\delta}$(N314) provide only one broad peak with a maximum distance of ~4.2Å from $Mg^{2+}$-center. This supports that all five G312 residues do not directly bind to $Mg^{2+}$ but they interact with the hexahydrated $Mg^{2+}$ through the hydrogen bonding. The n(r) value is 4 for the RDF of Mg-O(G312) for the FLCorA simulation and only 2 for FLCorA-no$Mg^{DCS}$ system. A considerable decrease of the interactions to the inner-shell waters suggests the TmCorA-SF loosely binds to the $Mg^{2+}$. The hydrogen-bond occupancy extracted from the last 20 ns MD trajectories of the two full-length CorA systems is shown in Figure 3.18. It clearly displays that the missing of DCS-$Mg^{2+}$ affects the hydrogen bonding formation in between the inner-shell water of $Mg^{2+}$ and the selectivity residues. Moreover, the Mg-$O^{\delta}$(N314) RDFs obviously display that, for the FLCorA-no$Mg^{DCS}$ system, a featureless RDF peak with the maximum roughly 4.8 Å (Figure 3.19(A)) was observed which was farther than that observed in the FLCorA system. By visual inspection, hydrogen bonding between $O^{\delta}$(N314) of FLCorA and the inner-shell water is apparent whereas all 5-$O^{\delta}$(N314) of FLCorA-no$Mg^{DCS}$ point away from the filter-center (Figure 3.19(B)). Therefore, the missing of DCS-$Mg^{2+}$ seriously affects the structural rearrangement of the GMN motif, causing a decrease in the interactions between the selectivity filter residues and the hexahydrated $Mg^{2+}$.

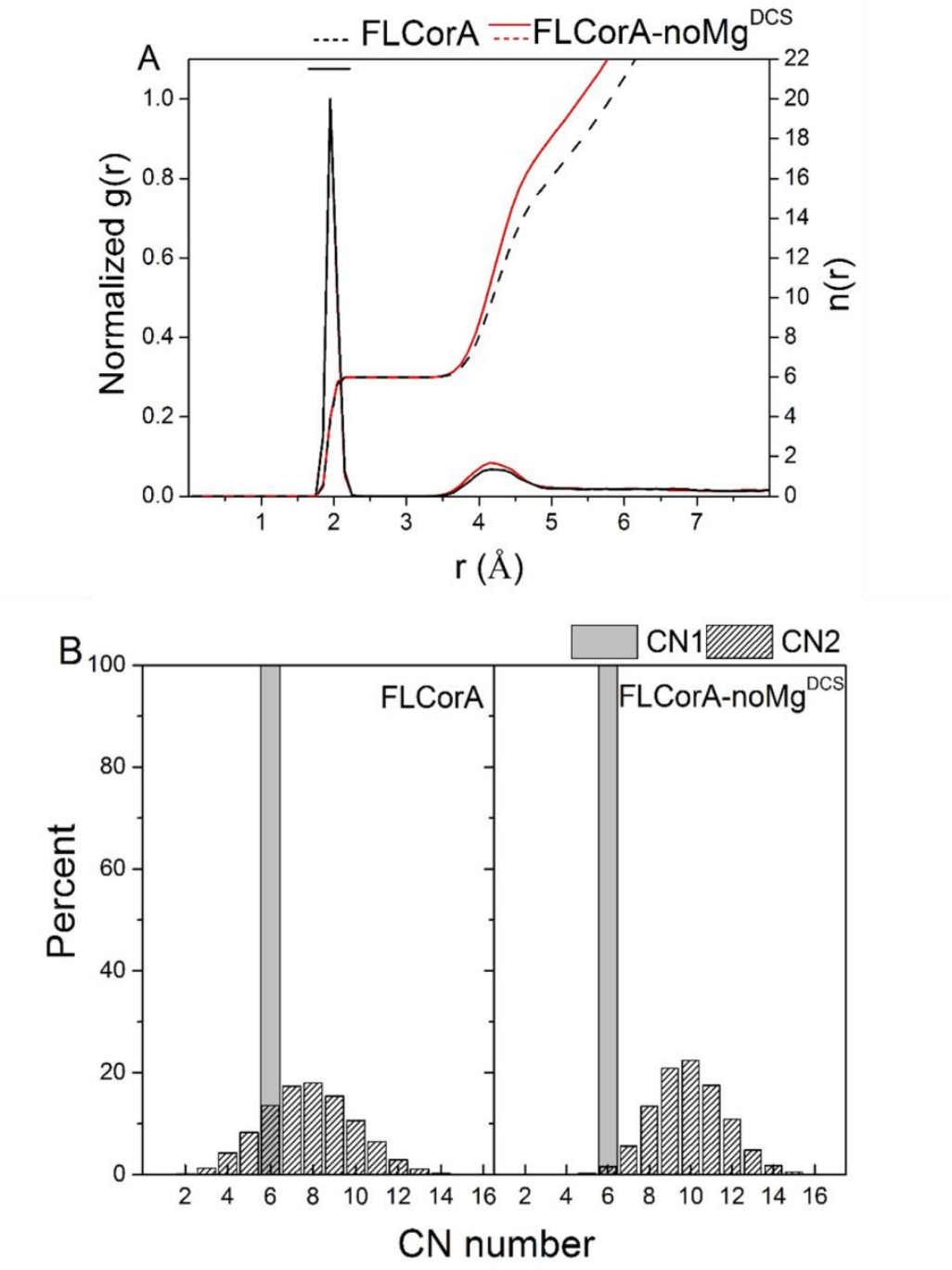


**Figure 3.17** (A) g(r) and n(r) of the Mg-O(water) distance (B) Coordination number distribution of CN1 and CN2 of FLCorA and FLCorA-noMg$^{DCS}$.

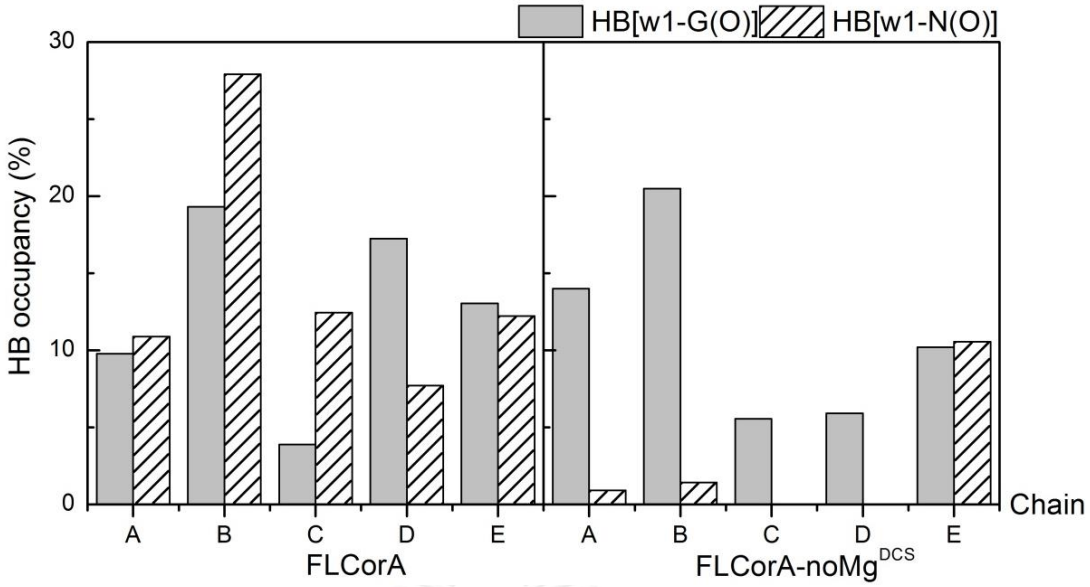


**Figure 3.18** hydrogen-bond occupancy for the pairs of w1-G312 and w1-N314 of FLCorA and FLCorA-noMgDCS systems.

Furthermore, the Mg-$O^{\delta}$(N314) distance distribution plots and RDF provide a less well-defined shape compared to the Mg-O(G312)'s. This can be implied that the G312 residues contribute to greater stability of the hydrated $Mg^{2+}$-GMN complex than the N314 residues as well as the missing of DCS-$Mg^{2+}$ could drive the pore opening which is observed from the $Mg^{2+}$ position along Z-axis (Figure 3.20(A)) showing that, at the simulation time of ~50ns, the hexahydrated $Mg^{2+}$ ion tends to move towards the permeation pore. The Z-position distribution plot shows a majority of events that, for FLCorA-no$Mg^{DCS}$, the $Mg^{2+}$ positions are closer to the pore entry of the channel than that of the FLCorA simulation. The results again confirm that the G312 and N314 are responsible for the stability of the hexahydrated $Mg^{2+}$ in the selectivity filter. Moreover, **Error! Reference source not found.**(B) depicts a wider diameter of the GMN scaffold in FLCorA-no$Mg^{DCS}$ than that of FLCorA. Nonetheless, the moving of $Mg^{2+}$ across the membrane was not observed because the channel pore remains unchanged. As expected, the study's simulations also show a significant structure perturbation of the cytoplasmic domain and the stalk helices upon removal of $Mg^{2+}$ from the DCS sites. Owing to the surrounding of negatively charged residues at the

DCS sites between the two adjacent subunits, the absence of DCS-$Mg^{2+}$ possibly leads to electrostatic repulsions among these residues resulting in the channel-unlocking as in a conductive state. However, during the course of the simulations, the channel pore did not open wide enough to permit translocation of a hydrated $Mg^{2+}$ ion.

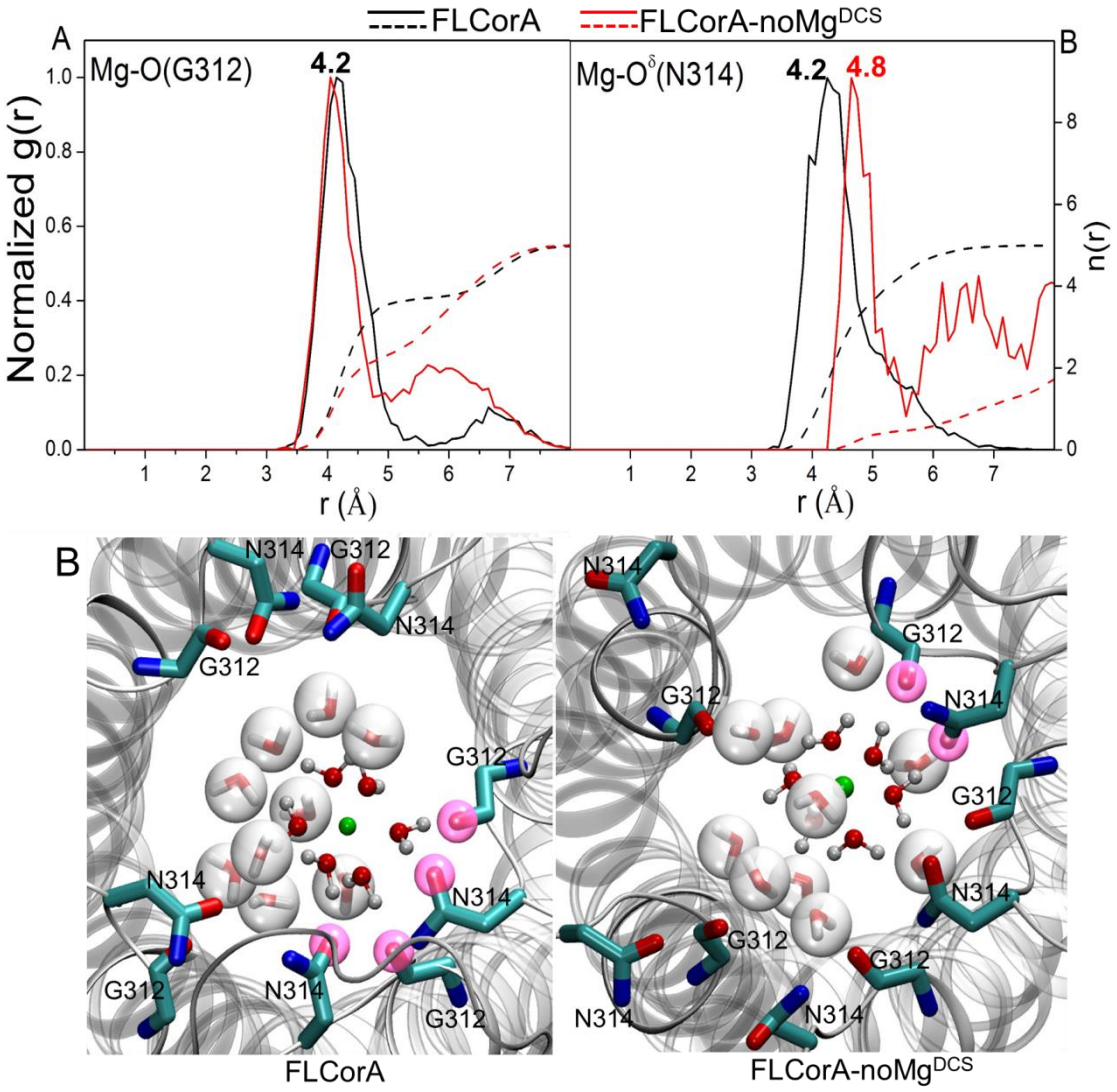


**Figure 3.19** (A) g(r) of the Mg-O of G312 and of N314 for FLCorA and FLCorA-noMg$^{DCS}$ systems. (B) Inner and outer shells of the coordination structure taken from MD snapshots. The model representation and color scheme used in this figure are the same as that used in Figure 3.12.

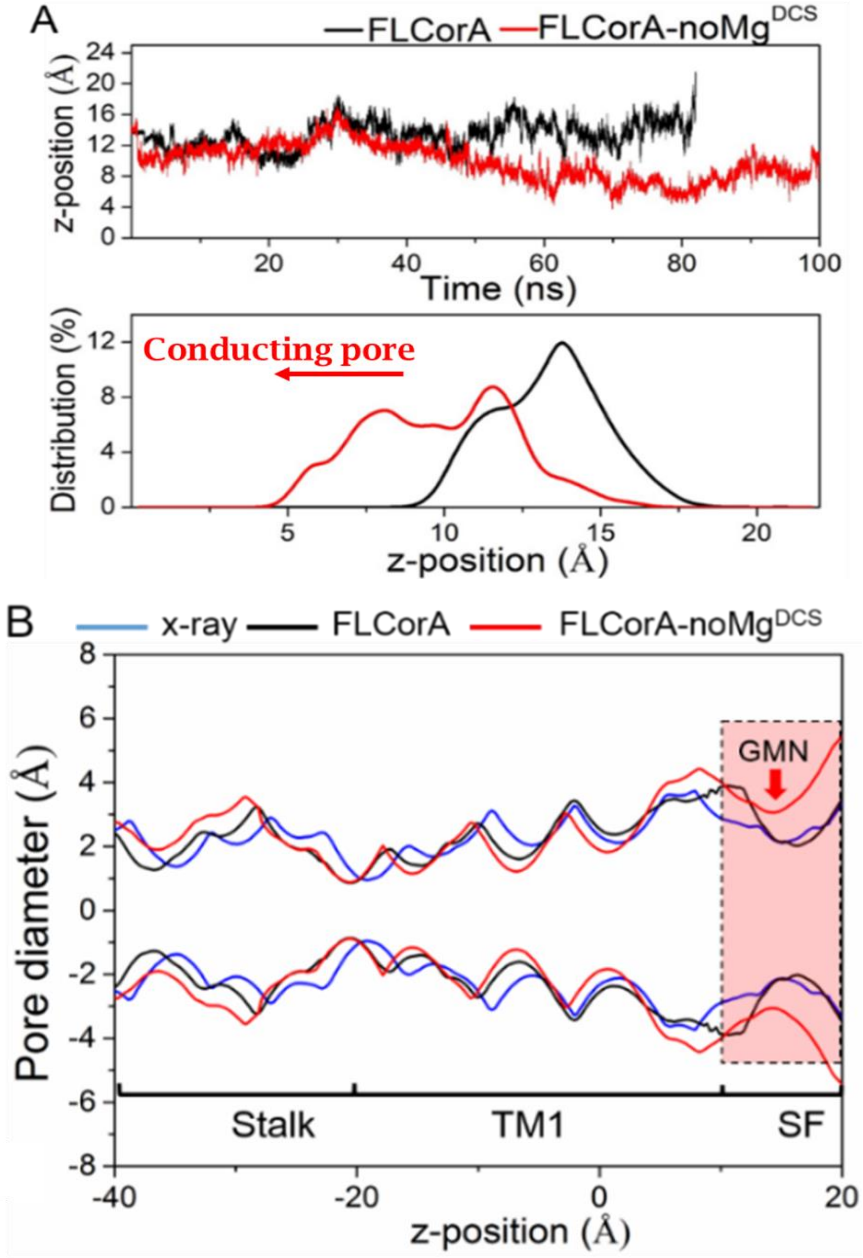


**Figure 3.20** (A) fluctuation and distribution of the corresponding z-position of $Mg^{2+}$ in the selectivity filter (SF) and (B) a pore diameter plot of the MD snapshot.

### 3.5.4 Domain motion by principal component analysis

To identify the essential dynamic conformational change associated with the presence or absence of $Mg^{2+}$ in DCS sites, post-processing MD including per-residue RMSF and essential dynamics analysis were performed between 60 and 100ns of MD trajectories of the full-length protein systems.

Figure 3.21 shows the residue-based Cα RMSFs of the FLCorA, FLCorA-noMg$^{DCS}$ and FLCorA-noMg$^{all}$ over the last 40ns of the simulation time. It is evident that the cytoplasmic (residues 150-195) and stalk helices (residues 245-290) in the FLCorA-noMg$^{DCS}$ trajectory reveals higher fluctuating part in comparison with those in the other two full-length trajectories. In addition, the inset plots show the largest fluctuation of the DCS-binding residues including E88, D89, D175 and D253 in the FLCorA-noMg$^{DCS}$ trajectory. This can be implied that the helix bundle is tended to be unlocked triggering the stalk helix moving toward the open conformation, when the DCS site has no $Mg^{2+}$.

In most cases, the first few eigenvectors or principal components are sufficient to capture the dominant modes of large-scale motions. As shown in Figure 3.22(A,B), the interpolated structures along the first principal component (PC1) were generated to explore the comparative motion between the FLCorA and FLCorA-noMg$^{DCS}$ trajectories. The PC1 of both trajectories clearly show that the cytoplasmic domain and extracellular loop appear to be the first dominant motion, which corresponds to rocking and twisting movement. As a comparison, PC1 can capture a different collective motion in the stalk region, where the motion observed in the FLCorA-noMg$^{DCS}$ trajectory is considerably greater than that in the FLCorA trajectory. The trajectory projected to the two-dimensional space described by PC1 and PC2 is shown in Figure 3.22(C)

จุฬาลงกรณ์มหาวิทยาลัย
Chulalongkorn University

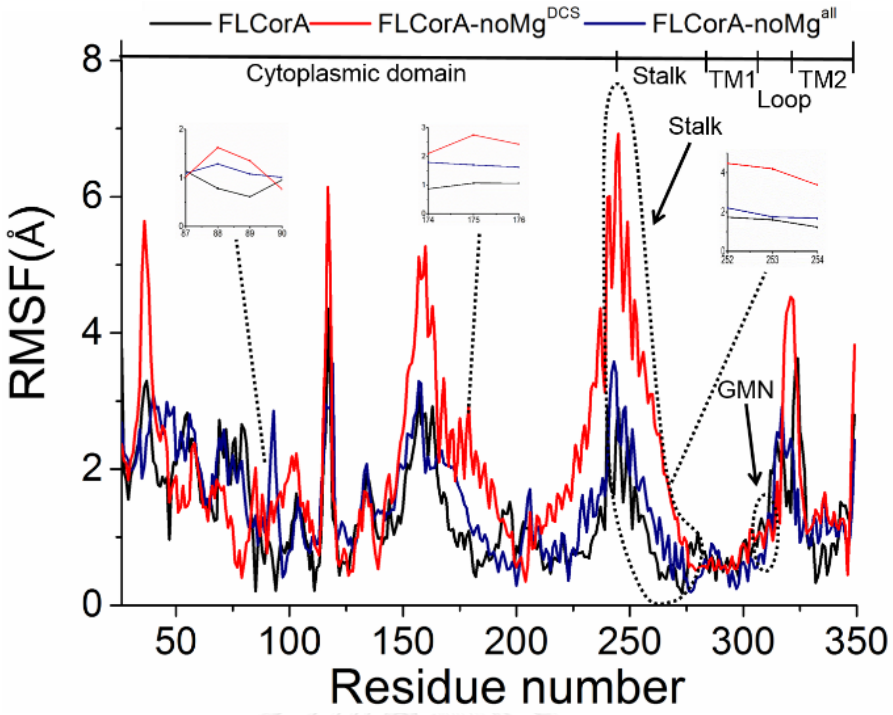


**Figure 3.21** Per-residue Cα RMSFs from the FLCorA (black), FLCorA_noMg$^{DCS}$(red) and FLCorA_noMg$^{all}$ (blue) trajectories analyzed between 60 and 100 ns. The insets highlight an increase of RMSF for the metal-binding residues (E88, D89, D175 and D253) in the DCS site.

จุฬาลงกรณ์มหาวิทยาลัย
Chulalongkorn University

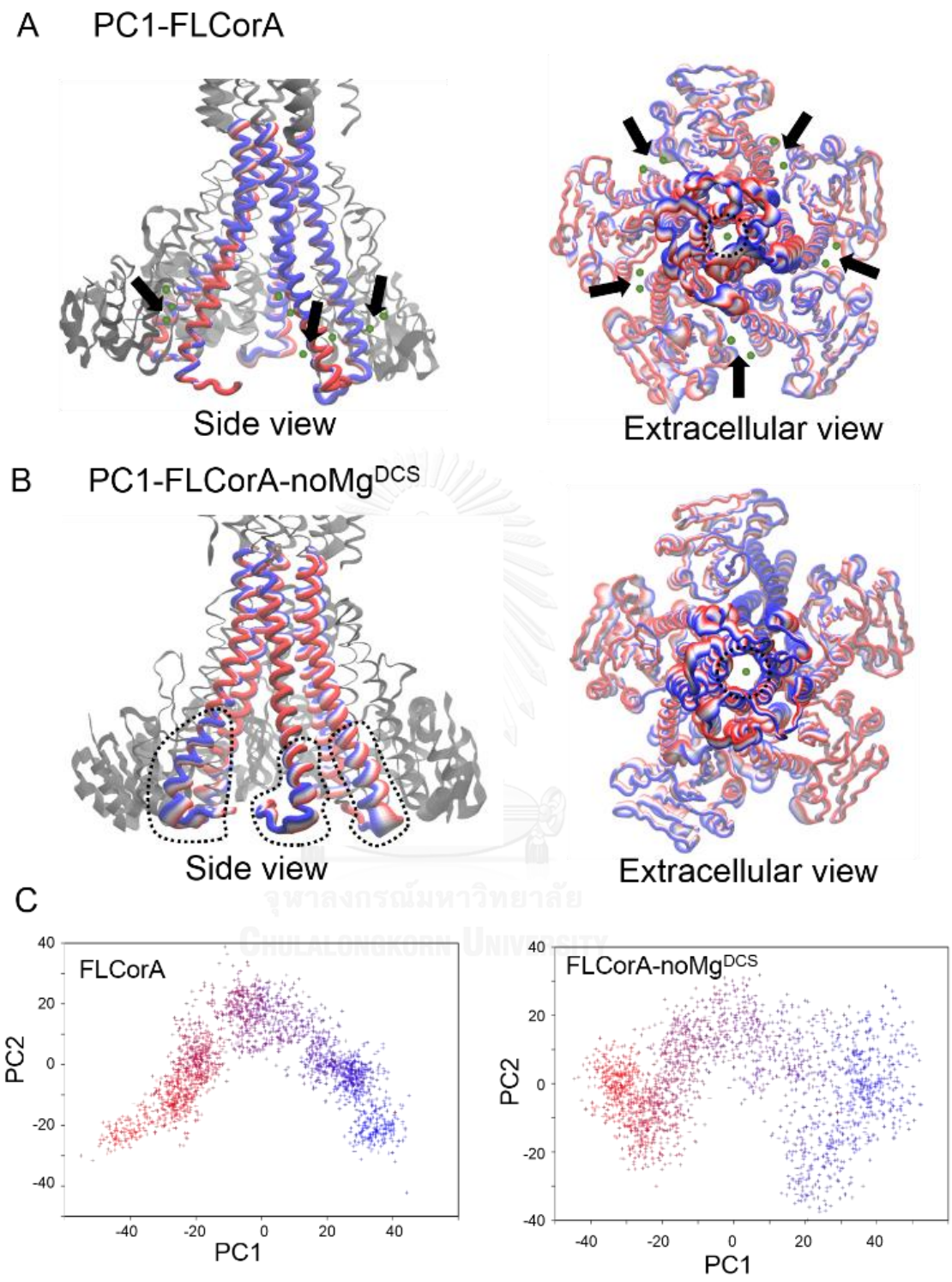


**Figure 3.22** PCA analysis of (A) FLCorA and (B) FLCorA_noMg$^{DCS}$ (extracted from 60-100 ns) along the PC1. Color scale from blue-white-red depicts low to high atomic motion (C) PCA scatter plot where blue-scatter is for the trajectory at 60 ns and red-scatter for the end at 100 ns.

### 3.5.5 QM/MM results: the optimized structure of the hydrated metal in GMN complex

The studied complex model comprises of 4 main parts including metal ion, inner solvation shell (waters or ammines), second-shell waters, and GMN residues (TmCoA-SF). According to the metal-O bond length as reported in the literature [1], the optimized structures of hydrated monovalent cations, $Li^+$, $Na^+$, and $K^+$, in the complex model gave the different geometries from the divalent and trivalent cations, $Mg^{2+}$, $Ca^{2+}$, $Co^{2+}$, $Ni^{2+}$, $Co^{3+}$, and $Al^{3+}$. All monovalent cations did not form the octahedral geometry with the first shell waters while the others form the first shell octahedral structure except $Ca^{2+}$. The optimized structure of $[Mg(H_2O)_6(H_2O)_4SF]^{2+}$ exhibits the inner octahedral structure with an average Mg-O distance of 2.10 Å and the bond angle in the range of 85-95° that is correspond to other experimental and theoretical studies [103]. For the outer shell coordination, the bond length between $Mg^{2+}$ and O-atom of G312 and N314 are in a range of 3.36 – 4.85 Å. The bond lengths between each metal ion and its ligands are listed in Table 3.4 and Figure 3.23 shows the M-O($H_2O$) distance distribution.

**Table 3.4** The structural data obtained from the optimized $[M(H_2O)_x(H_2O)_ySF]^{n+}$ structure.

| ion | CN1 | M-$O_{mean}$ ($H_2O^{1st}$) | M-$O_{mean}$ ($H_2O^{2nd}$) | M-O ($H_2O^{2nd}$) range | M-$O_{mean}$ (G312) | M-O (G312) range | M-$O_{mean}$ (N314) | M-O (N314) range |
|---|---|---|---|---|---|---|---|---|
| $Li^+$ | 5 | 2.09 | 3.81 | 3.11-4.66 | 4.22 | 3.69-4.53 | 4.86 | 4.01-5.92 |
| $Na^+$ | 4 | 2.33 | 4.09 | 3.32-5.71 | 4.53 | 3.04-5.49 | 4.44 | 2.99-6.60 |
| $K^+$ | 5 | 2.85 | 3.87 | 3.02-4.98 | 5.12 | 4.22-5.83 | 4.49 | 3.42-5.32 |
| $Ca^{2+}$ | 7[a] | 2.45 | 4.47 | 3.96-5.00 | 4.42 | 4.04-4.72 | 4.54 | 3.87-5.79 |
| $Mg^{2+}$ | 6 | 2.09 | 4.19 | 3.75-4.70 | 4.26 | 3.77-4.50 | 4.10 | 3.36-4.85 |
| $Co^{2+}$ | 6 | 2.07 | 3.55 | 3.33-3.67 | 4.60 | 4.01-5.60 | 5.47 | 4.42-5.88 |
| $Ni^{2+}$ | 6 | 2.06 | 4.07 | 3.52-4.52 | 4.34 | 4.07-4.64 | 4.42 | 4.11-4.81 |
| $Al^{3+}$ | 6 | 1.92 | 4.13 | 3.67-4.57 | 4.42 | 3.47-5.86 | 3.70 | 3.19-4.18 |
| $Co^{3+}$-hex | 6 | 1.98 | 4.00 | 3.85-4.350 | 5.22 | 4.37-6.07 | 4.28 | 3.66-4.62 |
| $Ni^{2+}$-hex | 6 | 2.13 | 4.24 | 4.17-4.36 | 4.81 | 3.97-6.26 | 4.63 | 4.20-5.11 |

[a]6(O) from $H_2O^{1st}$ + 1(O) from N314

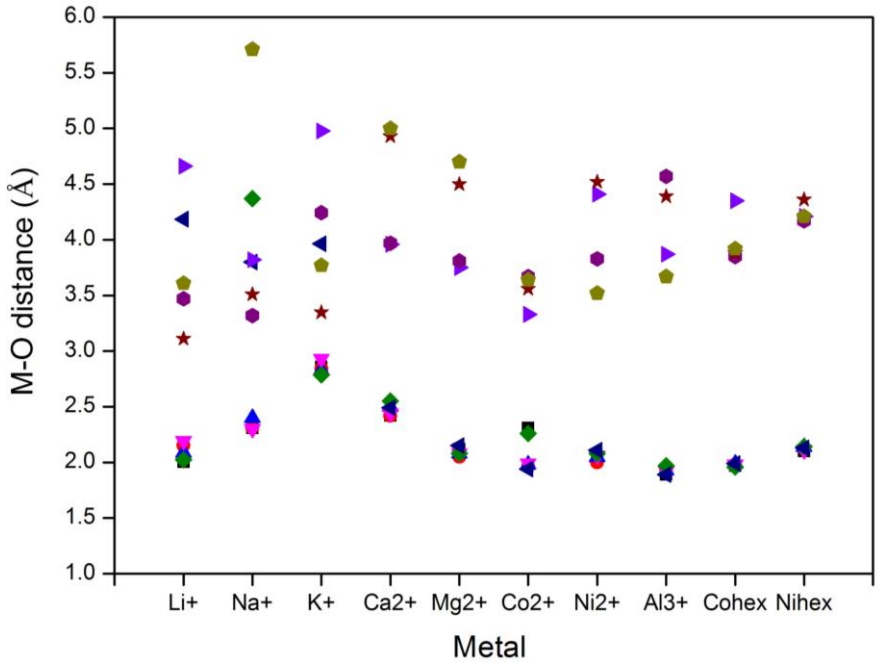


**Figure 3.23** M-O($H_2O$) distance distribution in the $[ML_xW_ySF]^{n+}$ complex

From ten studied ions, there are two ions that have the unpaired electron including $Co^{2+}$ and $Ni^{2+}$ where $Co^{2+}$ has the d-orbital electron configuration as $d^7$ and for $Ni^{2+}$ as $d^8$. The low spin state of them is compatible for studying with the 3-layered ONIOM optimization in this study. To validate the obtaining optimized structures, the spin contamination is considered because a high spin contamination can affect the geometry and population analysis which significantly affect the spin density of the system. The total spin operator (denoted as $<S^2>$) of the unpaired electron containing complex can be calculated from equation (3.6).

$$<S^2> = S(S+1) \qquad (3.6)$$

where "S" is the spin quantum number. The spin quantum number, multiplicity and $<S^2>$ values are listed in Table 3.5 [104]. The spin contamination can be negligible if the computing $<S^2>$ differs from the theoretical value less than 10% [105]. The obtaining $<S^2>$ and the small different percentages shown in Table 3.6 suggest the reliable optimized structures of these complexes.

**Table 3.5** Spin quantum number, multiplicity and $<S^2>$ values.

| spin quantum number<br>S | multiplicity<br>2S+1 | total spin<br>$<S^2>$ |
|---|---|---|
| 0 | 1 (singlet) | 0 |
| 1/2 | 2 (doublet) | 0.75 |
| 1 | 3 (triplet) | 2 |
| 3/2 | 4 (quartet) | 3.75 |
| 2 | 5 (quintet) | 6 |

**Table 3.6** The obtaining $<S^2>$ and the different percentages of the unpaired electron containing complex.

| complex | obtaining $<S^2>$ | % difference |
|---|---|---|
| $[Co(H_2O)_6(H_2O)_4SF]^{2+}$ | 0.759025 | 1.20 |
| $[Ni(H_2O)^6(H_2O)_4SF]^{2+}$ | 2.002934 | 0.15 |
| $[Ni(NH_3)_6(H_2O)_4SF]^{2+}$ | 2.001387 | 0.07 |

For the hydrated divalent cations in the TmCorA-SF, all have the octahedral geometry except for $Ca^{2+}$ that has the coordination number of 7 including 6(O-atoms) from waters and 1(O-atom) from N314 with the average Ca-O distance of 2.45 Å These results indicate that monovalent cations have the different first shell geometries from di- and tri-valent cations. The di- and trivalent cations form hexahydrated geometries (except $Ca^{2+}$) in the TmCorA-SF. In addition, the distance between metal and O-atom of N314 and G312 is rather far to make a direct M-O bond, suggesting these residues acting as the second shell ligand. The O…O distance between the inner shell water and the N314 and G312 is in the range of 2.50 – 2.70 Å which is consistent with the experimental study that reported the distance between O…O to form hydrogen bonding is 2.76 Å [106].

### 3.5.6 QM/MM results: solvation energy of ion (in the TmCorA-SF) and metal binding selectivity

The comparative energy plot among $\Delta E([ML_x]^{n+})$, $\Delta E([ML_xW_y]^{n+})$, hydration energy from [107] and $\Delta E_{sSF}$ is shown in Figure 3.24. The large $\Delta E([ML_x]^{n+})$ values were observed for all ions indicating that the inner-shell complexation is very strong whereas the presence of the second-shell water molecules affects a little higher of the total complexation energy. In case of $\Delta E([ML_xW_y]^{n+})$ values, compared to the reported hydration energy in aqueous solution [107], di- and tri-valent cations provide the lower $\Delta E([ML_xW_y]^{n+})$ energies (less negative energies) whereas monovalent cations give the higher $\Delta E([ML_xW_y]^{n+})$ (more negative energies) suggesting that the monovalent-water-GMN interaction through the stabilization energy ($\Delta E_{sSF}$) is significantly lower than that of the di- and trivalent cations as noticed a trend followed from Cohex > $Al^{3+}$ > Nihex ≈ $Co^{2+}$ ≈ $Ni^{2+}$ ≈ $Mg^{2+}$ ≈ $Ca^{2+}$ > $K^+$ > $Li^+$ > $Na^+$. This order is consistent with the selective binding trend (Cohex > $Mg^{2+}$ ≈ $Co^{2+}$ ≈ Nihex ≈ $Ni^{2+}$ > $Ca^{2+}$) from the experimental $IC_{50}$ (the concentration that inhibits 50% of $Mg^{2+}$-uptake on CorA proteins) reported in the previous researches as shown in Table 3.7.

Amino acid residues can play an important role as been the second-shell ligand of metals in several metalloproteins [108-115]. The full-length simulations as well as truncated models confirm some observed water molecules in the second shell remain to support the metal binding of G312 and N314. In addition, non-octahedral geometries of hydrated monovalent cations were observed. These results indicate that the TmCorA-SF prefers to coordinate with the octahedral complex ion.

จุฬาลงกรณ์มหาวิทยาลัย
Chulalongkorn University

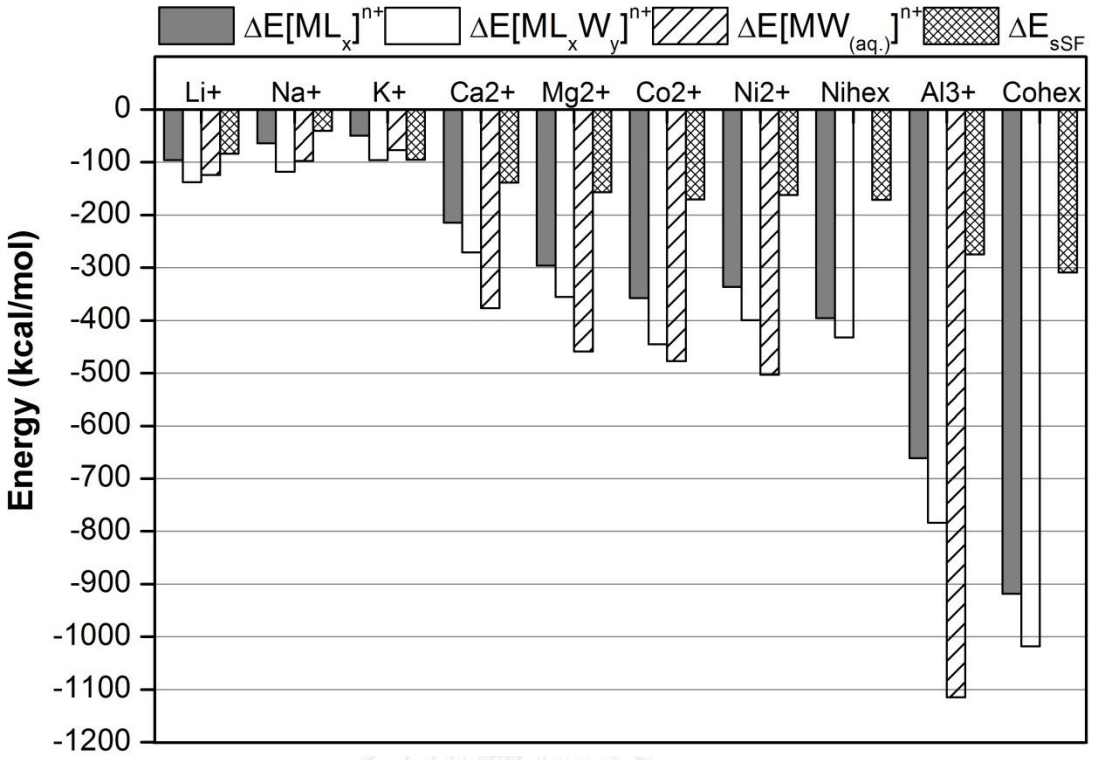


**Figure 3.24** Comparative energy plot among $\Delta E([ML_x]^{n+})$, $\Delta E([ML_xW_y]^{n+})$, the hydration energy denoted as $\Delta E([MW_{(aq.)}]^{n+})$ from [107], and $\Delta E_{sSF}$.

**Table 3.7** Experimental $IC_{50}$ on the CorA activity.

| cation | $IC_{50}$ (μM) | ref |
|---|---|---|
| $Mg^{2+}$ | 10 - 15 | [116] |
| $Co^{2+}$ | 20 – 30 | [116] |
| $Ni^{2+}$ | 200 | [116] |
| $Ca^{2+}$ | 5000 | [66] |
| $Co^{3+}$-hexaammine | 1 | [78] |
| $Ni^{2+}$-hexaammine | > 30 | [78] |

Although the results from MD simulations revealed the initial binding site for both $Co^{3+}$-hex and hydrated-$Mg^{2+}$ at E316 and E320 [117] which was corresponded to the electrostatic position at E316 of Dalmas et al.'s results [73], the positions of $Mg^{2+}$ or $Ca^{2+}$ in the X-ray structure (PDB code of 4EED and 2HN2,

respectively) [67, 70] are almost the center of the GMN motif as the same $Mg^{2+}$ position revealing from the X-ray structure of MjCorA (PDB code 4EV6) [77]. Therefore the GMN motif should be the bona find selectivity filter of CorA protein which is agreed well with mutational studies [62, 74, 118].

## 3.6 Conclusion: TmCorA study

The selectivity role of GMN residues in TmCorA periplasmic loop was investigated by means of MD simulations and QM/MM computations. MD results of $Mg^{2+}$ in the truncated TmCorA-loop suggest the similar appearance of an inner coordination sphere between in TmCorA-loop and in bulk solution while an outer coordination sphere is different. Some second-shell waters were replaced by backbone oxygen of G312 and side chain amide oxygen of N314 indicating that G312 and N314 in the GMN motif are not directly interact with the dehydrated $Mg^{2+}$ but indirectly bind to $Mg^{2+}$ via hydrogen bonding with the inner-shell water molecules as called ion-water-protein interaction. Subsequently, the vacant DCS-$Mg^{2+}$ in the cytoplasmic domain of TmCorA affects the collective motion the most on stalk helix and cytoplasmic domains as well as the GMN scaffold. Moreover, QM/MM study indicates the stabilization energy trend as Cohex > $Al^{3+}$ > Nihex ≈ $Co^{2+}$ ≈ $Ni^{2+}$ ≈ $Mg^{2+}$ ≈ $Ca^{2+}$ > $K^{+}$ > $Li^{+}$ > $Na^{+}$ which is consistent with the selective binding trend observed from the experimental data. Furthermore, the results reveal that the selective property of GMN motif is relied on the geometry recognition of the hydrated ion.

# CHAPTER IV: CONCLUSION

This research has been focused on the investigation of the structure and dynamics properties of two ion channels including potassium and magnesium channels. The MD results of the isolated voltage-sensor domain of KvAP channel showed that both Down-conformations in POPC and DOTAP membranes revealed the accessible water molecules at the intracellular side more than that occurred in the Up-state system as a result of the wider water crevice in the intracellular side present in the Down-state systems for being water-mediated accommodation of the gating charge movement in the VSD-core. For magnesium channel, the simulations results showed that the Gly-Met-Asn (GMN) residues can act as the second shell ligands for stabilizing the hydrated $Mg^{2+}$. Moreover, the absence of $Mg^{2+}$ from the DCS site affected the structural changes at the stalk-helix domain and the GMN cavity resulting in the weaker binding of $Mg^{2+}$ with moving toward the conducting pore. In addition, the results from the QM/MM study showed the stabilization energy trend of ion in the selectivity filter of TmCorA followed from Cohex > $Al^{3+}$ > Nihex ≈ $Co^{2+}$ ≈ $Ni^{2+}$ ≈ $Mg^{2+}$ ≈ $Ca^{2+}$ > $K^{+}$ > $Li^{+}$ > $Na^{+}$ which is consistent with the experimental hydration energy and the experimental selective trend of metal ions in CorA proteins indicating that the selectivity filter of TmCorA channel prefers to bind with the octahedral metal complex.

จุฬาลงกรณ์มหาวิทยาลัย
Chulalongkorn University

## REFERENCES


[1] Persson, I. Hydrated metal ions in aqueous solution: How regular are their structures? Pure Appl. Chem 82 (2010): 1901–1917.

[2] Cooper, G.M. Cell Membranes [Online]. 2000. Available from: http://www.ncbi.nlm.nih.gov/books/NBK9928/ [1 February, 2015]

[3] Reuss, L. Ion Transport across Nonexcitable Membranes. in eLS: John Wiley & Sons, Ltd, 2001.

[4] Demarche, S., Sugihara, K., Zambelli, T., Tiefenauer, L., and Voros, J. Techniques for recording reconstituted ion channels. R Soc Chem 136 (2011): 1077–1089.

[5] Dworakowska, B. and Dolowy, K. Ion channels-related diseases. Acta Biochim Pol 47 (2000): 685-703.

[6] Zlotkin, E. The insect voltage-gated sodium channel as target of insecticides. Annu Rev Entomol 44 (1999): 429-455.

[7] Swaminathan, R. Magnesium Metabolism and its Disorders. The Clinical Biochemist Reviews 24 (2003): 47-66.

[8] Bagal, S.K., et al. Ion channels as therapeutic targets: a drug discovery perspective. J Med Chem 56 (2013): 593-624.

[9] Yu, F.H., Yarov-Yarovoy, V., Gutman, G.A., and Catterall, W.A. Overview of molecular relationships in the voltage-gated ion channel superfamily. Pharmacol Rev 57 (2005): 387-395.

[10] Salkoff, L., Wei, A.D., Baban, B., Butler, A., Fawcett, G., Ferreira, G. and Santi, C.M. Potassium channels in C. elegans. WormBook: The Online Review of C. elegans Biology (2005): 1-15.

[11] Anderson, P.A. and Greenberg, R.M. Phylogeny of ion channels: clues to structure and function. Comp Biochem Physiol B Biochem Mol Biol 129 (2001): 17-28.

[12] Tombola, F., Pathak, M.M., and Isacoff, E.Y. How does voltage open an ion channel? Annu Rev Cell Dev Biol 22 (2006): 23-52.

[13] Swartz, K.J. Sensing voltage across lipid membranes. Nature 456 (2008): 891-897.

[14] Nave, R. Active Transport Across Cell Membranes [Online]. 2001. Available from: http://hyperphysics.phy-astr.gsu.edu/hbase/biology/actran.html [10 March, 2015]

[15] Bean, B.P. The action potential in mammalian central neurons. Nat Rev Neurosci 8 (2007): 451-465.

[16] Jiang, Y., et al. X-ray structure of a voltage-dependent K+ channel. Nature 423 (2003): 33-41.

[17] Murata, Y., Iwasaki, H., Sasaki, M., Inaba, K., and Okamura, Y. Phosphoinositide phosphatase activity coupled to an intrinsic voltage sensor. Nature 435 (2005): 1239-1243.

[18] Kohout, S.C., Ulbrich, M.H., Bell, S.C., and Isacoff, E.Y. Subunit organization and functional transitions in Ci-VSP. Nat Struct Mol Biol 15 (2008): 106-108.

[19] Sasaki, M., Takagi, M., and Okamura, Y. A voltage sensor-domain protein is a voltage-gated proton channel. Science 312 (2006): 589-592.

[20] Ramsey, I.S., Moran, M.M., Chong, J.A., and Clapham, D.E. A voltage-gated proton-selective channel lacking the pore domain. Nature 440 (2006): 1213-1216.

[21] Hodgkin, A.L. and Huxley, A.F. A quantitative description of membrane current and its application to conduction and excitation in nerve. J. Gen. Physiol. 117 (1952): 500-544.

[22] Schoppa, N.E., McCormack, K., Tanouye, M.A., and Sigworth, F.J. The size of gating charge in wild-type and mutant Shaker potassium channels. Science 255 (1992): 1712-1715.

[23] Seoh, S.A., Sigg, D., Papazian, D.M., and Bezanilla, F. Voltage-sensing residues in the S2 and S4 segments of the Shaker K+ channel. Neuron 16 (1996): 1159-1167.

[24] Aggarwal, S.K. and MacKinnon, R. Contribution of the S4 segment to gating charge in the Shaker K+ channel. Neuron 16 (1996): 1169-1177.

[25] Khalili-Araghi, F., Jogini, V., Yarov-Yarovoy, V., Tajkhorshid, E., Roux, B., and Schulten, K. Calculation of the gating charge for the Kv1.2 voltage-activated potassium channel. Biophys J 98 (2010): 2189-2198.

จุฬาลงกรณ์มหาวิทยาลัย
Chulalongkorn University

[26] Chanda, B., Kwame Asamoah, O., Blunck, R., Roux, B., and Bezanilla, F. Gating charge displacement in voltage-gated ion channels involves limited transmembrane movement. Nature 436 (2005): 852-856.

[27] Keynes, R.D.E., F. The screw-helical voltage gating of ion channels. Proc Natl Acad Sci U S A 266 (1999): 843-852.

[28] Broomand, A. and Elinder, F. Large-scale movement within the voltage-sensor paddle of a potassium channel-support for a helical-screw motion. Neuron 59 (2008): 770-777.

[29] Horn, R. How ion channels sense membrane potential. Proc Natl Acad Sci U S A 102 (2005 ): 4929-4930.

[30] Bezanilla, F. Voltage Sensor Movements. J. Gen. Physiol. 120 (2002): 465-473.

[31] Li, Q., Wanderling, S., Sompornpisut, P., and Perozo, E. Structural basis of lipid-driven conformational transitions in the KvAP voltage-sensing domain. Nat Struct Mol Biol 21 (2014): 160-166.

[32] Bezanilla, F. Voltage-Gated Ion Channels. IEEE T Nanobiosci 4 (2005): 34-48.

[33] Jiang, Q.X., Wang, D.N., and MacKinnon, R. Electron microscopic analysis of KvAP voltage-dependent K+ channels in an open conformation. Nature 430 (2004): 806-810.

[34] Cuello, L.G., Cortes, D.M., and Perozo, E. Molecular architecture of the KvAP voltage-dependent K+ channel in a lipid bilayer. Science 306 (2004): 491-495.

[35] Schmidt, D., Jiang, Q.-X., and MacKinnon, R. Phospholipids and the origin of cationic gating charges in voltage sensors. Nature 444 (2006): 775-779.

[36] Xu, Y., Ramu, Y., and Lu, Z. Removal of phospho-head groups of membrane lipids immobilizes voltage sensors of K+ channels. Nature 451 (2008): 826-829.

[37] Zheng, H., Liu, W., Anderson, L.Y., and Jiang, Q.-X. Lipid-dependent gating of a voltage-gated potassium channel. Nat Commun 2 (2011): 1-9.

[38] Krepkiy, D., Gawrisch, K., and Swartz, K.J. Structural interactions between lipids, water and S1-S4 voltage-sensing domains. J Mol Biol 423 (2012): 632-647.

[39] Larsson, H.P., Baker, O.S., Dhillon, D.S., and Isacoff, E.Y. Transmembrane Movement of the Shaker K+ Channel S4. Neuron 16 (1996): 387-397.

[40] Baker, O.S., Larsson, H.P., Mannuzzu, L.M., and Isacoff, E.Y. Three Transmembrane Conformations and Sequence-Dependent Displacement of the S4 Domain in Shaker K+ Channel Gating. Neuron 20 (1998): 1283-1294.

[41] Wang, M.H., Yusaf, S.P., Elliott, D.J., Wray, D., and Sivaprasadarao, A. Effect of cysteine substitutions on the topology of the S4 segment of the Shaker potassium channel: implications for molecular models of gating. J Physiol 521 (1999): 315-326.

[42] Freites, J.A., Tobias, D.J., von Heijne, G., and White, S.H. Interface connections of a transmembrane voltage sensor. Proc Natl Acad Sci U S A 102 (2005): 15059-15064.

[43] Freites, J.A., Tobias, D.J., and White, S.H. A voltage-sensor water pore. Biophys J 91 (2006): L90-L92.

[44] Andersson, M., Freites, J.A., Tobias, D.J., and White, S.H. Structural Dynamics of the S4 Voltage-Sensor Helix in Lipid Bilayers Lacking Phosphate Groups. J Phy Chem B 115 (2011): 8732-8738.

[45] Fuklang, S. Structural and dynamical properties of voltage sensor domain of activated and resting potassium channel in lipid bilayer by molecular dynamics simulation. Master degree, Department of Chemistry, Faculty of Science Chulalongkorn University, 2012.

[46] Sompornpisut, P., Roux, B., and Perozo, E. Structural refinement of membrane proteins by restrained molecular dynamics and solvent accessibility data. Biophys J 95 (2008): 5349-5361.

[47] Hubbell, W.L., McHaourab, H.S., Altenbach, C., and Lietzow, M.A. Watching proteins move using site-directed spin labeling. Structure 4 (1996): 779-783.

[48] Klug, C.S. and Feix, J.B. Methods and applications of site-directed spin labeling EPR spectroscopy. Methods Cell Biol 84 (2008): 617-658.

[49] Brooks, B.R., et al. CHARMM: The Biomolecular Simulation Program. J Comput Chem 30 (2009): 1545-1614.

[50] Phillips, J.C., et al. Scalable molecular dynamics with NAMD. J Comput Chem 26 (2005): 1781-1802.

[51] Humphrey, W., Dalke, A., and Schulten, K. VMD: Visual molecular dynamics. J Mol Graph Model 14 (1996): 33-38.

[52] Seeber, M., et al. Wordom: A User-Friendly Program for the Analysis of Molecular Structures, Trajectories, and Free Energy Surfaces. J Comput Chem 32 (2011): 1183-1194.

[53] Callenberg, K.M., Choudhary, O.P., de Forest, G.L., Gohara, D.W., Baker, N.A., and Grabe, M. APBSmem: a graphical interface for electrostatic calculations at the membrane. PLoS One 5 (2010): 1-11.

[54] Dolinsky, T.J., Nielsen, J.E., McCammon, J.A., and Baker, N.A. PDB2PQR: an automated pipeline for the setup of Poisson-Boltzmann electrostatics calculations. Nucleic Acids Res 32 (2004): W665-W667.

[55] Baker, N.A., Sept, D., Joseph, S., Holst, M.J., and McCammon, J.A. Electrostatics of nanosystems: Application to microtubules and the ribosome. Proc Natl Acad Sci U S A 98 (2001): 10037-10041.

[56] Aksimentiev, A.S., M.; Wells, D. University of Illinois at Urbana-Champaign Beckman Institute for Advanced Science and Technology Theoretical and Computational Biophysics Group Computational Biophysics Workshop. (2012): 1-43.

[57] Fogolari, F., Zuccato, P., Esposito, G., and Viglino, P. Biomolecular Electrostatics with the Linearized Poisson-Boltzmann Equation. Biophys J 76 (1999): 1-16.

[58] Grabe, M.L., H.; Jan, Y. N.; Jan, L. Y. . A Quantitative Assessment of Models for Voltage-Dependent Gating of Ion Channels. Proc. Natl. Acad. Sci. U.S.A. 101 (2004): 17640−17645.

[59] Jiang, Y., Ruta, V., Chen, J., Lee, A., and MacKinnon, R. The principle of gating charge movement in a voltage-dependent K+ channel. Nature 423 (2003): 42-48.

[60] Markham, G.D., Glusker, J.P., and Bock, C.W. The Arrangement of First- and Second-Sphere Water Molecules in Divalent Magnesium Complexes: Results from Molecular Orbital and Density Functional Theory and from Structural Crystallography. J Phys Chem B 106 (2002): 5118-5134.

[61] Vinogradov, E.V., Smirnov, P.R., and Trostin, V.N. Structure of hydrated complexes formed by metal ions of Groups I—III of the Periodic Table in

aqueous electrolyte solutions under ambient conditions. Russ Chem B+ 52 (2003): 1253-1271.

[62] Moomaw, A.S. and Maguire, M.E. Cation selectivity by the CorA Mg2+ channel requires a fully hydrated cation. Biochemistry 49 (2010): 5998-6008.

[63] Niegowski, D. and Eshaghi, S. The CorA family: structure and function revisited. Cell Mol Life Sci 64 (2007): 2564-2574.

[64] Gardner, R.C. Genes for magnesium transport. Current Opinion in Plant Biology 6 (2003): 263-267.

[65] Smith, R.L., Banks, J.L., Snavely, M.D., and Maguire, M.E. Sequence and topology of the CorA magnesium transport systems of Salmonella typhimurium and Escherichia coli. Identification of a new class of transport protein. J Biol Chem 268 (1993): 14071-14080.

[66] Snavely, M.D., Florer, J.B., Miller, C.G., and Maguire, M.E. Magnesium transport in Salmonella typhimurium: 28Mg2+ transport by the CorA, MgtA, and MgtB systems. J Bacteriol 171 (1989): 4761-4766.

[67] Payandeh, J. and Pai, E.F. A structural basis for Mg2+ homeostasis and the CorA translocation cycle. Embo j 25 (2006): 3762-3773.

[68] Eshaghi, S., Niegowski, D., Kohl, A., Martinez Molina, D., Lesley, S.A., and Nordlund, P. Crystal structure of a divalent metal ion transporter CorA at 2.9 angstrom resolution. Science 313 (2006): 354-357.

[69] Lunin, V.V., et al. Crystal structure of the CorA Mg2+ transporter. Nature 440 (2006): 833-837.

[70] Pfoh, R., Li, A., Chakrabarti, N., Payandeh, J., Pomes, R., and Pai, E.F. Structural asymmetry in the magnesium channel CorA points to sequential allosteric regulation. Proc Natl Acad Sci U S A 109 (2012): 18809-18814.

[71] Chakrabarti, N., Neale, C., Payandeh, J., Pai, E.F., and Pomes, R. An iris-like mechanism of pore dilation in the CorA magnesium transport system. Biophys J 98 (2010): 784-792.

[72] Wapeesittipan, P. Molecular dynamics simulation of closed and open state models of magnesium transporter in lipid bilayer. A thesis submitted in partial fulfillment of the requirements for the degree of Master of science program in chemistry, Chulalogkorn Unversity, 2012.

[73] Dalmas, O., Cuello, L.G., Jogini, V., Cortes, D.M., Roux, B., and Perozo, E. Structural Dynamics Of The Magnesium-Bound Conformation Of Cora In A Lipid Bilayer. Structure 18 (2010): 868-878.

[74] Dalmas, O., Sandtner, W., Medovoy, D., Frezza, L., Bezanilla, F., and Perozo, E. A Repulsion Mechanism Explains Magnesium Permeation And Selectivity In Cora. Proc Natl Acad Sci U S A (2014): 3002–3007.

[75] Dalmas, O., Sompornpisut, P., Bezanilla, F., and Perozo, E. Molecular Mechanism of Mg(2+)-dependent gating in CorA. Nature communications 5 (2014): 3590-3590.

[76] Nordin, N., et al. Exploring the structure and function of Thermotoga maritima CorA reveals the mechanism of gating and ion selectivity in Co2+/Mg2+ transport. Biochem J 451 (2013): 365-374.

[77] Guskov, A., et al. Structural insights into the mechanisms of Mg2+ uptake, transport, and gating by CorA. Proc Natl Acad Sci U S A 109 (2012): 18459-64.

[78] Kucharski, L.M., Lubbe, W.J., and Maguire, M.E. Cation hexaammines are selective and potent inhibitors of the CorA magnesium transport system. J Biol Chem 275 (2000): 16767-16773.

[79] Palombo, I., Daley, D.O., and Rapp, M. Why Is the GMN Motif Conserved in the CorA/Mrs2/Alr1 Superfamily of Magnesium Transport Proteins? Biochemistry 52 (2013): 4842-4847.

[80] Frisch, M.J.T., G. W.; Schlegel, H. B.; Scuseria, G. E.; Robb, M. A.; Cheeseman, J. R.; Scalmani, G.; Barone, V.; Mennucci, B.; Petersson, G. A.; Nakatsuji, H.; Caricato, M.; Li, X.; Hratchian, H. P.; Izmaylov, A. F.; Bloino, J.; Zheng, G.; Sonnenberg, J. L.; Hada, M.; Ehara, M.; Toyota, K.; Fukuda, R.; Hasegawa, J.; Ishida, M.; Nakajima, T.; Honda, Y.; Kitao, O.; Nakai, H.; Vreven, T.; Montgomery, Jr., J. A.; Peralta, J. E.; Ogliaro, F.; Bearpark, M.; Heyd, J. J.; Brothers, E.; Kudin, K. N.; Staroverov, V. N.; Kobayashi, R.; Normand, J.; Raghavachari, K.; Rendell, A.; Burant, J. C.; Iyengar, S. S.; Tomasi, J.; Cossi, M.; Rega, N.; Millam, J. M.; Klene, M.; Knox, J. E.; Cross, J. B.; Bakken, V.; Adamo, C.; Jaramillo, J.; Gomperts, R.; Stratmann, R. E.; Yazyev, O.; Austin, A. J.; Cammi, R.; Pomelli, C.; Ochterski, J. W.; Martin, R.

L.; Morokuma, K.; Zakrzewski, V. G.; Voth, G. A.; Salvador, P.; Dannenberg, J. J.; Dapprich, S.; Daniels, A. D.; Farkas, Ö.; Foresman, J. B.; Ortiz, J. V.; Cioslowski, J.; Fox, D. J. Gaussian 09 Gaussian, Inc. (2009): Wallingford CT.

[81] Dennington, R.K., Todd; Millam, John. GaussView 05 Semichem Inc (2009): Shawnee Mission, KS.

[82] Xiang, Z., Soto, C.S., and Honig, B. Evaluating conformational free energies: the colony energy and its application to the problem of loop prediction. Proc Natl Acad Sci U S A 99 (2002): 7432-7437.

[83] Perozo, E., Cortes, D.M., Sompornpisut, P., Kloda, A., and Martinac, B. Open channel structure of MscL and the gating mechanism of mechanosensitive channels. Nature 418 (2002): 942-948.

[84] Aksimentiev, A., Sotomayor, M., and Wells, D. Membrane Proteins Tutorial. University of Illinois at Urbana-Champaign Beckman Institute for Advanced Science and Technology Theoretical and Computational Biophysics Group Computational Biophysics Workshop (2012): 1-43.

[85] Jorgensen, W.L., Chandrasekhar, J., Madura, J.D., Impey, R.W., and Klein, M.L. Comparison of simple potential functions for simulating liquid water. J Chem Phys 79 (1983): 926-935.

[86] Darden, T., York, D., and Pedersen, L. Particle Mesh Ewald - an N.Log(N) Method for Ewald Sums in Large Systems. Journal of Chemical Physics 98 (1993): 10089-10092.

[87] Ryckaert, J.-P., Ciccotti, G., and Berendsen, H.J.C. Numerical integration of the Cartesian equations of motion of a system with constraints: molecular dynamics of n-alkanes. J Comput Phys 23 (1977): 327-341.

[88] Miyamoto, S. and Kollman, P.A. Settle: An analytical version of the SHAKE and RATTLE algorithm for rigid water models. J Comput Chem 13 (1992): 952-962.

[89] Feller, S.E., Zhang, Y.H., Pastor, R.W., and Brooks, B.R. Constant-Pressure Molecular-Dynamics Simulation - the Langevin Piston Method. J Chem Phys 103 (1995): 4613-4621.

[90] Martyna, G.J., Tobias, D.J., and Klein, M.L. Constant-Pressure Molecular-Dynamics Algorithms. J Chem Phys 101 (1994): 4177-4189.

จุฬาลงกรณ์มหาวิทยาลัย
Chulalongkorn University

[91] Smart, O.S., Neduvelil, J.G., Wang, X., Wallace, B.A., and Sansom, M.S. HOLE: a program for the analysis of the pore dimensions of ion channel structural models. J Mol Graph 14 (1996): 354-360.

[92] Luzar, A. Resolving the hydrogen bond dynamics conundrum. J Chem Phys 113 (2000): 10663-10675.

[93] Rocchi, C.B., Anna Rita; Cannistraro, Salvatore. Water dynamical anomalies evidenced by molecular-dynamics simulations at the solvent-protein interface. Phys. Rev. E 57 (1998): 3315-3325.

[94] Morokuma, K. New challenges in quantum chemistry: quests for accurate calculations for large molecular systems. Philos T Roy Soc A 360 (2002): 1149-1164.

[95] Kim, K. and Jordan, K.D. Comparison of Density Functional and MP2 Calculations on the Water Monomer and Dimer. J. Phy. Chem. 98 (1994): 10089-10094.

[96] Stewart, J.J.P. Optimization of parameters for semiempirical methods V: Modification of NDDO approximations and application to 70 elements. J. Mol Model 13 (2007): 1173-1213.

[97] Rappe, A.K., Casewit, C.J., Colwell, K.S., Goddard, W.A., and Skiff, W.M. UFF, a full periodic table force field for molecular mechanics and molecular dynamics simulations. J. Am. Chem. Soc. 114 (1992): 10024-10035.

[98] Helm, L. and Merbach, A.E. Inorganic and bioinorganic solvent exchange mechanisms. Chem Rev 105 (2005): 1923-1959.

[99] Caminiti, R., Licheri, G., Piccaluga, G., and Pinna, G. X-ray diffraction study of magnesium chloride aqueous solutions. J Appl Crystallogr 12 (1979): 34-38.

[100] Tongraar, A. and Rode, B.M. The role of non-additive contributions on the hydration shell structure of Mg2+ studied by Born-Oppenheimer ab initio quantum mechanical/molecular mechanical molecular dynamics simulation. Chem Phys Lett 346 (2001): 485-491.

[101] Tongraar, A. and Rode, B.M. Structural arrangement and dynamics of the hydrated Mg2+: An ab initio QM/MM molecular dynamics simulation. Chem Phys Lett 409 (2005): 304-309.

[102] Markham, G.D., Glusker, J.P., and Bock, C.W. The arrangement of first- and second-sphere water molecules in divalent magnesium complexes: Results from molecular orbital and density functional theory and from structural crystallography. J Phys Chem B 106 (2002): 5118-5134.

[103] Bock, C.W., Markham, G.D., Katz, A.K., and Glusker, J.P. The Arrangement of First- and Second-shell Water Molecules Around Metal Ions: Effects of Charge and Size. Theor Chem Acc 115 (2006): 100-112.

[104] molecular_modeling_notes_13 [Online]. Available from: http://www.uwyo.edu/kubelka-chem/molecular_modeling_notes_13.pdf [6 May, 2016]

[105] David, Y. Spin Contamination [Online]. Available from: http://www.ccl.net/cca/documents/dyoung/topics-framed/spin_cont.shtml [5 May 2016]

[106] Pavlov, M., Siegbahn, P.E.M., and Sandstro, M. Hydration of Beryllium, Magnesium, Calcium, and Zinc Ions Using Density Functional Theory. J. Phys. Chem. A 102 (1998): 219-228.

[107] Smith, D.W. Ionic Hydration Enthalpies. J. Chem. Educ. 54 (1977): 540-542.

[108] Maynard, A.T. and Covell, D.G. Reactivity of zinc finger cores: analysis of protein packing and electrostatic screening. J Am Chem Soc 123 (2001): 1047-1058.

[109] Dudev, T. and Lim, C. Factors governing the protonation state of cysteines in proteins: an Ab initio/CDM study. J Am Chem Soc 124 (2002): 6759-6766.

[110] Lesburg, C.A., Lloyd, M.D., Cane, D.E., and Christianson, D.W. Crystallization and preliminary X-ray diffraction analysis of recombinant pentalenene synthase. Protein Sci 4 (1995): 2436-2438.

[111] Mertz, P., Yu, L., Sikkink, R., and Rusnak, F. Kinetic and spectroscopic analyses of mutants of a conserved histidine in the metallophosphatases calcineurin and lambda protein phosphatase. J Biol Chem 272 (1997): 21296-21302.

[112] He, Q.Y., et al. Mutations at nonliganding residues Tyr-85 and Glu-83 in the N-lobe of human serum transferrin. Functional second shell effects. J Biol Chem 273 (1998): 17018-17024.

จุฬาลงกรณ์มหาวิทยาลัย
Chulalongkorn University

[113] Vipond, I.B., Moon, B.J., and Halford, S.E. An isoleucine to leucine mutation that switches the cofactor requirement of the EcoRV restriction endonuclease from magnesium to manganese. Biochemistry 35 (1996): 1712-1721.

[114] Marino, S.F. and Regan, L. Secondary ligands enhance affinity at a designed metal-binding site. Chem Biol 6 (1999): 649-655.

[115] Dudev, T., Lin, Y.L., Dudev, M., and Lim, C. First-second shell interactions in metal binding sites in proteins: A PDB survey and DFT/CDM calculations. J Am Chem Soc 125 (2003): 3168-3180.

[116] Maguire, M.E. Magnesium transporters: properties, regulation and structure. Front Biosci 11 (2006): 3149-3163.

[117] Zhang, T. and Mu, Y. Initial binding of ions to the interhelical loops of divalent ion transporter CorA: replica exchange molecular dynamics simulation study. PLoS One 7 (2012): 1-11.

[118] Payandeh, J., Li, C., Ramjeesingh, M., Poduch, E., Bear, C.E., and Pai, E.F. Probing structure-function relationships and gating mechanisms in the CorA Mg2+ transport system. J Biol Chem 283 (2008): 11721-11733.

จุฬาลงกรณ์มหาวิทยาลัย
Chulalongkorn University

# APPENDIX



จุฬาลงกรณ์มหาวิทยาลัย
Chulalongkorn University

# VITA

I was born on February 18, 1978 in Chonburi, Thailand. I graduated with Bachelor's and Master's degrees of Science in Chemistry both from Faculty of Science, Kasetsart University, in 2000 and in 2003, respectively. After that I have been a lecturer in Chemistry at Faculty of Science at Sriracha, Kasetsart University Sriracha Campus since 2003 then I have received the opportunity for full-time studying in the Ph.D. program (the Nanoscience and Technology Program Graduate School) at Chulalongkorn University since 2013, during this time, I have got 2 publications which are:

1. Kitjaruwankul S., Boonamnaj P., Fuklang S., Supunyabut C. Sompornpisut P. 2015. Shaping the Water Crevice to Accommodate the Voltage Sensor in a Down Conformation: A Molecular Dynamics Simulation Study. J. Phys.Chem. B., 119, 6516 – 6524.

2. Kitjaruwankul S., Wapeesittipan P., Boonamnaj P., Sompornpisut P. 2016. Inner and Outer Coordination Shells of Mg2+ in CorA Selectivity Filter from Molecular Dynamics Simulations., J. Phys.Chem. B., 120, 406–417.

My present address is 78/9, Moo 12, Napa Town, Muang District, Sukprayoon Road, Chonburi, Thailand, 20000 and my e-mail addresses are sunankit@gmail.com and srcsnk@ku.ac.th.

จุฬาลงกรณ์มหาวิทยาลัย
Chulalongkorn University